Fatigue, Fracture and Impact of Hybrid Carbon Fiber Reinforced Polymer Composites

Ayoub Yari Boroujeni

Dissertation submitted to the faculty of the

Virginia Polytechnic Institute and State University

in partial fulfillment of the requirements for the degree of

Doctor of Philosophy

in

Engineering Mechanics

Marwan S. Al-Haik, Chair

Scott W. Case, Co-Chair

Muhammad R. Hajj

Mayuresh Patil

Michael Philen

November 28, 2016

Blacksburg, Virginia

Keywords: hybrid carbon fiber reinforced polymer composites, carbon nanotubes, ZnO nanorods, mechanical characterization, finite element modeling

Fatigue, Fracture and Impact of Hybrid Carbon Fiber Reinforced Polymer Composites

Ayoub Yari Boroujeni

ABSTRACT

The excellent in-plane strength and stiffness to-weight ratios, as well as the ease of manufacturing have made the carbon fiber reinforced polymer composites (CFRPs) suitable structural materials for variety of applications such as aerospace, automotive, civil, sporting goods, etc. Despite the outstanding performance of the CFRPs along their fibers direction (on-axis), they lack sufficient strength and performance in the out-of-plane and off-axis directions. Various chemical and mechanical methods were reported to enhance the CFRPs' out-of-plane performance. However, there are two major drawbacks for utilizing these approaches: first, most of these methods induce damage to the carbon fibers and, therefore, deteriorate the in-plane mechanical properties of the entire CFRP, and second, the methods with minimal deteriorating effects on the in-plane mechanical performance have their own limitations resulting in very confined mechanical performance improvements. These methods include integrating nano-sized reinforcements into the CFRPs' structure to form a hybrid or hierarchical CFRPs.

In lieu to all the aforementioned approaches, a relatively novel method, referred to as graphitic structures by design (GSD), has been proposed. The GSD is capable of grafting carbon nanotubes (CNTs) onto the carbon fibers surfaces, providing high concentration of CNTs where they are most needed, i.e. the immediate fiber/matrix interface, and in-between the different laminae of a CFRP. This method shows promising improvements in the in-plane and out-of-plane performance of CFRPs. Zinc oxide (ZnO) nanorods are other nano-sized reinforcing

structures which can hybridize the CFRPs via their radially growth on the surface of carbon fibers. Among all the reported methods for synthesizing ZnO nanorods, hydrothermal technique is the most straightforward and least destructive route to grow ZnO nanorods over carbon fibers.

In this dissertation, the GSD-CNTs growth method and the hydrothermal growth of ZnO nanorods have been utilized to fabricate hybrid CFRPs. The effect of different ZnO nanorods growth morphologies, e.g. size distribution and alignment, on the in-plane tensile performance and vibration attenuation capabilities of the hybrid CFRPs are investigated via quasi-static tension and dynamical mechanical analysis (DMA) tests, respectively. As a result, the in-plane tensile strength of the hybrid CFRPs were improved by 18% for the composite based on randomly oriented ZnO nanorods over the carbon fibers. The loss tangent of the CFRPs, which indicates the damping capability, increased by 28% and 19% via radially and randomly grown ZnO nanorods, respectively.

While there are several studies detailing the effects of dispersed nanofillers on the fracture toughness of FRPs, currently, there are no literature detailing the effect of surface GSD grown CNTs and ZnO nanowire -on carbon fiber- on the fracture toughness of these hybrid composites. This dissertation probes the effects of surface grown nano-sized reinforcements on the fracture toughness via double cantilever beam (DCB) tests on hybrid ZnO nanorod or CNT grafted CFRPs. Results show that the surface grown CNTs enhanced the Mode I interlaminar fracture toughness (G_{Ic}) of the CFRPs by 22% and 32%, via uniform and patterned growth morphologies, respectively, over the reference composite based on untreated carbon fiber fabrics.

The dissertation also explains the basis of the improvements of the fracture toughness via finite element method (FEM). In particular, FEM was employed to simulate the interlaminar crack

growth behavior of the hybrid CFRPs under Mode I crack opening loading conditions embodied by the DCB tests. These simulations revealed that the hybrid CFRP based on fibers with uniform surface grown MWCNTs exhibited 55% higher interlaminar strength compared to the reference CFRPs. Moreover, via patterned growth of MWCNTs, the ultimate crack opening resistance of the CFRPs improved by 20%. To mimic the experimental behavior of the various CFRPs, a new methodology has been utilized to accurately simulate the unstable crack growth nature of CFRPs.

Several investigations reported the effects of adding nanomaterials-including CNTs- as a filler phase inside the matrix material, on the impact energy absorption of the hybrid FRPs. However, the impact mitigation performance of CFRPs based on ZnO nanorod grafted carbon fibers has not been reported. The dynamic out-of-plane energy dissipation capabilities of different hybrid composites were investigated utilizing high velocity (~90 m/s) impact tests. Comparing the results of the hybrid MWCNT/ZnO nanorod/CFRP with those of reference CFRP, 21% and 4% improvements were observed in impact energy absorption and tensile strain to failure of the CFRPs, respectively.

In addition to elevated stiffness and strength, CFRPs should possess enough tolerance not only to monotonic loadings, but also to cyclic loadings to be qualified as alternatives to traditional structural metal alloys. Therefore, the fatigue life of CFRPs is of much interest. Despite the promising potential of incorporating nano-sized reinforcements into the CFRPs structure, not many studies reported on the fatigue behavior of hybrid CFRPs so far. In particular, there are no reported investigations to the effect of surface grown CNTs on the fatigue behavior of the hybrid CFRPs, due to fact that almost all the CNT growth techniques (except for the GSD method) deteriorated the in-plane performance of the hybrid CFRPs. The hybrid ZnO nanorod grafted CFRPs have not been investigated under fatigue loading as well. In this dissertation, different

hybrid CFRPs were tested under tension-tension fatigue to reveal the effects of the different nano-reinforcements growth on the fatigue behavior of the CFRPs. A remarkable fatigue damage tolerance was observed for the CFRPs based on uniform and patterned grown CNT fibers. Almost two decades of fatigue life extension was achieved for CFRPs based on surface grown MWCNTs.

Fatigue, Fracture and Impact of Hybrid Carbon Fiber Reinforced Polymer Composites

Ayoub Yari Boroujeni

GENERAL AUDIENCE ABSTRACT

Carbon fiber reinforced polymer composites (CFRPs) are light-weight materials with excellent strength and stiffness along the direction of the fibers. These great mechanical properties have made CFRPs suitable structural materials for variety of applications such as aerospace, automotive, civil, sporting goods, etc. Despite the outstanding performance of the CFRPs along their fibers direction (on-axis), they lack sufficient strength and performance in the out-of-plane and off-axis directions. Various chemical and mechanical methods were reported to enhance the CFRPs' out-of-plane performance. However, there are two major drawbacks for utilizing these approaches: first, most of these methods induce damage to the carbon fibers and, therefore, deteriorate the in-plane mechanical properties of the entire CFRP, and second, the methods with minimal deteriorating effects on the in-plane mechanical performance have their own limitations resulting in very confined mechanical performance improvements. These methods include integrating nano-sized reinforcements into the CFRPs' structure to form a hybrid or hierarchical CFRPs.

In lieu to all the aforementioned approaches, a relatively novel method, referred to as graphitic structures by design (GSD), has been proposed. The GSD is capable of grafting carbon nanotubes (CNTs) onto the carbon fibers surfaces, providing high concentration of CNTs where they are most needed, i.e. the immediate fiber/matrix interface, and in-between the different layers of a CFRP. This method shows promising improvements in the in-plane and out-of-plane

performance of CFRPs. Zinc oxide (ZnO) nanorods are other nano-sized reinforcing structures which can hybridize the CFRPs via their radially growth on the surface of carbon fibers. Among all the reported methods for synthesizing ZnO nanorods, hydrothermal technique is the most straightforward and least destructive route to grow ZnO nanorods over carbon fibers.

In this dissertation, the GSD-CNTs growth method and the hydrothermal growth of ZnO nanorods have been utilized to fabricate hybrid CFRPs. The effect of different ZnO nanorods growth morphologies, e.g. size distribution and alignment, on the in-plane tensile performance and vibration damping capabilities of the hybrid CFRPs are investigated via tension and dynamical mechanical analysis (DMA) tests, respectively. As a result, the in-plane tensile strength of the hybrid CFRPs were improved by 18% for the composite based on randomly oriented ZnO nanorods over the carbon fibers. The loss tangent of the CFRPs, which indicates the damping capability, increased by 28% and 19% via radially and randomly grown ZnO nanorods, respectively.

Fracture toughness is a measure for the capability of a material to withstand a load in the presence of damage (i.e. crack) in the material's structure. While there are several studies detailing the effects of dispersed nanofillers on the fracture toughness of FRPs, currently, there are no literature detailing the effect of surface GSD grown CNTs and ZnO nanowire -on carbon fiber- on the fracture toughness of these hybrid composites. This dissertation probes the effects of surface grown nano-sized reinforcements on the fracture toughness via double cantilever beam (DCB) tests on hybrid ZnO nanorod or CNT grafted CFRPs. Results show that the surface grown CNTs enhanced the Mode I interlaminar fracture toughness (G_{Ic}) of the CFRPs by 22% and 32%, via uniform and patterned growth morphologies, respectively, over the reference composite based on untreated carbon fiber fabrics.

The dissertation also explains the basis of the improvements of the fracture toughness via finite element method (FEM). In particular, FEM was employed to simulate the interlaminar crack growth behavior of the hybrid CFRPs under Mode I crack opening loading conditions embodied by the DCB tests. These simulations revealed that the hybrid CFRP based on fibers with uniform surface grown MWCNTs exhibited 55% higher interlaminar strength compared to the reference CFRPs. Moreover, via patterned growth of MWCNTs, the ultimate crack opening resistance of the CFRPs improved by 20%. To mimic the experimental behavior of the various CFRPs, a new methodology has been utilized to accurately simulate the unstable crack growth nature of CFRPs.

Several investigations reported the effects of adding nanomaterials - including CNTs - as a filler phase inside the matrix material, on the impact energy absorption of the hybrid FRPs. However, the impact mitigation performance of CFRPs based on ZnO nanorod grafted carbon fibers has not been reported. The dynamic out-of-plane energy dissipation capabilities of different hybrid composites were investigated utilizing high velocity (~90 m/s) impact tests. Comparing the results of the hybrid MWCNT/ZnO nanorod/CFRP with those of reference CFRP, 21% and 4% improvements were observed in impact energy absorption and tensile strain to failure of the CFRPs, respectively.

In addition to elevated stiffness and strength, CFRPs should possess enough tolerance not only to monotonic loadings, but also to cyclic loadings to be qualified as alternatives to traditional structural metal alloys. Therefore, the fatigue life (i.e. the number of loading cycles to failure) of CFRPs is of much interest. Despite the promising potential of incorporating nano-sized reinforcements into the CFRPs structure, not many studies reported on the fatigue behavior of hybrid CFRPs so far. In particular, there are no reported investigations to the effect of surface grown CNTs on the fatigue behavior of the hybrid CFRPs, due to fact that almost all the CNT

growth techniques (except for the GSD method) deteriorated the in-plane performance of the hybrid CFRPs. The hybrid ZnO nanorod grafted CFRPs have not been investigated under fatigue loading as well. In this dissertation, different hybrid CFRPs were tested under tension-tension fatigue to reveal the effects of the different nano-reinforcements growth on the fatigue behavior of the CFRPs. A remarkable fatigue damage tolerance was observed for the CFRPs based on uniform and patterned grown CNT fibers. Almost two decades of fatigue life extension was achieved for CFRPs based on surface grown MWCNTs.

Dedication

This dissertation is dedicated to my wife Fatemeh whose infinite love and encouragements inspired me to pursue and complete this research.

Acknowledgements

I would like to thank my advisor, Professor Marwan Al-Haik, for his great guidance, encouragement, and support over the past five years. I am really grateful and proud to have worked under his supervision. He set a great example for me to be a good researcher, a creative thinker, a patient mentor, a knowledgeable teacher and a real gentleman at the same time. I would also like to thank my committee members for their participation and support. I would like to express my special thanks to Professor Scott Case for his helpful discussions and guidance over my graduate career, especially for the last year.

I would like to thank Mac McCord and Danny Reed for helping anywhere and anytime I needed them for performing my experiments. I would also like to thank all my officemates for their help and teamwork, Tony Nelson, Masoud Safdari, Amir Alipour Skandani, Nejib Masghouni, Ramez Hajj, and especially Mehran Tehrani who has been a colleague and a brother to me, at the same time.

I would like to thank my parents and my brothers for their love and support. I would also like to thank my parents and brothers in-law for their kindness and love. I would also like to thank all my friends in Blacksburg whom I would call family, Farid, Sadeh, Faryan, Sajjad, Ali, Sima, Mohammad, Bahar, Reza, and Shima.

Table of Contents

List of Figures

List of Tables

Chapter 1. **Introduction**

1.1 Carbon Fiber Reinforced Polymer Composites

Due to their remarkable structural properties, carbon fiber reinforced polymer composites (CFRPs) are replacing traditional materials in a variety of structural applications. Composite bridge decks, civilian structures, gas pipelines and aerospace structures are few examples that capitalize on the CFRPs' exceptional mechanical properties, low thermal expansion, high resistivity to corrosion and light weight [1,2]. Carbon fiber reinforced composites possess outstanding in-plane modulus and strength along the fiber direction (on-axis), but exhibit inadequate mechanical performance along the other directions (i.e. in plane off-axis and out-of-plane). Understanding the failure of CFRPs provides an explanation to these deficiencies. When a composite laminate is subjected to an on-axis loading, beside fibers fracture, a possible failure mechanism is the inter-fiber fracture. The inter-fiber fracture includes cohesive matrix fracture and adhesive debonding of the fiber/matrix interface [3]. When CFRPs are transversely loaded, e.g. bending and impact, a common damage, which may occur prior to fibers fracture, is the interlaminar delamination [4]. In addition to out-of-plane loads, in-plane tension, compression and cyclic fatigue loadings could trigger the interlaminar cracks leading to induce the interlaminar delamination damages [4]. The interlaminar delamination deteriorates the in-plane mechanical performance of CFRPs and limits the life of the composite structure leading to sudden failures of the whole structure [4,5].

1.2 Hybrid CFRPs

Various remedies have been implemented to enhance the interlaminar properties of the CFRPs, e.g., stitching [6], fiber surface treatment [7], and interleaving with toughened polymer [4,8].

However, some of these methods, e.g. fiber chemical treatments, degrade the fiber and consequently wakens the in-plane mechanical properties of the CFRPs [4].

Alternatively, incorporating nano-sized reinforcement into the CFRPs' structures is a potential remedy for their insufficient out-of-plane performance [9]. Carbon nanotubes (CNTs) possess excellent physical and mechanical properties, and extremely high aspect ratios [4]. Hence, a great body of research is devoted to investigating the effects of using CNTs on the CFRPs' through-thickness and in-plane performance [4,9].

Several investigations were devoted to integrating CNTs as a filler phase into CFRPs using different routes. The most straightforward approach is to directly mix the CNTs with the polymeric matrix prior to manufacturing the CFRP [9]. Incorporating the CNTs into a polymer matrix was proven to improve the toughness, stiffness and creep resistance of the polymer [10-12], and the CNT-enriched polymer matrix in return improves the matrix-dominated mechanical properties of the CFRP. Soliman et al. [13,14] showed improvements in interlaminar shear strength, low velocity impact resistance, and in-plane on- and off-axis tensile strength of a 1.5wt% pristine and functionalized CNT containing CFRP.

Despite its straightforwardness, CNTs mixing methods encounter two major hurdles [4,9]:

1. The inherent tendency of the CNTs to agglomerate, which arises from a much stronger van der Waals forces between the CNTs themselves than between the CNTs and the polymer matrix. The agglomeration limits the consistent dispersion of CNTs over the entire matrix [15].

2. The extremely viscous CNT polymer matrix slurry (even with very small amounts of CNTs, ca. 1.0 wt%) hinders the matrix infusion through the fibers during manufacturing the CFRP.

1.2.1 Hybrid CFRPs with CNT grafted hierarchical fibers

In order to eliminate the problems associated with the CNT mixing method, grafting CNTs onto the carbon fibers surfaces could provide high concentration of CNTs where they are most needed, i.e. the immediate fiber/matrix interface, and in-between the different laminae of a CFRP [9]. CNTs can be grown over various substrates such as silicon, silica, and alumina [16]. In order to effectively utilize CNTs in CFRPs, CNTs should be grown directly on carbon fibers' surfaces; however, the in-situ growth of CNTs on carbon fibers is accompanied with several complications. First, the transition metals that are used as catalysts for CNT synthesis can easily diffuse into the fiber substrate. Second, the synthesis environments could facilitate the growth of different carbon species rather than CNTs [17].

The most common route utilized to grow CNTs over carbon fibers is catalytic chemical vapor deposition (CCVD) [4,18-23]. The working temperature range for CCVD falls between 700 and 1200 °C, making CCVD destructive to the carbon fiber substrate itself [22,23], leading to degraded mechanical properties of the CFRP. For example, Thostenson et al. [24] utilized the CCVD method to grow CNTs on carbon fibers at 700 °C and fabricated composites based on them. Significant degradation in the matrix/fiber interface was reported due to the exposure of the carbon fibers to elevated temperature growth conditions. Identically, Zhang et al. [19] employed the CCVD method to grow CNTs on a PAN-based carbon fiber fabric at 700-800 °C and reported a 40% reduction in the on-axis strength of the ensuing composites. However, while the fiber dominated mechanical properties diminished due to the elevated temperatures, the

matrix dominated properties, e.g. interlaminar shear strength (ILSS), showed some improvement [17,25].

Consequently, growing CNTs via CCVD on temperature-resistant fibers has been reported to achieve substantial improvements in mechanical properties. Veedu et al. [26] grew CNTs on SiC woven yarns, which are thermally resistant, using the CCVD method. They reported improvements of 348% in Mode I fracture toughness, 140% in flexural strength, 424% in flexural toughness, and 514% in damping capability of the hybrid composites compared to the ones made from raw SiC fabrics.

In order to minimize the damages induced by the CCVD elevated temperatures, a relatively novel protocol for grafting the MWCNTs on carbon fibers has been developed [27,28] which requires lower temperature (550 °C) than CCVD's to perform. This method, referred to as graphitic structures by design (GSD), was utilized in a recent investigation by the authors [29] and no significant degradation in on-axis and off-axis tensile properties of the hybrid CFRP was observed when employing GSD to grow certain topologies of CNTs. Furthermore, optimally patterned growing the CNTs over the carbon fiber surfaces resulted in 11% and 19% enhancements in on- and off-axis tensile strength of the hybrid CFRPs, respectively [29]. The out-of-plane performance of hybrid CFRPs reinforced with GSD grown MWCNTs was also improved [22], e.g. 56% improvement in flexural loss modulus. In a more recent study [30], utilizing the GSD patterned growth of CNTs over carbon fibers yielded a 127% improvement of the impact energy dissipation of a CFRP.

1.2.2 Hybrid CFRPs with zinc oxide nanorod grafted hierarchical fibers

In lieu of CNTs, other nano-sized reinforcing structures which can hybridize the CFRPs are zinc oxide (ZnO) nanorods. They can be radially grown on the surface of carbon fibers in order to create hierarchical reinforcements [31,32]. Different methods have been used so far in order to synthesize ZnO nanostructures; vapor-phase transport [33], metalorganic chemical vapor deposition [34], sputtering [35], molecular beam epitaxy [36], thermal evaporation [37] and vapor-liquid-solid [38]. Most of these methods require elevated temperatures, and therefore damage the fibers resulting in degraded in-plane mechanical properties. Furthermore, some of the aforementioned methods follow complex procedures and require advanced equipment. Alternatively, hydrothermal synthesis technique, which is a solution-based low temperature (70~90 °C) technique can successfully grow ZnO nanorods radially on the carbon fibers.

The hydrothermal method was used by Lin et al. [32] to whiskerize the carbon fibers with ZnO nanorods and more than 100% improvement in fiber/matrix interfacial shear strength was reported which proves the excellent enhancement in fiber/matrix adhesion which is a promising factor in both in-plane and out-of-plane performance of the CFRPs. For example, in recent investigations [39,40], via hydrothermally growing ZnO nanorods on woven carbon fiber fabrics, flexural vibration attenuation, and stress relaxation modulus of a hybrid CFRP were improved by 50% and 65%, respectively. Utilizing the same synthesis technique, interlaminar shear strength of a hybrid CFRP was also improved by 55% [41].

ZnO nanorods possess piezoelectric and semiconductor properties making the hybrid CFRPs suitable for numerous applications, e.g. solar cells, sensors, structural health monitoring (SHM) and energy harvesting devices [42-45]. In a recent study [46] the hydrothermal ZnO synthesis technique was utilized to manufacture hybrid CFRP beams for energy harvesting applications.

1.3 Interlaminar Fracture Toughness of Hybrid CFRPs

Since CFRPs possess different phases and their fabrication include various thermal and mechanical inputs, matrix (micro) cracks could exist inside their structure. Besides, some loadings (e.g. low velocity impacts) could initiate cracks inside CFRPs structure. Therefore, one of the most important mechanical and structural performance criteria for CFRPs is their resistance to fracture in the presence of a crack, namely fracture toughness. These cracks could occur in the interlaminar region and as mentioned before, low resistance of the CFRPs to hinder interlaminar crack propagation will lead to delamination damage, which is detrimental to the mechanical performance and life of the whole CFRP structure.

The delamination damage resistance in the FRPs can be evaluated by interlaminar fracture toughness in different modes: Mode I – crack opening mode where the delaminated faces open away from each other, Mode II – in-plane shear mode where a delamination grows due to an in-plane shear force or displacement perpendicular to the crack front, and Mode III: out-of-plane shear mode where the delamination grows due to an out-of-plane shear force or displacement parallel to the crack front.

There are a number of publications investigating the addition of nano-scale reinforcements inside polymer matrices and studying their effect on the fracture toughness behavior of the nano-sized filler reinforced polymers, namely nanocomposites [4,47-52]. For example, the fracture toughness of an epoxy resin showed a 43% improvement via adding 0.5 wt.% of double-walled CNTs (DWCNTs) [53]. In another study [54], the stress intensity factor of a tetra functional epoxy resin increased by 200% via dispersing 1.0 wt.% MWCNTs.

This promising performance of the CNT-enriched polymers in fracture toughness encouraged the researchers to investigate the effect of hybridizing the CFRPs with nano-reinforcements on their interlaminar fracture toughness. For example, Yokozeki et al. [55] improved the mode I interlaminar fracture toughness of a CFRP by 98% utilizing 5 wt.% cup-stacked CNT (CSCNT) mixing into its epoxy matrix. In another study, Godara et al. [56] separately mixed 0.5 wt.% MWCNTs and DWCNTs with epoxy matrices and the mode I interlaminar fracture toughness of the hybrid CRRPs improved by 75% and 33%, respectively. However, there are some cases in which mixing low contents of CNTs (e.g. 0.1 wt.%) led to decrease in the mode I interlaminar fracture toughness of the hybrid CFRPs [57,58]. In a recent study by Borowski et al. [59], the effect of adding carboxyl functionalized MWCNTs into the polymer matrix of a CFRP was investigated and a 25% improvement in interlaminar fracture toughness was observed.

Compared to the direct mixing method, more significant improvements in mode I and II fracture toughness of the hybrid FRPs were observed utilizing CNT growth methods on fibers. As mentioned before, Veedu et al. [26] utilized a CCVD approach to grow MWCNTs on SiC fibers and improved the mode I and II fracture toughness of their FRP by 348% and 54%, respectively. Wicks et al. [60] grew MWCNTs on top of alumina fibers and improved the mode I interlaminar fracture toughness by 67%.

While there are several studies detailing the effects of dispersed nanofillers on the fracture toughness of FRPs, no literature is detailing the effect of surface GSD grown CNTs and ZnO nanowire -on carbon fiber- on the fracture toughness of these hybrid composites. Besides, the literature lacks investigations on the effect of different CNT growth topologies over carbon fiber on the interlaminar damage resistance of hybrid CFRPs.

1.4 Finite Element Simulation of Interlaminar Crack Growth in Hybrid CFRPs

Delamination damage in laminated composites can be triggered by an impact loading or a manufacturing geometric discontinuity, e.g. ply drops, bonded joints, etc. and cause severe loss of structural performance and fatigue life of the FRPs [4,61]. Therefore, accurate prediction of fracture behavior in the interlaminar region of the FRPs is crucial. There are two major techniques for simulating the interlaminar crack propagation behavior of the FRPs using finite elements method (FEM); virtual crack closure technique (VCCT), and cohesive elements or cohesive zone modeling (CZM). VCCT, which was firstly proposed by Rybicki and Kanninen [61,62] applies a fracture mechanics technique to evaluate the energy release rates (G). The main assumption used in this technique is that the strain energy released as a crack propagates by a small amount is equal to the work needed to close the same crack. Depending on the crack propagation mode, the energy release rates of G_I, G_{II} and G_{III} can be computed using the nodal forces and displacements. This method can be effectively implemented via FE analysis by ABAQUS. This software package is capable of predicting the onset of crack initiation, as well as simulating stable and unstable crack propagation behavior [63]. However, for applying this method the initial crack front should be determined prior to the simulation, which could be very challenging to predict for complex crack geometries and loading situations [61]. Use of cohesive elements is an alternative way to simulate the interlaminar crack propagation phenomenon. Cohesive elements, which are based on Dugdale-Barenblatt cohesive zone approach [64,65], obey a strength-based failure criterion indicating the onset of crack softening process. Two major types of cohesive elements have been used in the literature; point cohesive elements, which are identical to non-linear spring elements [66,67], and continuous interface elements, which are finite- or zero-thickness volume elements connecting solid elements among which the fracture

grows [68,69]. Zero-thickness volume elements can also be implemented in FEM using ABAQUS. Although there are several reported investigations on simulating the interlaminar fracture of FRPs, to the best knowledge of the author, none has utilized FEM to examine the effect of surface grown nano-reinforcements on improving the interlaminar fracture resistance of hybrid CFRPs.

1.5 Impact Damage Mechanisms in Hybrid CFRPs

When a CFRP is subjected to an impact loading, the kinetic energy of the impactor transforms into three forms of energy: elastic strain energy inside the composites, dissipated energy from plastic deformations, and energy required to apply different damage modes. Since the CFRPs are brittle in nature, in addition to the energy dissipated through friction, a complex mixture of different energy absorbing damage mechanisms could occur; matrix cracking caused by transverse shear, fiber fracture, kinking referred to as trans-laminar fracture, and delamination mainly caused by mode II shear [4].

Various parameters in the impact damage could be considered as impact damage resistance of the CFRPs; e.g. maximum load, deflection to maximum load, absorbed energy, delaminated area, etc. [4]. CFRPs capable of dissipating more impact energies and retaining less delamination area are considered as more damage resistant CFRPs. Another energy dissipating mechanisms exclusive to the hybrid CFRPs are nano-whiskers' pull out and breakage [4]. The frictional forces between polymer matrix and high aspect ratio fillers (e.g. CNTs or ZnO nanorods) contribute to this energy dissipating mechanism. In general, high aspect ratios of one-dimensional nano reinforcements (e.g. ZnO nanorods and CNTs) provide large surfaces for frictional interactions inside the structure resulting in an increase the crashworthiness of the entire structure when the damage interacts with these nano-structures. Another energy

consuming mechanism that ZnO nanorods can contribute to stems from the coupling between the mechanical and electrical responses (i.e., piezoelectric response) of the ZnO crystalline structure when mechanically loaded. Some investigations reported the effects of adding nanomaterials, as a filler phase inside the matrix material, in impact performance of the hybrid FRPs. However, to the best knowledge the authors, CNT growth techniques has not ever been employed to improve the ballistic impact performance of the hybrid CFRPs. ZnO nanorod growth methods are relatively new in the field and their application in impact damage mitigation of hybrid CFRPs has not been reported yet.

1.6 Fatigue Performance of Hybrid CFRPs

In addition to elevated stiffness and strength, FRPs should possess enough tolerance under not only monotonic loadings, but also under cyclic loadings to be qualified as alternatives to traditional structural metal alloys. Therefore, the fatigue life of FRPs is of much interest. It is well known that the fatigue life in FRPs is controlled mostly by polymer matrix crack resistance; since the pre-fatigue cracks in the matrix will propagate and cause fibers' fracture, resulting in fatigue failure of the FRP [70]. Comparing the two mostly used fibers in FRPs, i.e. glass and carbon fibers, carbon fibers exhibit higher stiffness than the glass fibers. Therefore, when the FRPs are under on-axis loadings, for similar stresses in CFRPs and Glass FRPs (GFRPs) structure, GFRPs would experience higher strains. This elevated strain, when applied to the brittle polymer matrix, would initiate matrix cracks resulting in shortening the fatigue life of the GFRPs. Therefore, CFRPs are considered to be more resistant to on-axis high-cycle fatigue loading than GFRPs' [70-72]. However, the presence of geometrical discontinuities, and in general, stress raisers, e.g. voids, holes, warp-weft cross-overs in woven fabrics, etc., would trigger matrix cracks causing the fatigue damage to progress. Avoiding all the aforementioned

matrix crack initiators is almost unachievable during the fabrication and use of CFRPs. Hence, improving CFRPs' fatigue life using alternative routes is crucially needed.

There are some investigations on the effect of incorporating the nano-sized reinforcements on the fracture toughness of polymer nanocomposites. It was reported that fatigue crack growth resistance of the polymer matrices could be improved via adding nano-reinforcements, e.g. CNTs, etc. For example in a relatively recent study by Bortz et al. [73], well-dispersed graphene oxide nano-sheets improved the mode I fracture toughness of an epoxy by 28-110%. A significant improvement of 1580% in fatigue life of the nanocomposite was also observed. The graphene oxide nano-sheets' capabilities in pinning the fatigue cracks inside the polymer was the basis for this extended fatigue life.

Despite this huge potential of incorporating the nano-sized reinforcements into the CFRPs structure, there are not many studies reported on the fatigue behavior of hybrid CFRPs so far. Grimmer and Dharan [70] dispersed 1.0 wt.% of MWCNTs in an epoxy matrix, and although there were no changes observed in the tensile strength of the GFRPs, significant life improvement was observed in their tension-tension life. Davis et al. [74] utilized special CNTs in different weight percentages, in order to make hybrid CFRPs. They reported 1-2 orders of magnitude improvements in tension-tension fatigue life of the CFRP via incorporating 0.3 wt.% of fluorine XD-CNTs. However, they observed no improvement in fatigue life for CNTs contents of 0.2 wt.% or less, hinting that this CNT content was not sufficient for hindering the fatigue crack growth inside the matrix. In a recent investigation by Knoll et al. [75], incorporating 0.3 wt.% MWCNTs, improved the fatigue life of a hybrid CFRP by 5 folds. The well dispersion of the nano-reinforcements is crucial in fatigue performance of the hybrid FRPs. For example, in a recent study [76], incorporating 0.5 wt.% MWCNTs showed no improvement,

while adding 1.0 wt.% MWCNTs led to significant degradation in the fatigue life of a hybrid GFRP.

The interlaminar fatigue performance of hybrid FRPs was also investigated. One of the pioneering works was carried out by Grimmer and Dharan [77], where they incorporated 1.0 wt.% MWCNTs and fabricated hybrid GFRPs. The cyclic mode I crack propagation rate decreased significantly, while improvements in monotonic fracture toughness was reported to be less than 5.0%. In a recent study, Fenner and Daniel [78] utilized 0.5 wt.% MWCNTs and reported order of magnitude improvement in interlaminar shear fatigue life of a hybrid CFRP. They also reduced the interlaminar fatigue crack growth rate by a factor of 2.0.

Literature review suggests that the effect of surface grown CNTs on the fatigue behavior of the hybrid CFRPs has not been investigated; mostly due to the fact that almost all the CNTs growth techniques (except for the GSD method) deteriorated the in-plane performance of the hybrid CFRPs. Furthermore, the hybrid ZnO nanorod grafted CFRPs have not been investigated under fatigue loading either.

1.7 Outlines of the Dissertation

In the second chapter, two different techniques are utilized to pre-deposit the ZnO growth initiation layer on the surface of carbon fibers: ZnO nanoparticles/solution mixture airbrush spraying, and magnetron sputtering. In both techniques, carbon fibers with pre-deposited ZnO layer undergo the hydrothermal ZnO nanorod synthesis technique. It is shown that, the carbon fibers pre-coated by the airbrush spraying method yielded a forest of randomly aligned ZnO nanorods, while the fibers pre-coated by the sputtering technique exhibited radially aligned ZnO nanorods forests. Hybrid CFRPs are fabricated based on the aforementioned carbon fiber fabrics

and tested via quasi static tension and 3-point bending dynamic mechanical analysis (DMA) to examine the effect of ZnO nanorods growth alignment on the hybrid CFRPs' mechanical behavior.

In the third chapter, carbon fibers underwent two different nano-reinforcements synthesis techniques to make hierarchical reinforcements; GSD method to grow MWCNTs and (b) hydrothermal technique to grow ZnO nanorods over the carbon fibers. The carbon fibers with surface grown ZnO nanorods or CNTs are utilized to fabricate hybrid CFRPs. Double cantilever beam (DCB) tests are performed to investigate the effect of the surface grown nano-reinforcements on the Mode I interlaminar fracture toughness (G_{Ic}) of the hybrid CFRPs.

In chapter 4, FEM is employed to simulate the interlaminar crack growth behavior of the hybrid CFRPs under Mode I crack opening loading conditions embodied by the DCB tests of chapter 3. ABAQUS is utilized to perform the numerical simulations. First, utilizing the VCCT, preliminary FE models are developed to attain optimum mesh size and number of load increments. VCCT-based FE models are established for different samples configurations as tested in the experimental studies. Mode I interlaminar fracture toughness values utilized in these FE models are average values taken from the experimental measurements of the corresponding sample. In another set of simulations, cohesive elements are used to simulate the interlaminar crack propagation behavior of the hybrid CFRPs to study the effect of different surface treatments on the CFRPs' interlaminar strength against crack propagation, as well as their ultimate crack opening. Due to the nature of woven CFRPs, unstable crack growth behavior was observed in the DCB experiments of chapter 3. In order to simulate such crack propagation behavior, the fluctuations in the interlaminar fracture toughness values along the crack length are taken into account and another VCCT-based set of simulations are performed.

In chapter 5, an experimental investigation on the impact performance and damage resistance of especially designed CRRPs is presented. A hydrothermal ZnO nanorod synthesis technique is used to make hybrid ZnO nanorod-carbon fiber fabric reinforcements. GSD method is also used to grow MWCNTs over carbon fiber fabrics and ZnO nanorods. Hybrid CFRPs based on the designed configurations are fabricated and tested to illustrate the effect of different nano-reinforcement synthesis factors (Hydrothermal and GSD methods' environments, existence of grafted nano-whiskers, etc.) on the mechanical behavior of the hybrid CFRPs. The designed CFRPs are tested via tension, high velocity (~90 m/s) and quasi static spherical punch tests.

In chapter 6, the carbon fibers with surface grown ZnO nanorods or CNTs are utilized to fabricate hybrid CFRPs. The CFRPs are examined under monotonic tensile loading to obtain their tensile strengths, as well as their elastic moduli and strain-to-failures. The designed CFRPs are also tested under tension-tension fatigue to reveal the effects of the different nano-reinforcements growth on the fatigue behavior of the CFRPs. Stress-life (S-N) curves are obtained at three stress levels under a cycling stress ratio of 0.10.

In all the experimental studies, scanning electron microscopy (SEM) is utilized to capture the fractographs of the tested CFRPs to reveal the different damage mechanisms under different loading condition, and to reveal the nano-reinforcements contribution in the damage mitigation.

Finally, in the last chapter, a summary and conclusions from all the investigations are presented. Furthermore, future work is proposed to promote the application of hybrid CFRPs.

Chapter 2. **Hybrid ZnO nanorod grafted carbon fiber reinforced polymer composites; randomly vs. radially aligned ZnO nanorods growth**

2.1 Overview

Integrating nano-sized reinforcing materials into carbon fiber polymer composites (CFRPs) has been reported by many investigations to enhance various mechanical performances of the CFRPs; e.g. fiber/matrix interfacial strength, delamination resistance, vibration attenuation capabilities, etc. Utilizing various synthesis techniques, ZnO nanorods can be grown on the surface of carbon fibers to make hybrid reinforcements. Hydrothermal synthesis technique is one of these methods, which requires the deposition of a thin layer of ZnO on top of the carbon fibers to seed the ZnO nanorods growth. Depending on the method by which the seeding ZnO layer is deposited, the grown ZnO nanorods could display different morphologies on the surface of carbon fibers. In this chapter, two different techniques are utilized to pre-deposit the ZnO growth initiation layer on the surface of carbon fibers: ZnO nanoparticles/solution mixture airbrush spraying, and magnetron sputtering. In both techniques, carbon fibers with pre-deposited ZnO layer underwent the hydrothermal ZnO nanorod synthesis technique. The carbon fibers pre-coated by the airbrush spraying method yielded a forest of randomly aligned ZnO nanorods, while the fibers pre-coated by the sputtering technique exhibited radially aligned ZnO nanorods forests. Hybrid CFRPs were fabricated based on the aforementioned carbon fiber fabrics and tested via quasi static tension and 3-point bending dynamic mechanical analysis (DMA). The in-plane tensile strength of the hybrid CFRPs were improved by 18% for the composite based on randomly oriented ZnO nanorods over the carbon fibers. The loss tangent of the CFRPs, which

indicates the damping capability, increased by 28% and 19% via radially and randomly grown ZnO nanorods, respectively.

2.2 Introduction

Fiber reinforced polymer composites (FRPs) possess excellent specific strength and stiffness along the fibers' direction. However, they lack sufficient out of plane and off-axis in-plane mechanical performance [2]. Several studies were carried out to enhance the FRPs' poor out of plane mechanical performance, e.g. stitching [6], interleaving with toughened polymer [4,8], fiber surface treatment [7], etc. However, improvements in the out-of-plane performance were at the expense of losing the in-plane mechanical properties of the CFRPs [4]. Alternatively, utilizing nano-sized reinforcing materials in the FRPs' structure is a promising method to improve the out-of-plane performance of the FRPs, and simultaneously, to minimize the negative effects on their in-plane properties. Carbon nanotubes (CNTs) [4,9], graphene nano-platelets (GNPs) [79-81], nano-sized ceramic structures (e.g. ZnO [39,41], SiO_2 [82-85]), etc., are among the nano-fillers utilized in order to improve the mechanical performance of the hybrid FRPs.

Common approach to integrate the nano-fillers into FRPs' structure include mixing the fillers into the matrix phase prefabricating the composite laminates [9]. This method essentially modifies the matrix material via nano-additives. Although some improvements in matrix dominated properties were achieved [9,86], utilizing high volume ratios of nano-fillers can be severely limited by the difficulty of dispersing them into polymeric matrices [15]. For example, in the case of CNTs, their inherent tendency to agglomerate limits the achievable mixing weight percent to less than 3.0 wt.% [22,87]. The CNTs agglomerates disprove the mechanical performance of the host matrix, as they provide possible stress concentration locations inside the host material. In addition, mixing a minute weight percent of CNTs into a polymeric matrix

dramatically increases the polymer's viscosity preventing the matrix from defusing in-between the fibers during the composite fabrication process [9].

In order to avoid the dispersion problems associated with the mixing methods, nanostructures can be alternatively grown over the surface of fibers before fabricating the composites. This approach produces hybrid hierarchical reinforcements, potentially capable of providing the composites with a stronger fiber/matrix interface. However, some growth methods could be destructive to the fibers, resulting in poor in-plane mechanical performance of the hybrid FRPs. As an example, chemical vapor deposition (CVD) is the most common approach to grow CNTs, which requires relatively high temperatures (700-1100 °C). This temperature range has destructive effects on the in-plane mechanical performance of the FRPs; both glass and carbon fibers are sensitive to these elevated temperatures [19,22]. An alternative method for CVD, graphitic structures by design (GSD), which utilizes relatively low temperatures (550 °C) [27,28], has been reported to improve in-plane and out-of-plane mechanical performance of the CFRPs [22,29,30]. However, GSD still moderately induces damage to the in-plane mechanical performance of FRPs based on glass fibers (GFRPs) [88].

Similar to CNTs, ZnO nanorods can be grown over fibers to produce hybrid reinforcements [31,32]. In addition to mechanical benefits, ZnO is a semi-conductive and piezoelectric material. These unique characteristics of ZnO facilitate their application in energy harvesting and structural health monitoring of the hybrid FRPs [46,89,90]. There are several techniques to synthesize ZnO nanorods; vapor-phase transport [33], metalorganic chemical vapor deposition [34], sputtering [35], molecular beam epitaxy [36], thermal evaporation [37] and vapor-liquid-solid [38,91]. Most of these methods employ elevated temperatures, which are destructive to carbon fibers, and require complex synthesis setup. Alternatively, hydrothermal synthesis is a

low temperature (~90 °C) solution-based technique, capable of successfully growing ZnO nanorods over carbon fibers [31,32]. Employing this technique yielded improvements in fiber/matrix interface shear strength [32], interlaminar shear strength [41], vibrations attenuation [39,41], in-plane on-axis and off-axis tensile strengths [41,92], creep behavior [40] and high-velocity impact energy dissipation [92] of CFRPs.

This method requires a pre-deposited ZnO layer on top of the fibers; providing initiation seeds for growing the ZnO nanorod crystals. The morphology and dimensions of the grown ZnO nanorods can be tuned by employing different concentrations of chemicals inside the solution, temperature, time of the growth process, and the way the initiation seeds are pre-deposited [93].

In the present work, two different methods were employed to deposit the initial ZnO layer over carbon fibers. The first method utilizes a magnetron sputtering technique to uniformly cover up the fibers' surfaces with a thin layer of ZnO before exposing the deposited fibers to the ZnO nanorods growth environment. The other method involves spraying a mixture of ZnO nanoparticles over the carbon fiber fabrics and allowing the solvent to evaporate in order to form a thin layer of ZnO nanoparticles over carbon fibers. Specific chemical concentrations, temperature and time of the ZnO growth process were chosen for the ZnO nanorod growth process in order to reach long ZnO nanorods (~2.5 μm). The chosen pre-deposition methods resulted in two different morphologies of ZnO nanorod forests over the carbon fibers.

Field emission scanning electron microscopy (FE-SEM) was employed to investigate the quality of the grown ZnO nanorods over the carbon fibers. The sputtering based method grows radially aligned ZnO nanorods around carbon fibers, while in the solution spraying method ZnO nanorods are grown randomly oriented but still attached to the carbon fibers.

Hybrid CFRPs based on these surface grown ZnO/carbon fibers were fabricated and tested under quasi static in-plane tension to examine the effect of ZnO nanorod alignments on the tensile stiffness, strength and strain-to-failure of the hybrid CFRPs. A 3-point bending dynamic mechanical analysis (DMA) test was employed to investigate the damping characteristics of the hybrid CFRPs. The fractographs of the hybrid composites after tension tests were taken from two different angles in order to investigate the hybrid CFRPs' behavior during the mechanical failure and effect of different ZnO nanorods morphologies on the damage mechanisms occurring in the interlaminar region.

2.3 Materials and method

2.3.1 ZnO layer pre-deposition

Un-sized plain-woven SGP196 (IM7-GP, provided by Hexcel Inc.,) carbon fiber fabric (6 K filaments count in a tow) was used as the main reinforcements. Square samples of 130 × 130 mm^2 were cut from the fiber fabrics along the warp and weft directions.

In order to pre-deposit the initial ZnO layer over the carbon fibers, two methods were employed. In the first method, an ATC Orion high vacuum sputtering system (AJA international, Inc.) was utilized to deposit a 75 nm thick layer of amorphous ZnO on both sides of the square fabric samples under 3 mTorr pressure of argon gas where 140 W of power was supplied to the sputtering target.

In the second method, 300 mg of ZnO nanoparticles (Nano Tek 40-100 nm APS powder, Alfa Aesar) were dispersed in 300 ml dimethylformamide (DMF) and 3 ml Triton X-100 (TX-100, Alfa Aesar). The mixture was homogenized via a Vibra-Cell VCX 500 tip ultrasonic processor for a total of 2 hours at amplitude of 40%. The mixture was allowed to set for 24 hours to make

sure that the solution was stable. Then, it was sprayed on both sides of carbon fiber fabrics using an airbrush. Ten layers of the mixture were sprayed over each side of carbon fiber samples starting from a different direction for each layer in order to attain a uniform coverage. There were two-minute gaps between spraying cycles to allow evaporation of DMF to prevent agglomeration of nanoparticles. To ensure complete evaporation of DMF, sprayed samples were kept for 24 hours at 60 °C. Using the two aforementioned different methods, the ZnO pre-deposited carbon fiber fabrics were prepared for the hydrothermal ZnO nanorod synthesis process.

2.3.2 ZnO nanorod synthesis method and composites fabrication

The hydrothermal synthesis technique utilizes an aquatic solution of zinc acetate dihydrate ($Zn(O_2CCH_3)_{22}H_2O$) and hexamethylenetetramine (HMTA) in deionized (DI) water using 30 mM concentrations of each chemical. In order to grow ZnO nanorods, the pre-coated samples were immersed in the abovementioned solution and kept in a convection oven at 85 °C for 8 hours. For unraveling the effect of exposing the fabrics to the hydrothermal environment, some ZnO pre-coated samples were soaked in pure DI water and heated up to 85 °C for 8 hours. Figure 2-1 illustrates the steps taken in order to grow ZnO nanorods over carbon fibers utilizing the hydrothermal synthesis technique.

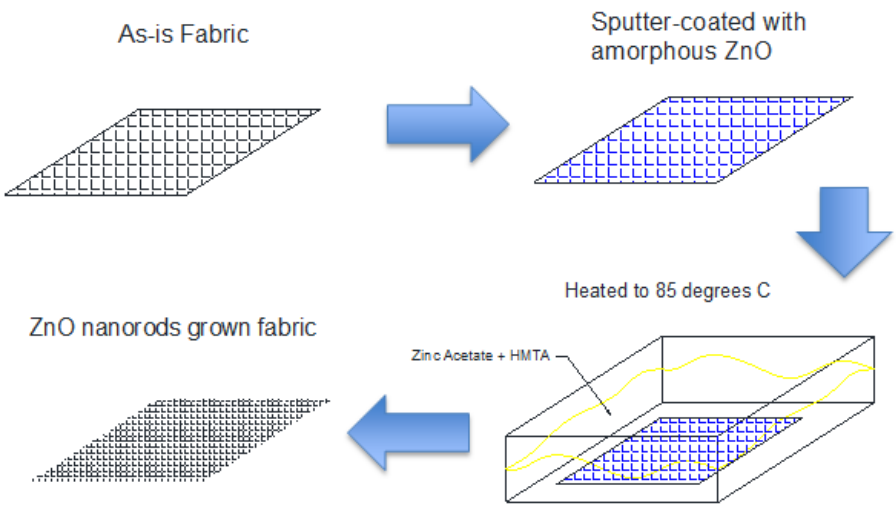

Figure 2-1. Schematic of the steps towards hydrothermal synthesis of ZnO nanorods over carbon fibers

After completion of the synthesis process, the fibers were rinsed using DI water and dried overnight in the same oven at 85 °C. At the end of the surface treatments on the fibers, five distinctive sample configurations were achieved; their designation and the process they underwent are listed in Table 2-1.

Table 2-1. Different designed sample configurations

Label	***Treatment undergone***	**Nano-reinforcements grown**
R	*As-received carbon fiber fabric (reference)*	none
SW	*Reference, pre-coated with sputtering method, immersed in hot water.*	none
SWZ	*Reference, pre-coated with sputtering method, hydrothermal ZnO nanorod growth.*	Radially aligned ZnO nanorods
AW	*Reference, pre-coated with airbrush spray method, immersed in hot water.*	none
AWZ	*Reference, pre-coated with airbrush spray method, hydrothermal ZnO nanorod growth*	Randomly oriented ZnO nanorods

The composite fabrication was carried out utilizing a vacuum- and pressure-assisted hand layup system. Aeropoxy™ (PTM&W Industries Inc.) that comprises a resin (PR2032), and a hardener (PH3665) was used as the polymer matrix in order to fabricate the designed hybrid CFRPs. The composite laminates comprised 3 layers from the fabrics listed in Table 2-1. The fabrics and composite laminates were weighed before and after fabrication, and knowing the density of the carbon fibers and matrix epoxy, the fiber volume fractions were calculated. The fiber volume fractions of the fabricated CFRPs are listed in Table 2-2.

Table 2-2. Fiber volume fractions of composite laminates and their thickness

CFRP sample label	R	SW	SWZ	AW	AWZ
V^f (%)	56.4	52.4	53.0	55.0	52.4

2.3.3 Characterization

In order to examine the quality of the grown ZnO nanorods over the carbon fibers, a 5200 Hitachi FE-SEM electron microscope operating at 5 kV was used. For the tension tests, tensile coupons of 125.0 × 12.5 mm^2, and for the DMA tests, samples of 40.0 × 12.5 mm^2 were cut from the fabricated composite panels. The tensile tests were carried out following the ASTM-D3039/D3039M-08 standard [94], utilizing an Instron® 4400R testing frame under 1.0 mm/min constant crosshead speed. An MTS extensometer was used to record the strain. The stress vs. strain data for different test coupons were recorded and analyzed in order to report the samples' elastic modulus, ultimate strength and strain to failure. The DMA tests were performed utilizing a DMA Q800 (TA Instruments, Inc.) at 30°C, over the frequency range of 1–32 Hz. Tensile and DMA tests were performed on six and four samples, respectively, from each configuration.

2.4 Results and discussions

2.4.1 Scanning electron microscopy of the synthesized ZnO nanorods

The morphology of the ZnO nanorods grown on the surface of the carbon fibers is shown in the SEM micrographs of Figure 2-2. Radially aligned ZnO nanorods, shown in Figure 2-2(a), have more persistent dimensions, shown in Figure 2-2(b), while the randomly aligned ZnO nanorods possess verities of lengths and diameters. However, they are successfully grown on and attached to the carbon fibers. The inset micrographs are higher magnification views showing the dimensions of the ZnO nanorods grown using the corresponding synthesis methods.

The different morphologies of the grown ZnO nanorods over carbon fibers arise from the difference in their pre-coated ZnO layer. The magnetron sputtering is inherently a relatively slow rate deposition method where angstrom-sized particles of ZnO are detached from target material by the plasma's accelerated argon ions and sit on the surface of carbon fibers. These ZnO particles form a relatively uniform layer over the carbon fibers. This uniform ZnO layer provides a consistent initiation seeds for the growth of ZnO nanorods during the hydrothermal process, consequently, resulting in uniform radially aligned nanorod forests. This controlled morphology would provide more ZnO surface area available for the polymer matrix to defuse in, producing strong interlocking mechanism between the ZnO nanorod forest and the matrix material in a CFRP laminate. In contrast, in the spraying method, nano-sized particles were sprayed over carbon fibers. These particles possessed random orientations and size distribution (40-200 nm) providing nonuniform growth seeds for the hydrothermal process; leading to ZnO nanorods forest random in size and orientation.

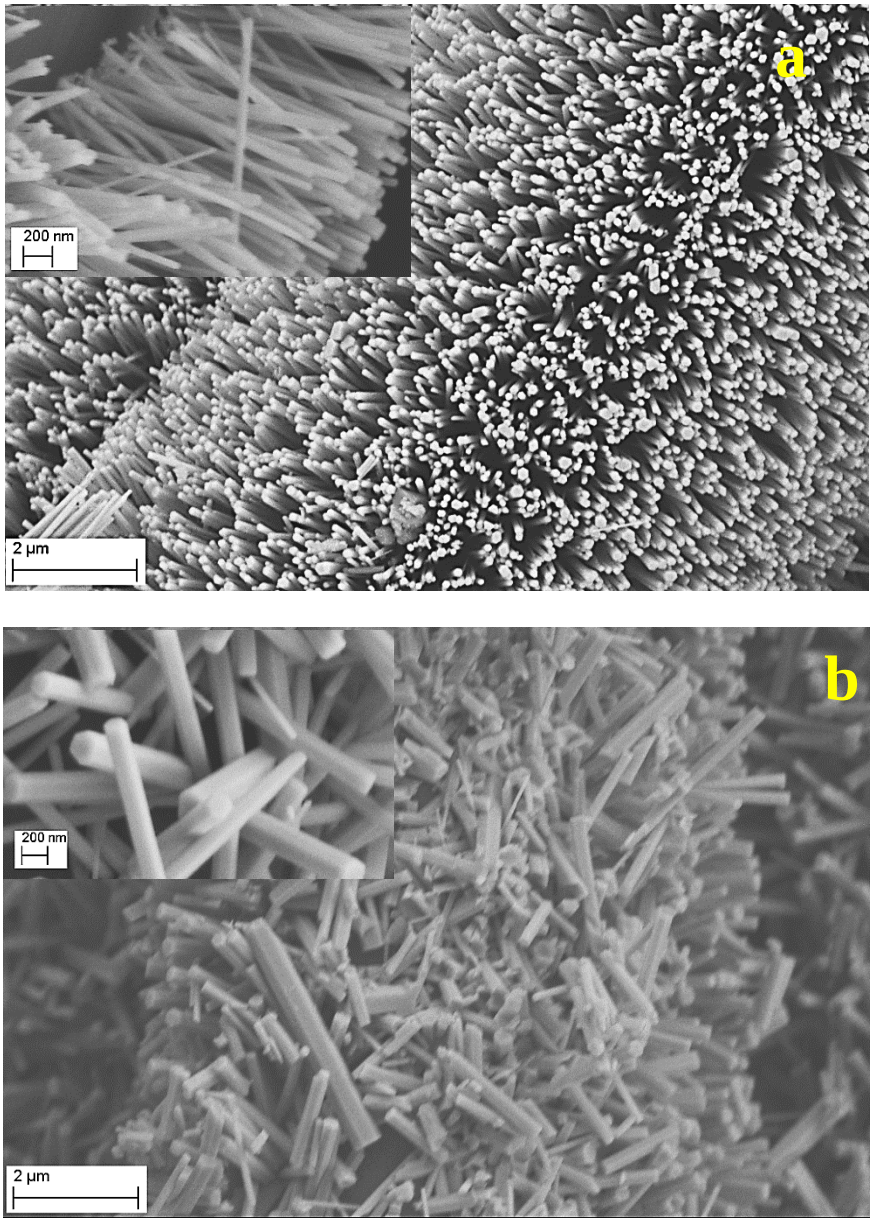

Figure 2-2. Scanning electron microscope micrographs of (a) radially and (b) randomly aligned ZnO nanorods over carbon fibers.

2.4.2 In-plane tensile performance of the designed hybrid ZnO nanorods-CFRPs

Representative stress vs. strain curves for the designed CFRPs, obtained from the tension tests, are illustrated in Figure 2-3. Figure 2-4 reports the average values and the standard deviations for the CFRPs' (a) elastic modulus, (b) tensile strength, and (c) strain to failure. The slope of the

stress vs. strain curves of the CFRPs up to the strain value of 0.30% was considered as their elastic moduli. The tensile strength of the designed CFRPs was considered to be the maximum stress value in the stress vs. strain data, and the strain to failure to be the strain value at the last data point of the curves.

There is a slight decrease in elastic moduli of the CFRPs based on the fibers exposed to water. Although the fibers were heated for 24 hours to eliminate water, this drop in stiffness still can be due to existence of moisture content inside the laminates.

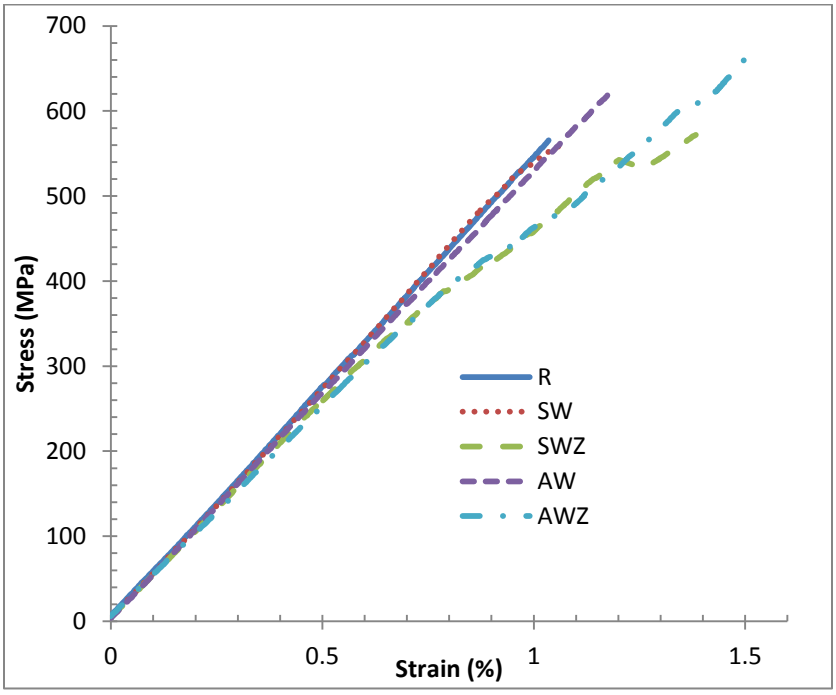

Figure 2-3. Representative stress vs. strain curves for the CFRPs based on R (as-received), SW (pre-coated with sputtering method and immersed in hot water), SWZ (pre-coated with sputtering method, hydrothermal ZnO nanorod growth), AW (pre-coated with airbrush spray method, immersed in hot water), and AWZ (pre-coated with airbrush spray method, hydrothermal ZnO nanorod growth) fibers.

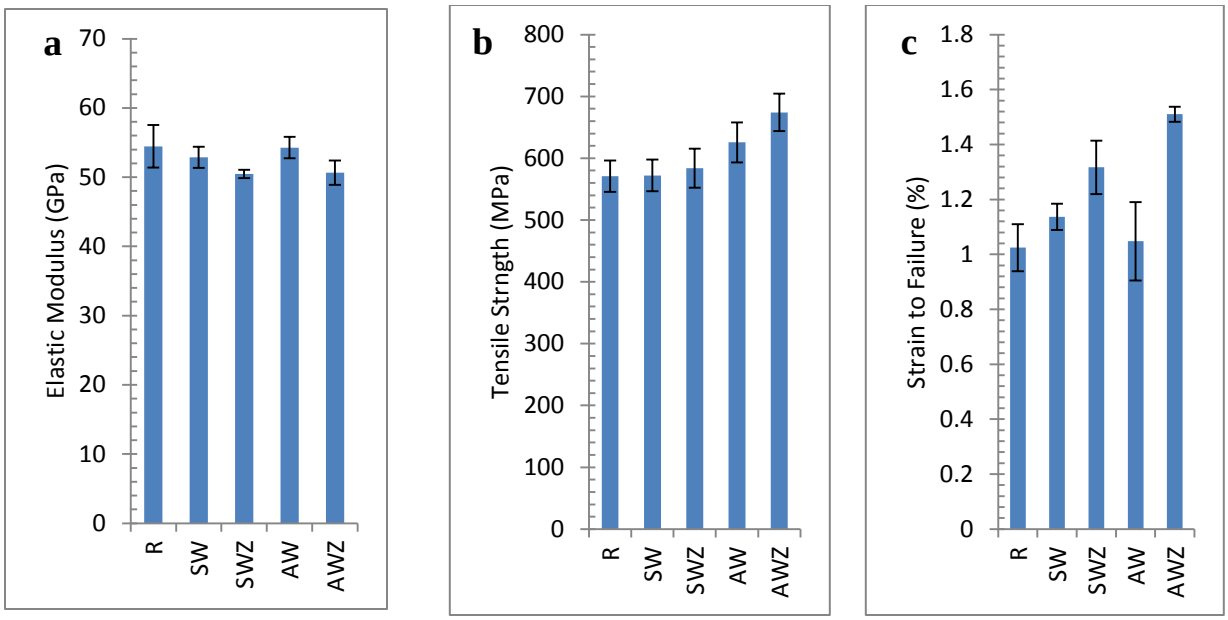

Figure 2-4. Average values of the (a) elastic modulus, (b) tensile strength, and (c) strain to failure, for the CFRPs based on R (as-received), SW (pre-coated with sputtering method and immersed in hot water), SWZ (pre-coated with sputtering method, hydrothermal ZnO nanorod growth), AW (pre-coated with airbrush spray method, immersed in hot water), and AWZ (pre-coated with airbrush spray method, hydrothermal ZnO nanorod growth) fibers.

Inferred from Figure 2-3, all the CFRPs showed initial linear-elastic behavior up to the strains around 0.4%. However, as load increases their behavior deviates from linearity due to initiation of matrix cracking and some individual fiber breakages. The cracks in the matrix could propagate towards the fibers increasing stress intensity close to the fibers causing fiber breakage (more apparent in the CFRPs with no ZnO nanorods; i.e. R, SW and AW sample configurations), unless the crack is stopped or deflected by the ZnO nanorods forest in the fiber/matrix interface region (such as the CFRPs with surface grown ZnO nanorods; i.e. SWZ and AWZ). In the case of individual fiber breakage, the stress transfer mechanism through the matrix in the fiber/matrix interface region aids the composite to withstand the load. The surface grown ZnO nanorods provide stronger fiber/matrix interface, thereby, help the hybrid CFRPs to resist the failure up to higher strains, and therefore to exhibit more ductile behavior than the CFRPs with no nano-

reinforcements. Hence, the samples with ZnO nanorods; SWZ and AWZ, show enhancements in the strain to failure compared to the reference CFRPs (R) by 28% and 47%, respectively (Figure 2-4(c)).

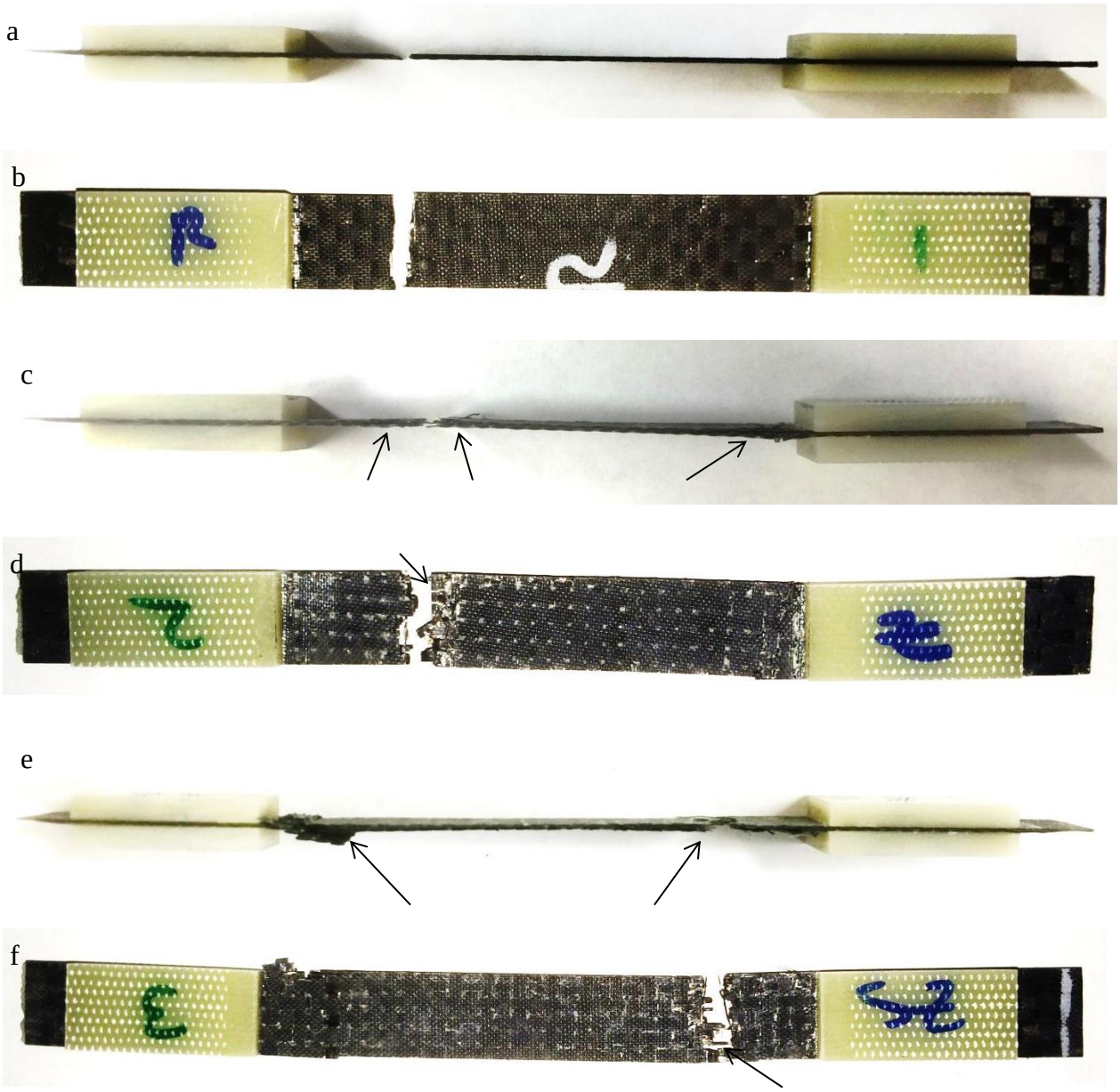

Figure 2-5. Fractured tensile samples from side and front views of the CFRPs based on (a and b) R, (c and d) SWZ, and (e and f) AWZ fibers. The delaminated regions are pointed with arrows.

This strong fiber/matrix region produced by randomly aligned ZnO nanorods in the AWZ samples improved the strength of the reference CFRPs by 18%. However, when bonding between the matrix and the surface grown ZnO nanorods forest is stronger than the bonding between the ZnO nanorods forest and the fibers, stress transfer mechanism can detach the nanorods forest from the surface of the fibers, producing local delamination failure as shown in Figure 2-5 (c-f). Delamination failure has a negative effect on the final strength of the FRPs. The delaminated areas were vaster for the hybrid CFRPs with radially aligned ZnO nanorods (SWZ) than for the ones with randomly aligned ZnO nanorods (AWZ). Hence, the SWZ based CFRP possess less strength than the CFRP based on AWZ. However, the CFRPs based on radially aligned ZnO nanorods were still slightly stronger than the reference CFRPs (R).

2.4.3 Dynamic mechanical performance of the designed hybrid ZnO nanorods-CFRPs

The average storage modulus and loss tangent (tan δ) values of the designed CFRPs, measured at 9 different frequencies, ranged from 1-35 Hz, are shown in Figure 2-6. Standard deviations of the measurements are also embodied by error bars on the data points. As shown in Figure 2-6(a), the storage moduli of the CFRPs were almost independent of the frequency. However, small increase in their values can be observed as the frequency increases. Comparing the average storage modulus values over all the input frequencies for individual sample configurations, 7.9% and 4.0% drops in storage moduli of the CFRPs was observed via growing radially and randomly aligned ZnO nanorods (i.e. SWZ and AWZ), respectively. These values are close to the reduction in elastic moduli of the same sample configurations in tensile tests. As explained earlier, this observation can be attribute to the existence of moisture in their structure, most likely trapped between the nanorods, as this drop was not evident for the samples with no nano-reinforcements.

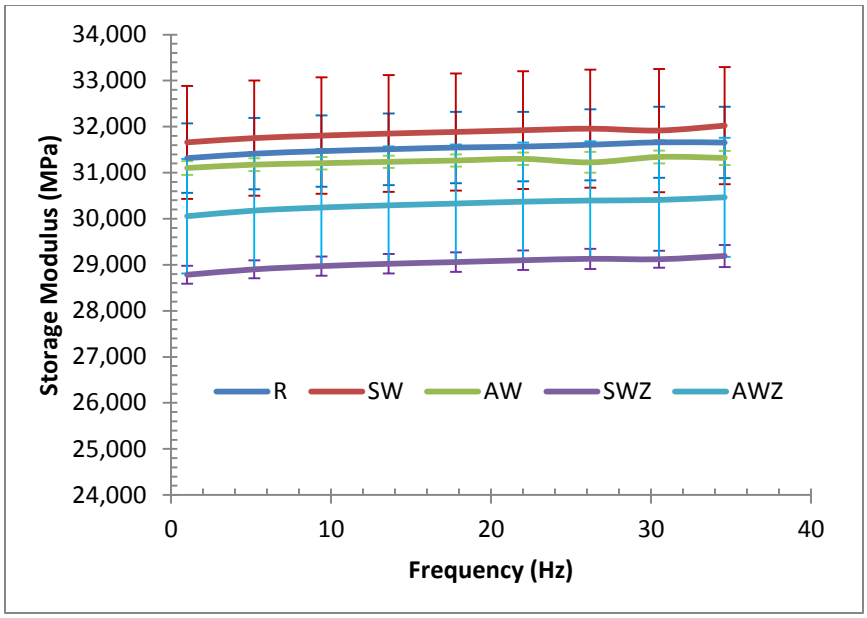

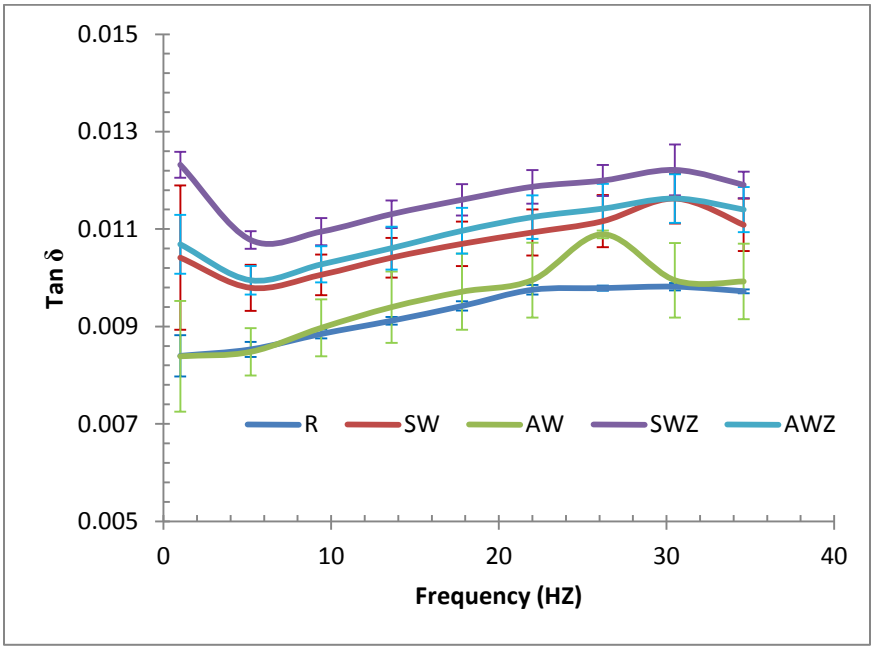

Figure 2-6. Storage modulus (a) and loss tangent (b) for the CFRPs based on R (as-received), SW (pre-coated with sputtering method and immersed in hot water), SWZ (pre-coated with sputtering method, hydrothermal ZnO nanorod growth), AW (pre-coated with airbrush spray method, immersed in hot water), and AWZ (pre-coated with airbrush spray method, hydrothermal ZnO nanorod growth) fibers.

Unlike storage modulus, loss tangent is highly dependent on the frequency, since this characteristic is driven by the viscoelastic behavior of the material. As shown in Figure 2-6(b) at

the frequency of 1Hz, the CFRPs comprising radially aligned ZnO nanorods (SWZ) had the highest loss tangent among all the CFRPs configurations. In comparison to the reference sample (R), this configuration exhibited 47% improvement in damping parameter of the CFRPs. At the same frequency, the CFRPs with randomly aligned ZnO nanorods exhibited 27% enhancement in damping compared to the reference configuration. Although the improvement in damping capabilities of the CFRPs is more pronounced at lower frequencies, taking the average of the loss tangent values over the measured frequency range, the improvements of 26% and 18% were observed for the composites with radially aligned and randomly aligned ZnO nanorods, i.e. SWZ and AWZ configurations, respectively. The mechanism responsible for this enhancement in damping can be the frictional slippage between the ZnO nanorods and the polymer matrix, as well as energy dissipation originated from the electromechanical coupling of the piezoelectric ZnO nanorods [39,95]. The outstanding energy dissipation through surface friction for the ZnO grown samples is due to the high surface area introduced by the high aspect ratio ZnO nanorods into the CFRPs structure. However, to some extent, energy dissipation through friction between fibers and pre-coated ZnO layer is evident from enhancement in loss tangent for AW and SW configurations. This improvement is more pronounced for SW sample in which magnetron sputtering method was used. Comparing the two designed CFRPs with ZnO nanorods, the one with radially aligned ZnO nanorods contributed more in vibration attenuation. More ZnO nanorod/matrix interface surface offered by this morphology (inferred from SEM micrographs of Figure 2-2), can be the reason for the higher damping improvement of the CFRPs based on SWZ fibers than the ones based on AWZ.

2.5 Conclusions

Two methods were utilized to pre-deposit a thin layer of ZnO on the surface of the woven carbon fiber fabrics. These two methods comprised (a) ZnO magnetron sputtering, and (b) airbrush spraying of dispersed ZnO nanoparticles/solvent mixture techniques. The pre-coated carbon fibers underwent a hydrothermal ZnO nanorods synthesis process. As a result of the different pre-coating techniques, different morphologies of ZnO nanorods forests were grown over the carbon fibers. Radially aligned ZnO nanorods were achieved utilizing the sputtering technique for pre-coating the fibers, while randomly aligned nanorods were grown using the airbrush spraying method.

Hybrid carbon fiber reinforced polymer composites based on the ZnO nanorod grown carbon fiber fabrics were fabricated and tested via quasi-static tension and 3-point bending dynamic mechanical analysis testing. The CFRPs possessing randomly aligned ZnO nanorods illustrated outstanding improvements in the CFRPs in-plane strength (18%) and strain to failure (47%), due to their strong fiber/matrix interface region. However, lesser improvements in strength and strain-o-failure of the CFRPs were achieved via radially grown ZnO nanorods. The long, thin, and controlled ZnO nanorods morphology provided stronger adhesion between the ZnO nanorods and polymer matrix than the adhesion between the ZnO nanorods and carbon fibers. This characteristic caused the CFRPs with radially aligned carbon fibers to show local delamination failure right before the final fracture.

The radially aligned ZnO nanorods introduce larger surface area to the CFRPs structure than the randomly aligned ones. Therefore, vibration attenuation capabilities of the CFRPs with radially aligned ZnO nanorods were higher than the ones with randomly aligned ZnO nanorods. As a

result of DMA tests, loss tangent of the CFRPs were improved by 26% and 18% via growing radially and randomly aligned ZnO nanorods, respectively.

Chapter 3. **Interlaminar fracture toughness of hybrid carbon nanotubes/ZnO nanorods grafted carbon fiber reinforced polymer composites**

3.1 Overview

In this study, carbon fibers underwent two different nano-reinforcements synthesis techniques to make hierarchical reinforcements; (a) graphitic structure by design (GSD) method was used to grow multi-walled carbon nanotubes (CNTs), and (b) hydrothermal technique was employed to grow zinc oxide (ZnO) nanorods over the carbon fibers. The carbon fibers with surface grown ZnO nanorods or CNTs were utilized to fabricate hybrid carbon fiber reinforced polymer composites (CFRPs). Double cantilever beam (DCB) tests were performed to investigate the effect of the surface grown nano-reinforcements on the Mode I interlaminar fracture toughness (G_{Ic}) of the hybrid CFRPs. The surface grown CNTs enhanced the G_{Ic} of the CFRPs by 22% and 32%, via uniform and checkerboard-patterned growth morphologies, respectively, over the carbon fiber fabrics. Strong attachment of the surface grown nano-reinforcements to the surface of the carbon fibers is crucial for improving the fracture toughness. Weak adhesion between the ZnO nanorods forests and the carbon fiber substrates yielded 37% drop in G_{Ic} of the CFRPs.

3.2 Introduction

Fiber reinforced polymer composites (FRPs) are structural materials with broad applications in aerospace, automotive, sport goods, etc. due to their high stiffness and strength to weight ratios [1,2]. Although FRPs possess excellent in-plane mechanical performance, they lack sufficient strength and stiffness along the out-of-plane direction. Particularly, in the interlaminar region,

conventional multilayered FRP laminates are insubstantial. Therefore, their resistance to delamination damage is a fundamental challenge in the FRPs application [85]. The delamination damage resistance in the FRPs can be evaluated by interlaminar fracture toughness in different modes: Mode I – crack opening mode where the delaminated faces open away from each other, Mode II – in-plane shear mode where a delamination grows due to an in-plane shear force or displacement perpendicular to the crack front, and Mode III: out-of-plane shear mode where the delamination grows due to an out-of-plane shear force or displacement parallel to the crack front.

Several remedies have been carried out to enhance the FRPs' poor interlaminar fracture resistance, e.g. stitching [6], interleaving with toughened polymer [4,8], fiber surface treatment [7], etc. However, these methods usually deteriorate the in-plane mechanical performance of the FRPs [4,85]. Alternatively, utilizing nano-sized reinforcing materials in the FRPs' structure is a promising method to improve the out-of-plane performance of the FRPs avoiding the deteriorating effects of the abovementioned methods on their in-plane properties. Carbon nanotubes (CNTs) [4,9], graphene nano-platelets (GNPs) [79-81], nano-sized ceramic nanowires (e.g. ZnO [39,41], SiO_2 [82-85]), etc. are among the nano-fillers utilized to improve the mechanical performance of the hybrid FRPs.

The conventional approach to integrate the nano-fillers into the FRPs' structure is via mixing the fillers into the matrix phase prior to fabricating the composite laminates [9]. This method simply modifies the matrix material by adding nano-additives. Although some improvements in the matrix dominated properties were achieved [9,86], utilizing high volume ratios of nano-fillers can be severely limited by the difficulty of dispersing them into polymeric matrices [15]. For example, the inherent tendency of CNTs to agglomerate limits their achievable mixing weight percent to less than 3.0 wt.% [22,87]. The CNT agglomerates disprove the mechanical

performance of the host matrix, as they provide possible stress concentration locations inside the host material. In addition, mixing a minute weight percentage of CNTs into a polymeric matrix dramatically increases the polymer's viscosity, thus, preventing the matrix from defusing in-between the fibers during the composite fabrication process [9].

Alternatively, in order to avoid the dispersion problems associated with the mixing methods, nanostructures can be grown over the surface of the reinforcement fibers. This approach produces hybrid hierarchical reinforcements, potentially capable of providing the composites with a stronger fiber/matrix interface. However, some growth methods could be destructive to the fibers, resulting in poor in-plane mechanical performance of the hybrid FRPs. For example, chemical vapor deposition (CVD) is the most common approach to grow CNTs, which requires relatively high temperatures (700-1100 °C). Although great improvements in the interlaminar fracture toughness of the CVD-CNT grown hybrid FRPs have been reported in the literature [26,87,96], this temperature range induce destructive effects on the in-plane mechanical performance of the FRPs; both glass and carbon fibers are sensitive to these elevated temperatures [19,22]. An alternative method to CVD, graphitic structures by design (GSD), which utilizes relatively low temperatures (550 °C) [27,28], has been reported to improve in-plane and out-of-plane mechanical performance of carbon fiber reinforced polymer composites (CFRPs) [22,29,30]. The simplicity of the equipment and nontoxicity of the gases utilized in the GSD technique are among the advantages of this method over the CVD. In addition, the GSD technique enables the growth of CNT frosts in various patterns and topologies over the fibers, as CNTs would grow where the catalyst metal is pre-deposited. This capability was used previously [29,30] to promote the benefits of the CNT growth simultaneously for both the in-plane and the

out-of-plane performance of the CFRPs. However, GSD still moderately induces damage to the in-plane mechanical performance of FRPs based on glass fibers (GFRPs) [88].

Similar to CNTs, ZnO nanorods can be grown over structural fibers to produce hybrid reinforcements [31,32]. In addition to the mechanical benefits, ZnO is a semi-conductive and piezoelectric material. These unique characteristics of ZnO facilitate their application in energy harvesting and structural health monitoring of the hybrid FRPs [46,89,90]. There are several techniques to synthesize ZnO nanorods; vapor-phase transport [33], metalorganic chemical vapor deposition [34], sputtering [35], molecular beam epitaxy [36], thermal evaporation [37] and vapor-liquid-solid [38,91]. Most of these methods employ elevated temperatures, which are destructive to carbon fibers, and require complex synthesis setup. Alternatively, hydrothermal synthesis is a low temperature (~90 °C) solution-based technique, capable of successfully growing ZnO nanorods over carbon fibers [31,32]. Employing this technique yielded improvements in fiber/matrix interface shear strength [32], interlaminar shear strength [41], vibrations attenuation [39,41], in-plane on-axis and off-axis tensile strengths [41,92], creep behavior [40] and high-velocity impact energy dissipation [92] of CFRPs.

In the present work the GSD and the hydrothermal synthesis techniques were employed to grow multiwalled CNTs (MWCNTs) and ZnO nanorods, separately, over woven carbon fiber fabrics. In order to unravel the effect of different parameters included in the nano-reinforcement growth techniques (exposure to the GSD temperature, uniform or patterned CNT growth topologies, exposure to hydrothermal environment, and ZnO nanorods growth), carbon fibers underwent various surface treatments. Field emission scanning electron microscopy (FE-SEM) was utilized to examine the quality of the grown nano-reinforcements. Composites based on these hybrid fibers were fabricated. Double cantilever beam (DCB) tests were performed to investigate the

effect of the surface grown nano-reinforcements on the Mode I interlaminar fracture toughness of the hybrid CFRPs. Fractographs, produced using the FE-SEM, of the fracture surfaces of the CFRPs with different configurations in the interlaminar region, were used to investigate the interlaminar fracture mechanisms and the role of surface grown nano-reinforcements to resist against these mechanisms.

3.3 Materials and experimental methods

3.3.1 Preparing the fibers for nano-reinforcement synthesis procedures

Un-sized plain-woven SGP196 (IM7-GP, provided by Hexcel Inc.) carbon fiber fabric (6 K filaments count in a tow) was used as the main reinforcements. Square samples of 130 × 130 mm^2 were cut from the fiber fabrics along the warp and weft directions to perform the desired surface treatments.

The GSD MWCNTs synthesis technique requires pre-deposition of a catalyst meal (i.e. nickel in this study) on the surface of the carbon fibers. The CNTs growth initiate at the areas where the catalyst material is pre-deposited. For growing uniform CNTs forests over the carbon fiber fabrics, a uniform layer of nickel was deposited. An ATC Orion (AJA international Inc.) high vacuum sputtering system was utilized to deposit a 2 nm thick layer of nickel on both sides of the square carbon fabric samples under 3 mTorr pressure of argon gas where 200 W of power was supplied to the sputtering target. To achieve a checkerboard patterned CNTs forest over the carbon fiber fabrics, a perforated mesh template with a thread size of 76 μm and an opening edge size of 140 μm, was clamped on the fabrics prior to depositing the nickel layer.

Hydrothermal ZnO nanorods synthesis technique requires a pre-deposited ZnO seed layer over the carbon fibers to initiate the growth of ZnO nanowires. The same magnetron sputtering

system used in the aforementioned nickel sputtering was utilized here, supplied by 140 W of power, to deposit a 75 nm thick layer of amorphous ZnO on both sides of the square carbon fiber fabric samples.

3.3.2 MWCNTs synthesis by GSD technique

The MWCNTs growth process was performed following the GSD protocol explained elsewhere [27,28]. Particularly, the GSDCNT growth process was carried out inside a quartz tube reactor equipped with a thermal controller and three-input gas mass flow controllers. Briefly, the GSD process starts with a reduction step, under an H_2/N_2 gas mixture atmosphere at 550 °C for 2hr. Then, the process is followed by the flushing step in which the tube reactor is flushed with N_2 gas to get rid of any residuals of the previous step. Subsequently, the CNTs growth step begins, maintaining the constant temperature at 550 °C for 1hr under a $C_2H_4/H_2/N_2$ environment. In order to unravel the effect of GSD heat treatment and gas environment on the carbon fibers, some samples with no pre-deposited nickel layer were exposed to identical heat-treatment and gas mixtures as in the GSD process. Consequently, they didn't possess any radially grown MWCNTs on their surfaces.

3.3.3 ZnO nanorods synthesis by hydrothermal technique

To grow ZnO nanorods over the carbon fiber fabrics, a hydrothermal ZnO synthesis technique was performed which is explained in more details elsewhere [39]. As explained earlier, prior to conduct the hydrothermal synthesis, a 75 nm thick layer of amorphous ZnO was deposited on both sides of the de-sized fabrics. This pre-sputtered ZnO layer provides initiation seeds for the hydrothermally growing ZnO nanorod crystals on the surface of the carbon fibers. The synthesis technique utilizes an aqueous solution of zinc acetate dihydrate ($Zn(O_2CCH_3)_2.2H_2O$) and hexamethylenetetramine (HMTA) in deionized (DI) water using 30 mM concentrations of each

chemical. In order to grow the ZnO nanorods, the pro-coated samples were immersed in the abovementioned solution and kept in a convection oven at 85 °C for 8 hours. To unravel the effects of exposing the fabrics to the hydrothermal environment, some ZnO pre-coated samples were soaked in DI water and heated up to 85 °C for 8 hours. After completion of the synthesis process, the fibers were rinsed using DI water and dried overnight in the same oven at 85 °C.

3.3.4 Sample configurations and composite laminates fabrication

In order to examine the quality of the grown nano-structures, over the carbon fibers, a 5200 Hitachi FE-SEM electron microscope operating at 5 kV was used. To illustrate of MWCNTs forest patches grown in a checkerboard pattern, the GSD synthesis technique was carried out on a flat surface of a silicon wafer substrate, sputtered with a patterned nickel catalyst layer, and SEM was performed on this sample.

After all the different surface treatments on the carbon fibers, six distinctive sample configurations were achieved, which their designation and the process they underwent are listed in Table 3-1.

Table 3-1. Different designed sample configurations

Label	***Treatment undergone***	**Nano-reinforcements grown**
R	*As-received carbon fiber fabric (reference)*	none
H	*Reference, exposed to the heat treatment and gas environment of GSD method*	none
UG	*Reference, pre-coated with a uniform nickel layer, MWCNT growth by GSD method*	Uniform MWCNTs forest
PG	*Reference, pre-coated with a patterned nickel layer, MWCNT growth by GSD method*	Patterned MWCNTs forest
W	*Reference, pre-coated with uniform ZnO layer, exposed to hot water*	none
Z	*Reference, pre-coated with uniform ZnO layer, hydrothermal ZnO nanorods growth*	ZnO nanorods

The composite fabrication was carried out utilizing a vacuum- and pressure-assisted hand layup system. Aeropoxy™ (PTM&W Industries Inc.) that comprises a resin (PR2032), and a hardener (PH3665) was used as the matrix to fabricate the different hybrid CFRPs. The composite laminates comprised a total of 10 layers: 4 layers of as-received carbon fiber fabrics, 2 layers of surface treated fabrics (i.e. listed in Table 3-1), and another 4 layers of as-received carbon fiber fabrics. The composite panels were labeled after their two middle layers' designations. In order to impose interlaminar pre-cracks in the composite panels, as advised by the ASTM standard [97], a PTFE (Teflon) sheet was inserted between the two middle layers halfway through their length. Figure 3-1 shows a schematic of the laminate stacking sequence for the fabrication process.

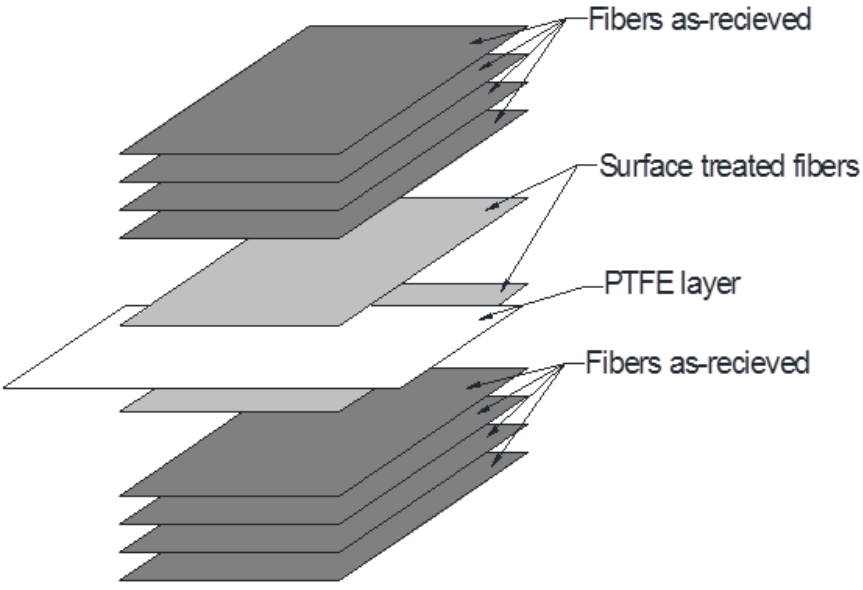

Figure 3-1. Schematic of the laminates stacking sequence

The mold used in the layup fabrication system had the capacity of fabricating maximum four composite panels at a time, providing a consistent fiber volume fraction for all the four laminates. Therefore, two separate layup sets were fabricated; the first set included the laminates based on R, H, UG, and PG configurations, and the second included the laminates based on R, W, and Z configurations. The weights of the samples were measured before and after the composite fabrication to calculate the fiber volume fractions of the composite laminates. Table 3-2 lists the fiber volume fractions of different composite laminates. The composite laminates fabricated as the first set possessed a fiber volume fraction of 50.85±1.05%, and the laminates of the second set 58.03±1.23%.

Table 3-2. Fiber volume fractions of composite laminates

CFRP label	R1	H	UG	PG	R2	W	Z
V^f (%)	50.7	51.9	50.0	50.8	58.8	58.5	56.8

Following the ASTM D5528 – 13 standard [97], DCB specimens of 130.0×25.4 mm^2 were cut out of the fabricated laminates perpendicular to the PTFE insert. Piano hinges were attached on both sides of the specimens. In order to ensure frictionless performance of the piano hinges, prior to attaching the hinges to the samples, G-10 tabs were glued on the both sides of the specimens tips and then the hinges were glued to the tabs. The same epoxy system used in the composite fabrication was utilized for attaching the tabs and hinges to the DCB specimens. As suggested by the ASTM standard, both lateral faces of the specimen were painted by a correction fluid (WiteOut) in order to ease the crack tip detection during the experiments. Also, tick marks 1mm

apart were marked on the painted faces. Figure 3-2 shows a schematic of the prepared DCB specimens.

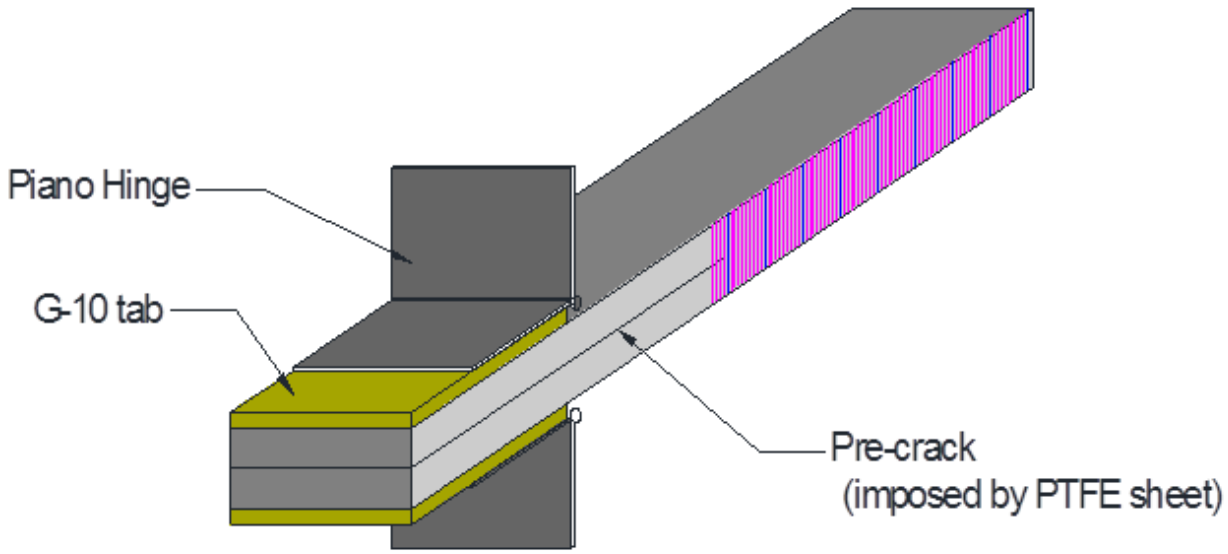

Figure 3-2. Schematic of the specimens prepared for double cantilever beam (DCB) tests.

3.3.5 Double cantilever beam (DCB) experiments

The prepared composite samples were tested according to ASTM D5528 – 13 standard [97]; the standard test method for Mode I interlaminar fracture toughness of unidirectional fiber-reinforced polymer matrix composites which can also be used for woven fabrics reinforced composites [97]. An Instron® 4400R testing frame equipped with a 1.0 kN capacity load-cell was used under 3.0 mm/min constant crosshead speed to perform the DCB tests. The cross-head displacement and the load were recorded using a data acquisition system hooked up with the

testing frame. An optical zoom microscope was also utilized to produce a magnified view of the crack tip for accurately tracking the interlaminar crack growth. The test setup is shown in Figure 3-3. As required by the ASTM standard, the interlaminar crack lengths were read and recorded by the test operator as a function of cross-head displacement.

Figure 3-3. The test setup for interlaminar fracture toughness experiments.

Suggested by the standard, modified beam theory (MBT) method was utilized for Mode I interlaminar fracture toughness calculations as in equation (3.1)

$$G_{Ic} = \frac{3P\delta}{2b(a + |\Delta|)} \tag{3.1}$$

where G_{Ic} is the opening Mode I interlaminar fracture toughness, P is applied load, δ is load point deflection, b is width of DCB specimen, a is delamination length, and Δ is effective delamination extension to correct for rotation of DCB arms at the delamination front. The Δ

value can be determined experimentally, by plotting the cube root of compliance values, which are $(\delta/P)^{(1/3)}$, versus delamination length, a, and fitting a linear trend-line. The distance between the origin and the point where the line intersects the a-axis would be Δ [97].

The calculated Mode I interlaminar fracture toughness values were corrected for large displacements, where the correction factor F is calculated by equation (3.2) as follows [97],

$$F = 1 - \frac{3}{10}\left(\frac{\delta}{a}\right)^2 - \frac{3}{2}\left(\frac{\delta t}{a^2}\right) \tag{3.2}$$

where t is the perpendicular distance between the center line of the hinge's pin and the top surface of the DCB specimen plus one quarter of the DCB specimen's thickness. The factor F multiplied by the calculated interlaminar fracture toughness values calculated in equation (3.1) gives the corrected value for G_{Ic}.

Visual observation (VIS) criteria was considered for the initiation value for G_{Ic}, where this value is corresponding to the load and displacement value recorded for the first point as delamination crack is visually observed to start growing from the insert. The G_{Ic} for delamination front growth were also calculated to produce delamination resistance curves (so-called *R*-Curves) for different composite configurations.

3.4 Results and discussion

3.4.1 Scanning electron microscopy of the synthesized nano-reinforcements

The MWCNTs grown over the carbon fibers utilizing the GSD method are shown in micrographs of Figure 3-4(a). The inset picture is a magnified micrograph of the grown MWCNTs showing that the MWCNTs have ~20 nm diameters and wavy shapes. Figure 3-4 (b) shows the

checkerboard pattern growth of CNT patches over a silicon wafer. The same pattern was used in preparing the PG sample configuration.

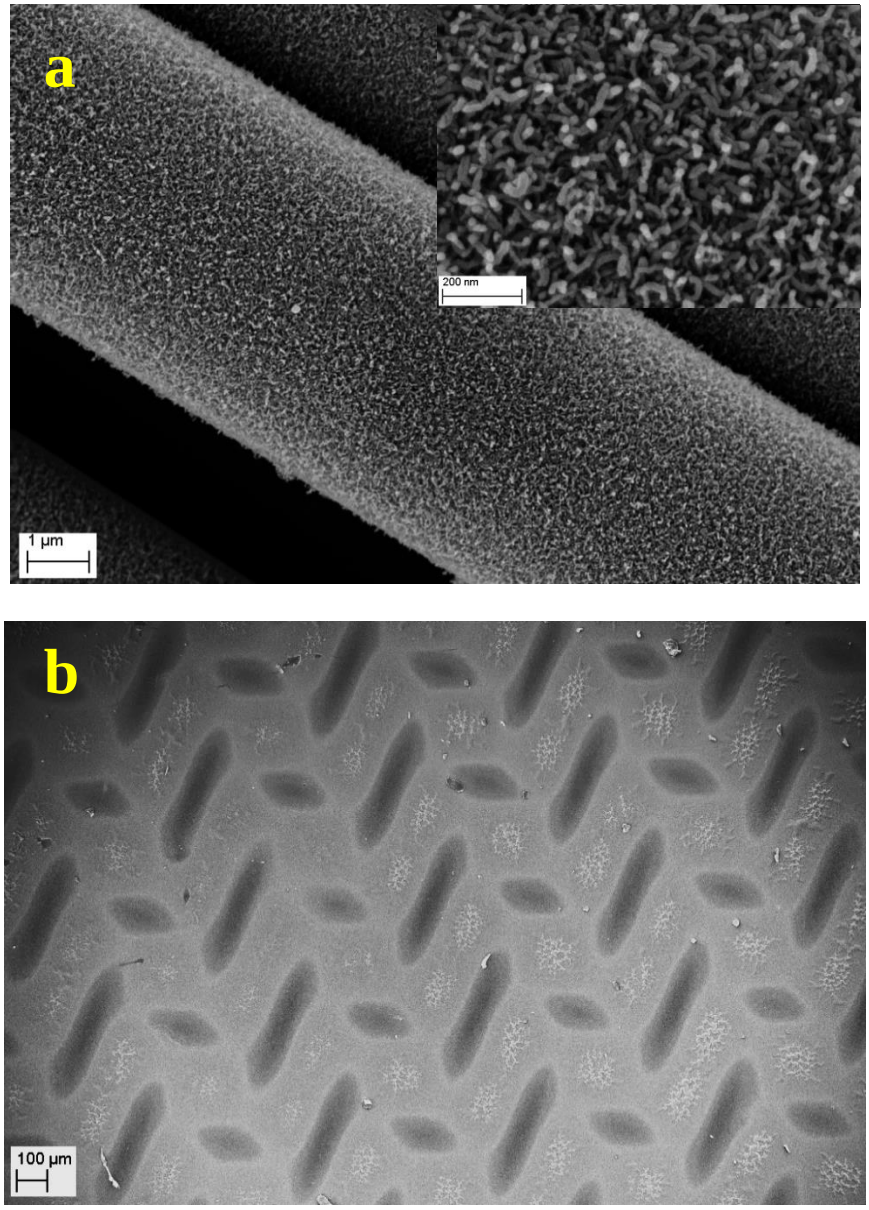

Figure 3-4. Scanning electron microscopy (SEM) micrographs of (a) GSD grown MWCNTs over carbon fibers in two different magnifications, and (b) MWCNT patches grown in a checkerboard pattern over a silicon wafer. Shining spots are MWCNT patches.

The hydrothermally ZnO nanorods grown over the carbon fibers are shown in micrographs of Figure 3-5. The magnified inset micrograph in Figure 3-5(a), as well as Figure 3-5(b) show the nanorods possess ~2.0 μm length and ~20.0-100.0 nm diameter.

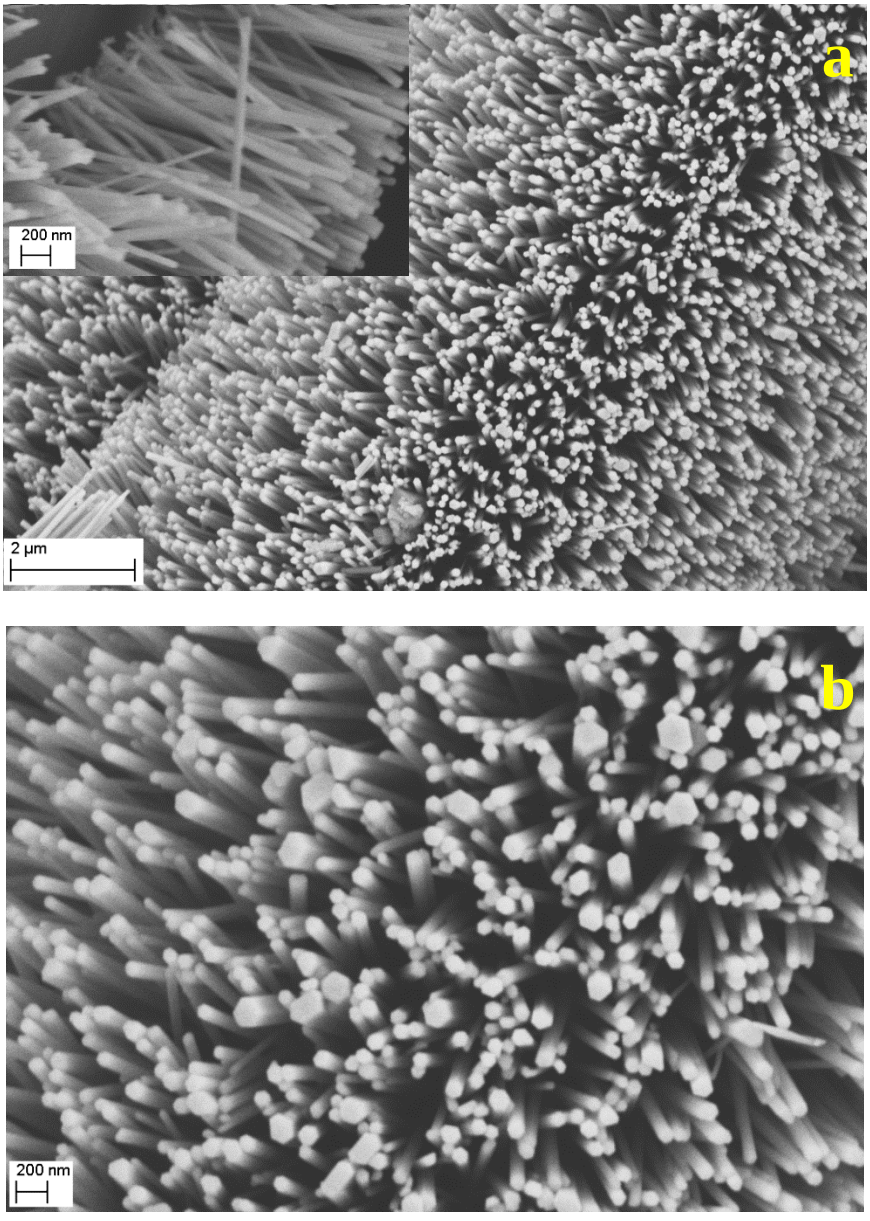

Figure 3-5. Scanning electron microscopy (SEM) micrographs of ZnO nanorods grown over carbon fibers using hydrothermal synthesis technique, (a) the overall growth over a carbon fiber, the insert is higher magnification to estimate the nanorods' lengths, and (b) a magnified view to estimate the nanorods' diameters

3.4.2 The effect of GSD grown MWCNTs on Mode I interlaminar fracture toughness of hybrid CFRPs

Figure 3-6 shows representative load vs. displacement curves for the DCB tests on the CFRPs based on R (reference), H (GSD heat-treated), UG (uniform GSD grown MWCNTs) and PG (patterned GSD grown MWCNTs) fibers. Inferred from Figure 3-6, all the samples exhibited initial a linear-elastic behavior up to the point where the first visual delamination crack growth occurred. A mutual characteristic for all the curves is the presence of several sudden drops in the load as the delamination crack propagates. This behavior is expected in woven fiber reinforced polymer composites [98-100] where the delamination crack growth is unstable for this type of composites. In the case of a stable crack growth behavior, the load gradually drops as the cross-head displacement increases [97].

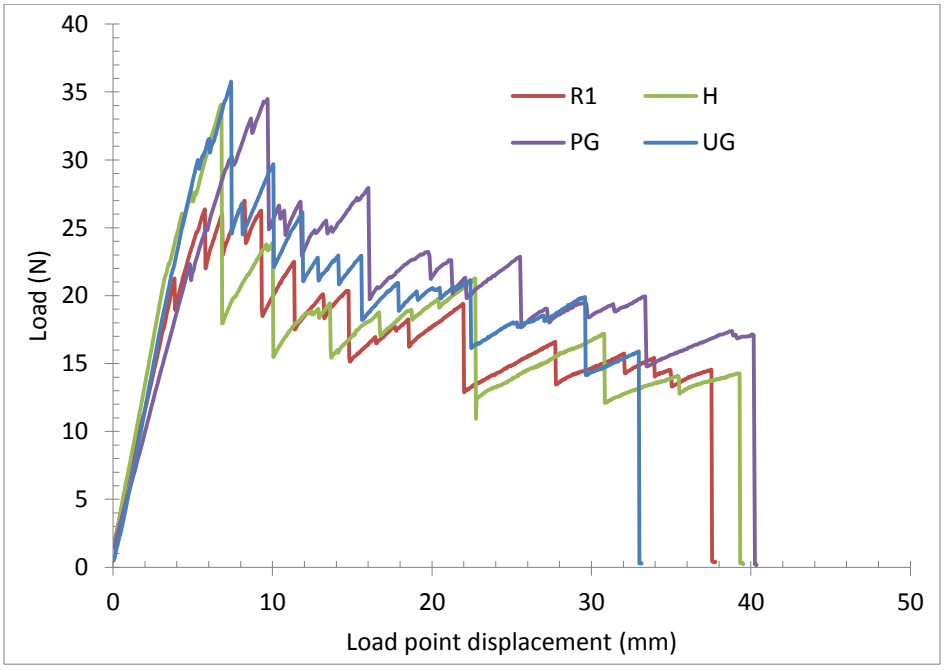

Figure 3-6. Representative load vs. load-point displacement curves for the designed hybrid CFRPs based on reference (R), heat-treated (H), patterned GSD grown MWCNTs (PG), and uniform GSD grown MWCNTs (UG) fibers.

Delamination crack growth behaviors of the designed CFRPs are shown in Figure 3-7 where the delamination crack lengths vs. load-point displacement data are plotted in (a), and delamination crack lengths vs. load are plotted in (b).

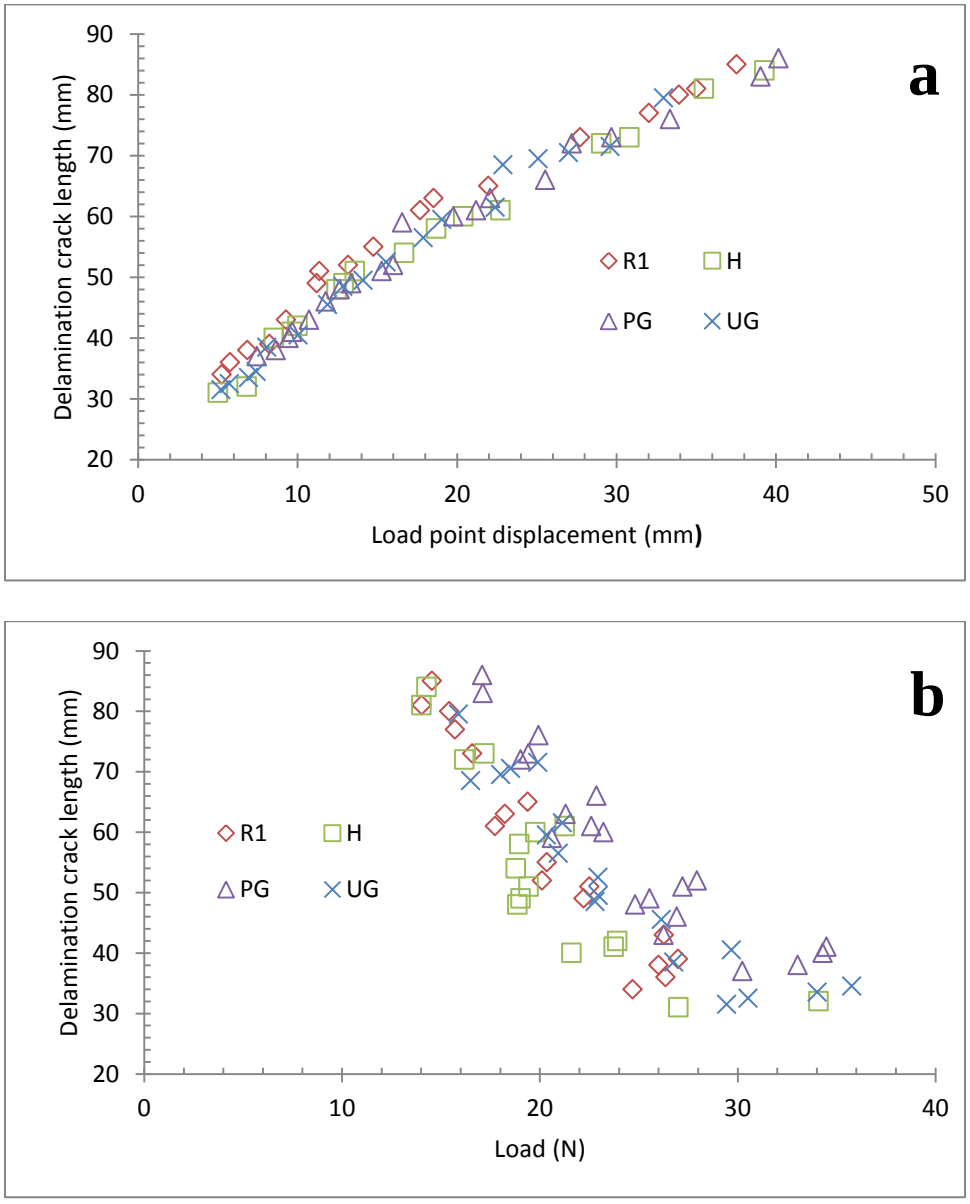

Figure 3-7. Representative delamination crack length vs. (a) load-point displacement, and (b) vs. load data for the CFRPs based on reference (R), heat-treated (H), patterned GSD grown MWCNTs (PG), and uniform GSD grown MWCNTs (UG) fibers.

The composites comprising surface grown MWCNTs (UG and PG) entailed higher loads to propagate the delamination cracks compared to the samples with no MWCNTs (R and H). This can be observed in the behavior of UG and PG samples illustrated in Figure 3-7(b) where for the same crack lengths, the PG configuration attained the highest load values among all the configurations followed by the UG configuration. Therefore, even before post-processing the results, it was anticipated to observe higher Mode I interlaminar fracture toughness values for the samples reinforced with surface grown MWCNTs (i.e. the UG and PG configurations), in lieu to the samples with no MWCNTs (i.e. R1 and H configurations). Representative crack resistance curves (R-curves) for the aforementioned sample configurations are plotted in Figure 3-8 and as mentioned before, PG and UG configurations exhibited highest G_{Ic} values.

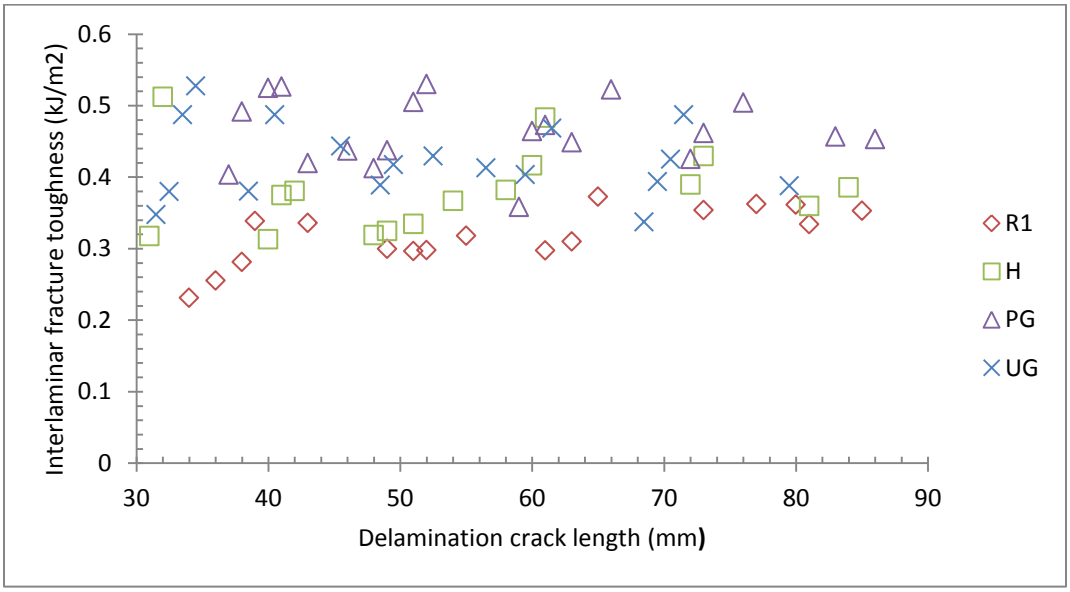

Figure 3-8. Representative R-curves for the designed hybrid CFRPs based on reference (R), heat-treated (H), patterned GSD grown MWCNTs (PG), and uniform GSD grown MWCNTs (UG) fibers.

For unidirectional composite laminates, it was reported that the R-curve starts at a minimum value, which is G_{Ic} for crack initiation, and as the delamination crack grows, G_{Ic} value gradually

increases to form a plateau shape representing G_{Ic} for crack growth [97]. Fiber bridging phenomenon between the two delaminating plies is responsible for the increase in toughness and subsequently increase in G_{Ic} as the crack grows. This phenomenon was observed during the DCB tests of the current study (shown in Figure 3-9) and, therefore, similar behavior was observed in the R-curves plotted in Figure 3-8.

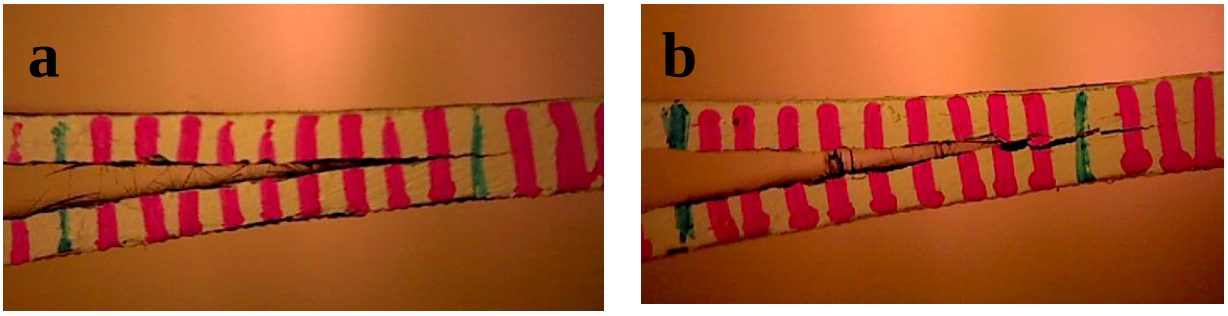

Figure 3-9. Crack opening and fiber bridging for the DCB samples based on (a) uniform GSD grown MWCNTs (i.e. UG), and (b) patterned GSD grown MWCNTs (i.e. PG) fibers.

Fibers' bridging and breakages are two energy dissipating mechanisms during the interlaminar crack growth. Furthermore, matrix cracking through the matrix-enriched regions, as well as matrix micro-cracking between adjacent fibers and in fiber/matrix interfaces are other key energy dissipating mechanisms that determine the critical energy release rates during the interlaminar crack growth. All the aforementioned damage mechanisms can be seen in the SEM micrographs of Figure 3-10 produced at the interlaminar fracture face of a DCB sample based on R fibers.

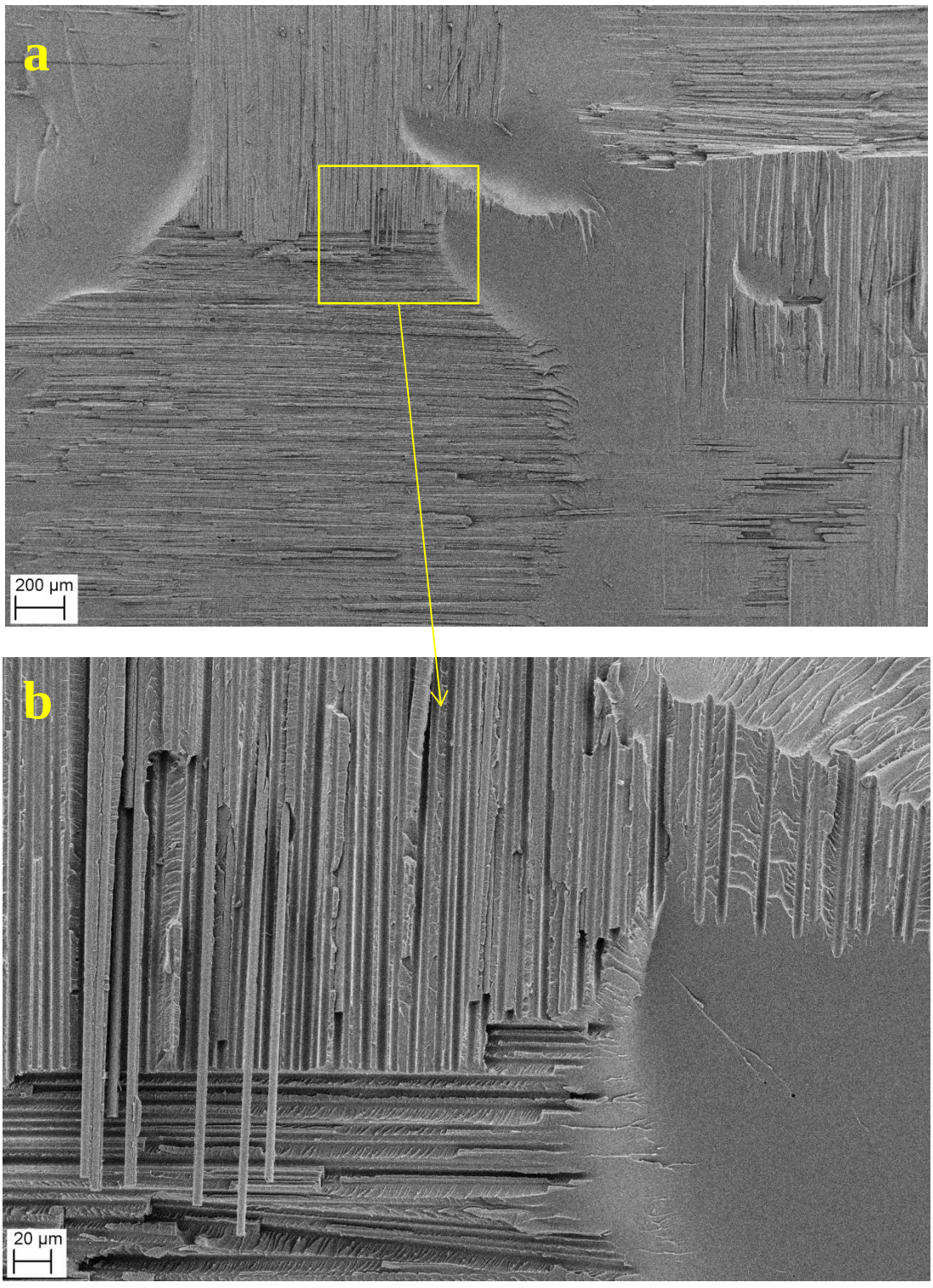

Figure 3-10. SEM micrographs of the interlaminar fracture face of a CFRP based on reference (i.e. R) fibers in two different magnifications.

Figure 3-10(a) shows the overall image of a fractured face, while Figure 3-10(b) shows a magnified region illustrating all the aforementioned fracture mechanisms (i.e. fibers' pull-out and breakage, matrix cracking through matrix enriched regions, and matrix micro-cracking in the vicinity of the fibers).

The critical energy release rates (i.e. interlaminar fracture toughness, G_{Ic}) at the crack initiation, as well as during the crack propagation were calculated for all the samples. For each sample configuration, the G_{Ic} value at the crack initiation and the average value of the G_{Ic}'s during the crack growth, were taken as $G_{Ic\text{-}CI}$ and $G_{Ic\text{-}CG}$, respectively, for that specific configuration. The average values of $G_{Ic\text{-}CI}$ and $G_{Ic\text{-}CG}$ for different sample configurations are shown in Figure 3-11. The error bars for G_{Ic} of crack initiation is the standard deviation of the values for the four samples of same configuration, while the error bars for G_{Ic} of crack growth are the average value of the standard deviations of the G_{Ic}'s of individual samples during the crack growth.

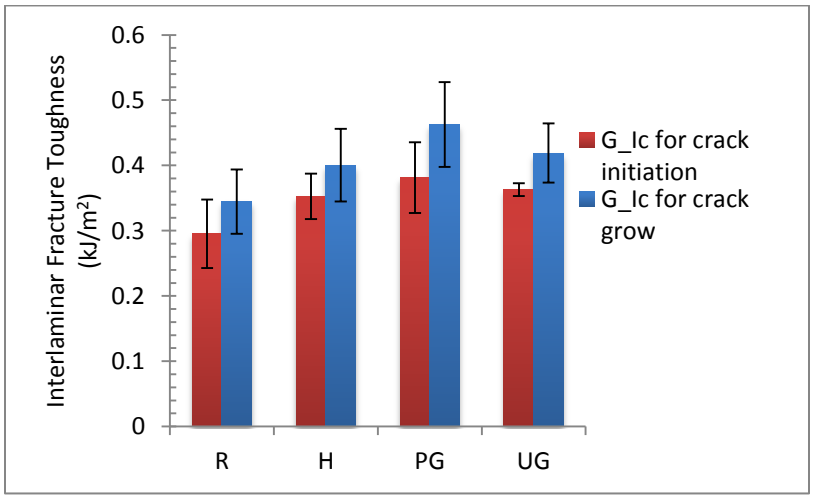

Figure 3-11. Interlaminar fracture toughness values for the designed hybrid CFRPs based on reference (R), heat-treated (H), patterned GSD grown MWCNTs (PG), and uniform GSD grown MWCNTs (UG) fibers.

Inferred from the results of Figure 3-11, the $G_{Ic\text{-}CI}$ and $G_{Ic\text{-}CG}$ of the CFRPs have been improved by 23% and 22% respectively, via uniform growing of MWCNTs over the carbon fibers. In other words, for a certain amount of interlaminar crack growth, the UG configuration released 22% more energy than the reference sample. This is evident by the SEM micrographs of Figure 3-12, which are taken for the interlaminar crack faces of the CFRPs based on R and UG fibers. The fracture surfaces of the hybrid CRRP based on the uniform CNT grown fibers, shown in Figure 3-12(a and c), possess finer wrinkles compared to the fracture surfaces of the reference CFRP, shown in Figure 3-12(b and d). The finer wrinkles on the fracture surface yielded larger accumulative fractured surface area, hence, more energy was dissipated when interlaminar crack propagated. This fine pattern of wrinkles on the fracture surface stems from the entanglement of the CNTs with the polymer matrix in the fiber/matrix interface. The magnified inset image inside Figure 3-12(c) shows a fractured fiber/matrix interface region. Some CNTs were pulled-out and some fractured. This figure reveals how the polymer matrix and the CNTs forest interacted with each other. The large aspect ratio of the CNTs provides large surface area to interact with the polymer matrix, dissipating more energy when they slid against each other. The above-mentioned damage mechanisms combined all together were responsible for the improvement in G_{Ic}.

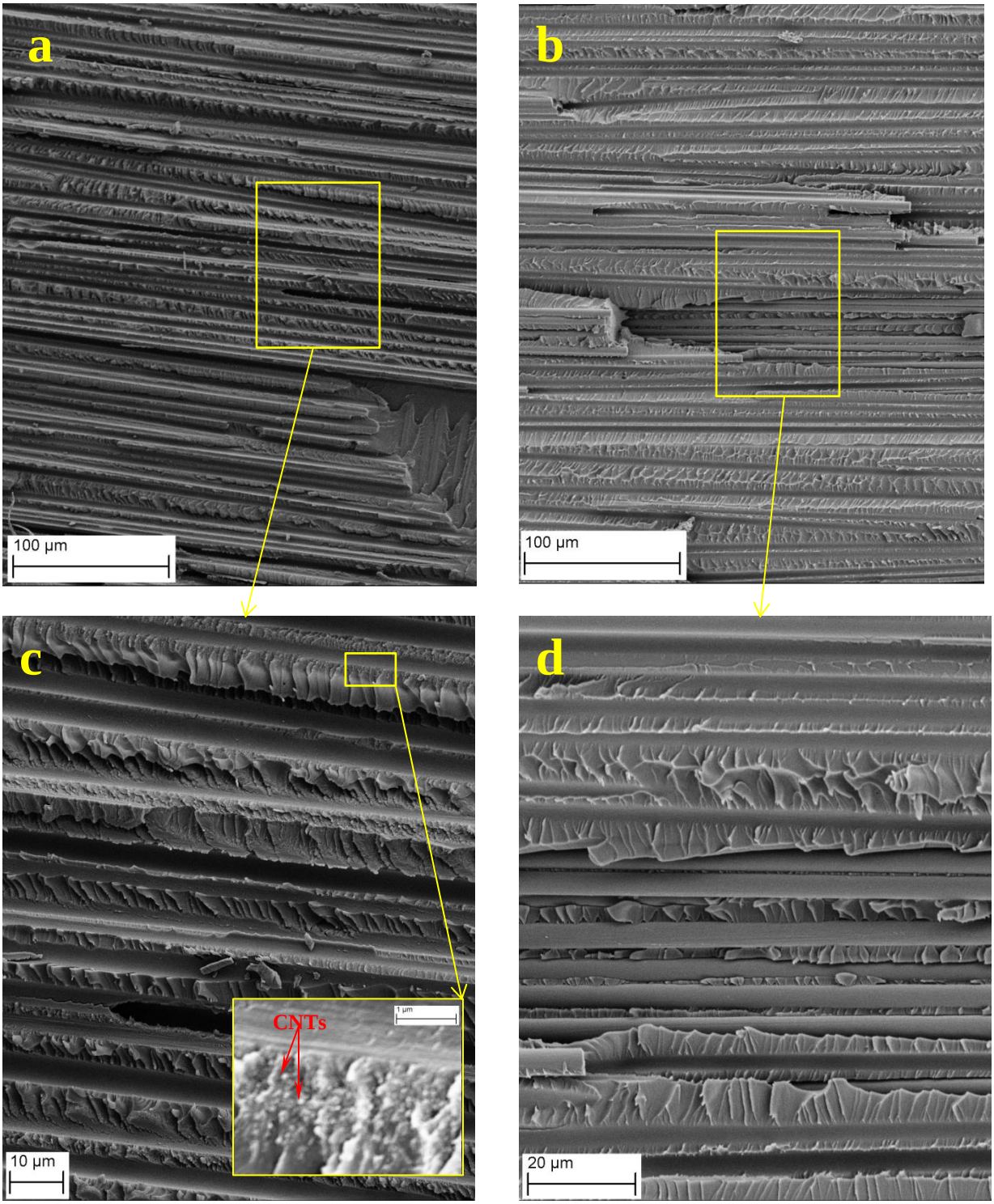

Figure 3-12. SEM micrographs of the interlaminar fracture faces of CFRP based on (a and c) uniform GSD grown MWCNTs (UG), and (b and d) reference (i.e. R) fibers.

The results of Figure 3-11 for the CFRPs based on GSD heat treated fibers (i.e. H) shows 16% improvement in crack growth interlaminar fracture toughness compared to the reference CFRPs. Stronger fiber/matrix adhesion due to a moderate oxidation of carbon fibers during the heat treatment can be the reason for this improvement. However, the maximum improvements in both crack initiation and crack growth G_{Ic} were observed in the hybrid CFRPs based on the carbon fibers surface-grown with a checkerboard pattern of MWCNTs forest of Figure 3-4(b), which is designated as PG configuration. Significant improvements of 29% and 34% in G_{Ic} of crack initiation and crack propagation, respectively, were achieved via growing this specific topology of CNTs forest over the carbon fiber fabrics. The PG configuration benefited from both the heat treatment and the surface grown CNTs characteristics. However, the mechanical interlocking of the polymer matrix in between the CNT patches over the carbon fibers in the interlaminar region can be the major cause for this significant improvement in interlaminar fracture toughness. This result is in agreement with our previously published results [30] where maximum impact energy dissipation was observed in this specific topology of MWCNTs growth using the GSD method.

3.4.3 The effect of ZnO nanorods growth on Mode I interlaminar toughness of hybrid CFRPs

Figure 3-13 shows representative load vs. displacement curves for the DCB specimens based on R (reference), W (hot-water exposed) and Z (ZnO nanorods grown) composite configurations. The initial linear-elastic behavior can be seen for these CFRPs in Figure 3-13. The curves deviate from the linearity as soon as first visual delamination cracks initiate. Similar to the CFRPs discussed in section 3.4.2, several sudden drops in load were observed as the delamination crack propagated exhibiting unstable crack growth behavior. However, these drops are less pronounced for the hybrid CFRPs based on ZnO nanorods grown fibers (i.e. Z). This behavior was noticed

during the experiments for this specific configuration, as the an almost stable crack growth was observed.

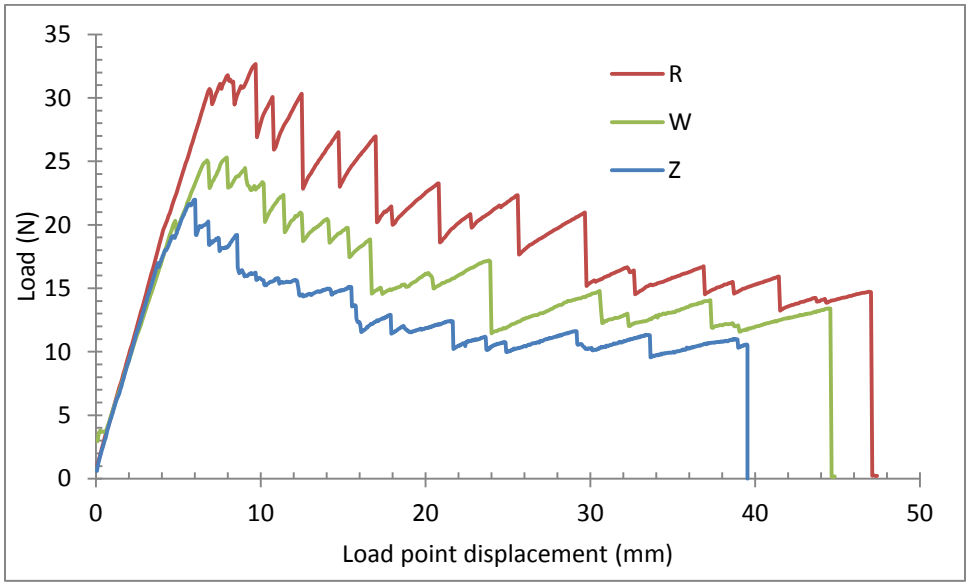

Figure 3-13. Representative load vs. load-point displacement curves for the designed hybrid CFRPs based on reference (R), hot-water exposed (W), ZnO nanorods grown (Z) fibers.

Delamination crack growth behaviors of the designed CFRPs are shown in Figure 3-14 Figure 3-7where delamination crack lengths vs. load-point displacement data are plotted in (a), and delamination crack lengths vs. load are plotted in (b). Figure 3-14 reveals that the interlaminar crack in the CFRPs with ZnO nanorods has grown quicker compared to the reference CFRP. Inferred from Figure 3-14(b) for a certain crack length, the Z sample configuration needs lower loads to propagate the crack compared to the R sample. Also, the CFRPs based on water exposed fibers needed a level of load between Z and R samples. Therefore, it was expected that G_{Ic} disproves via sputtering the ZnO layer, exposing to hydrothermal solution environment and growing ZnO nanorods over fibers.

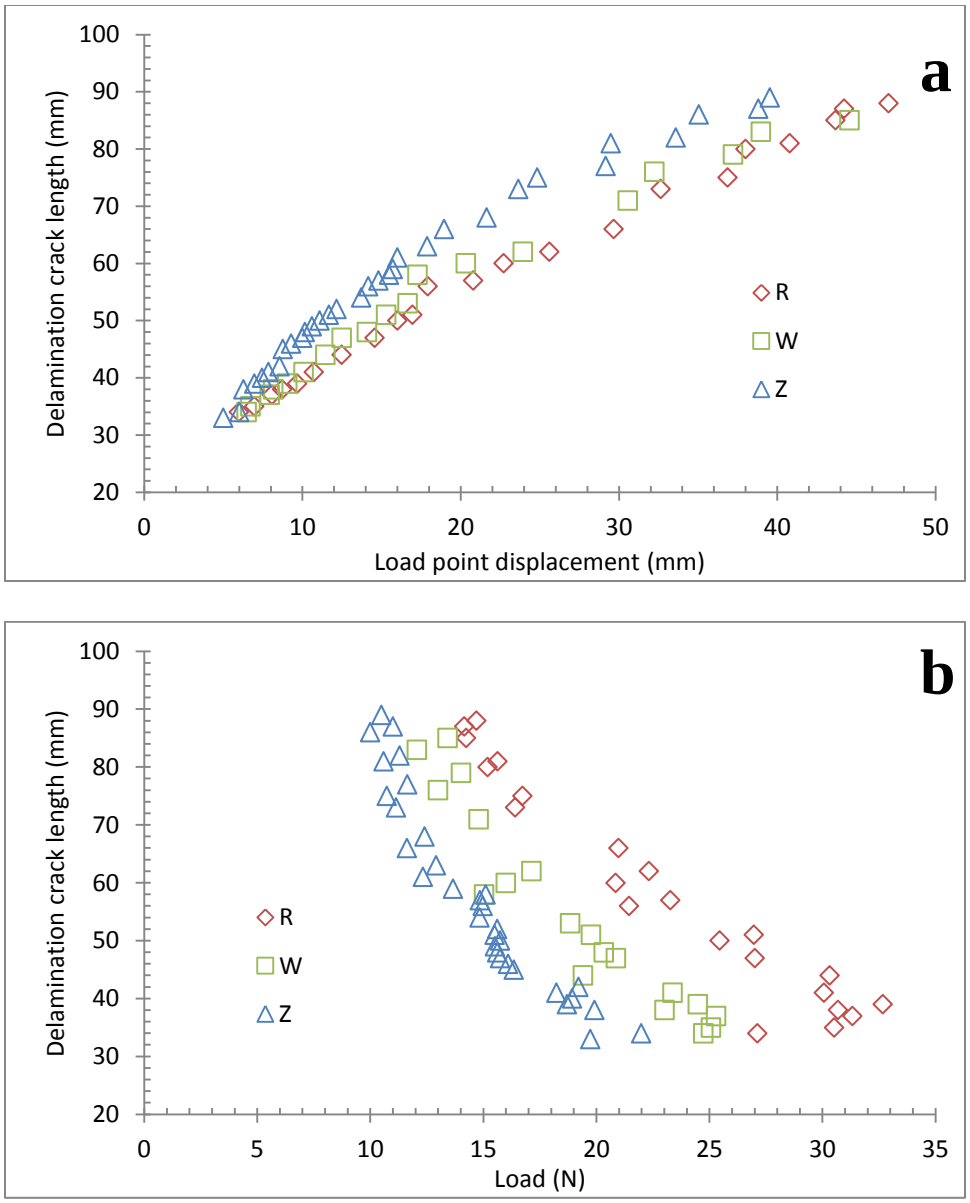

Figure 3-14. Representative delamination crack length vs. (a) load-point displacement, and (b) vs. load data for the designed hybrid CFRPs based on reference (R), hot-water exposed (W), ZnO nanorods grown (Z) fibers.

Representative crack resistance curves (R-curves) for these sample configurations are plotted in Figure 3-15 showing that the samples based on Z fibers possess lowest G_{Ic} values.

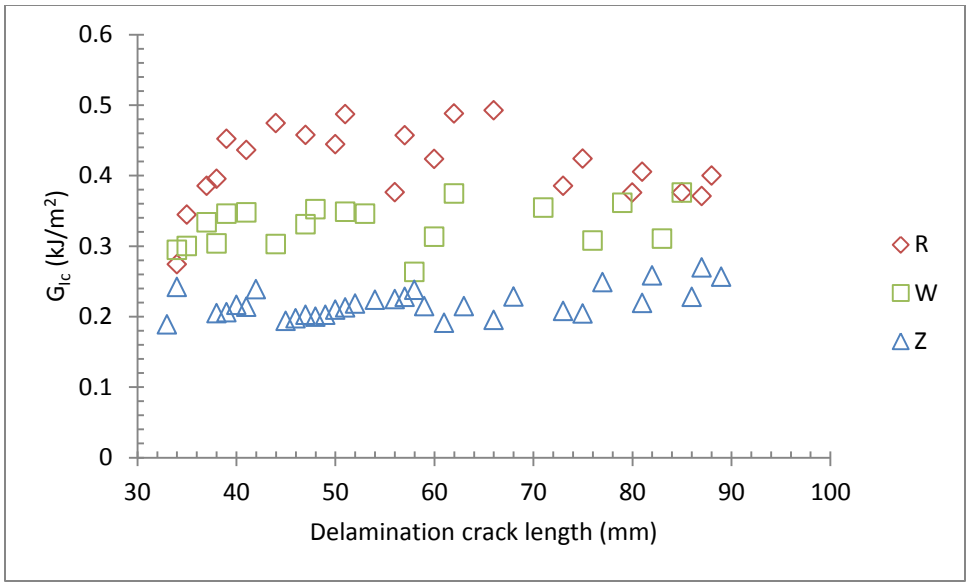

Figure 3-15. Representative R-curves for the designed hybrid CFRPs based on reference (R), hot-water exposed (W), ZnO nanorods grown (Z) fibers.

As delamination crack grew, the G_{Ic} values increased gradually from an initial value (i.e. $G_{Ic\text{-}CI}$) to form a plateau. This behavior was more pronounced in the reference CFRP and less in the CFRPs based on W fibers. However, in the CFRPs based on Z fibers, this trend was not observed. As discussed earlier, this gradually increase in G_{Ic} is owing to fiber bridging phenomenon which almost did not observed during the tests on the hybrid CFRPs based on Z fibers. Figure 3-16 shows the crack opening and fiber bridging phenomenon during the DCB tests of the samples based on reference and water exposed fibers. Fiber bridging was not observed during the DCB tests of the samples based on ZnO nanorods grown fibers.

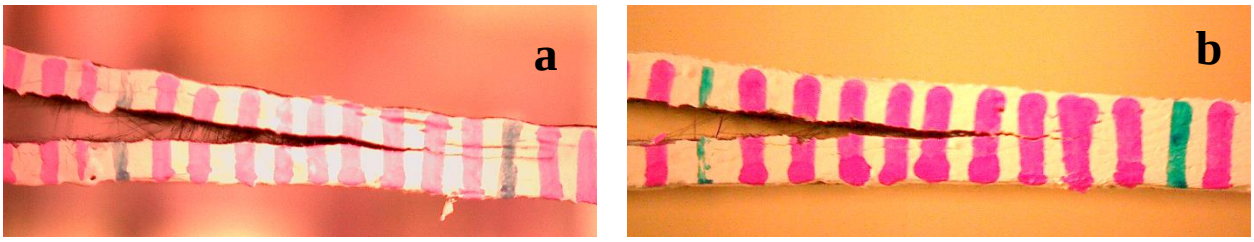

Figure 3-16. Crack opening and fiber bridging for the DCB samples based on (a) reference (i.e. R), and (b) hot-water exposed (i.e. W) fibers.

Based on the data acquired during the DCB tests, average values for $G_{Ic\text{-}CI}$ and $G_{Ic\text{-}CG}$ were achieved which are shown in Figure 3-17. The error bars for G_{Ic} of crack initiation is the standard deviation of the values for the four samples of same configuration, while the error bars for G_{Ic} of crack growth are the average value of the standard deviations of the G_{Ic}'s of individual samples during the crack growth.

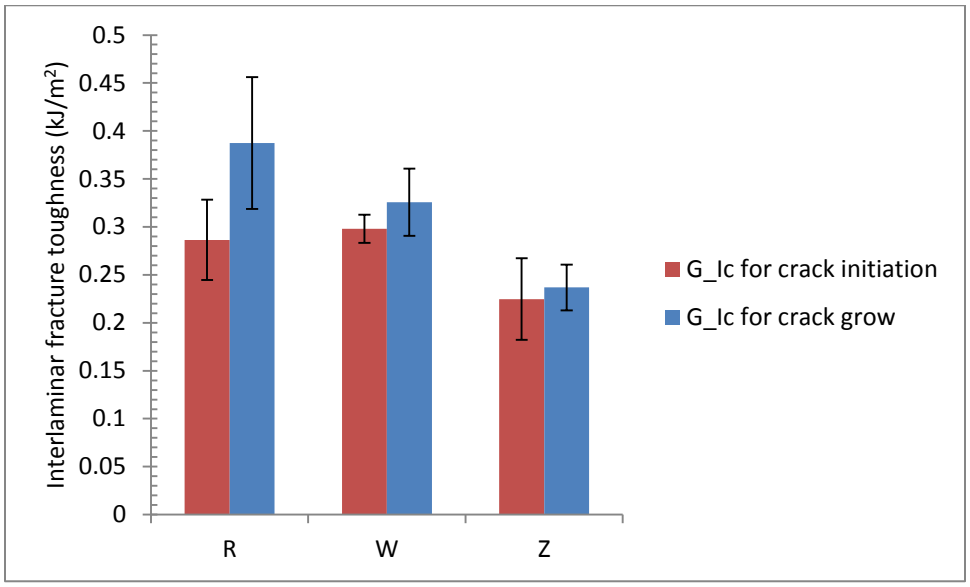

Figure 3-17. Interlaminar fracture toughness values for the designed hybrid CFRPs based on reference (R), hot-water exposed (W), ZnO nanorods grown (Z) fibers.

Inferred from Figure 3-17, Mode I interlaminar fracture toughness for crack growth decreased by 39% via growing ZnO nanorods over carbon fiber fabrics. The reason for this drop can be revealed by the SEM micrographs of Figure 3-18. The micrographs were taken at the opposite faces in the interlaminar region of a DCB sample based on the fibers comprising surface grown ZnO nanorods. From the SEM images of Figure 3-18 it appears that the interlaminar fracture has propagated between the ZnO nanorods forest of one lamina and their substrate fibers from the same lamina instead of between the ZnO nanorods frosts of the opposite laminae. As a result, the nanorods forest which initially belonged to the face shown in Figure 3-18(b and d) has been detached from the fibers surface and attached to the opposite face shown in Figure 3-18(a and c). Therefore, Figure 3-18(b and d) show bare faces of fibers and Figure 3-18(a and c) show ZnO nanorods forest from bottom. In other words, the interlaminar crack has not interacted with the nanorods and the matrix in the interlaminar region. This observation justifies the low fracture toughness of the hybrid CFRPs based on ZnO nanorods grown fibers compared to the reference CFRPs. This fracture pattern can be the reason that the fiber bridging was very limited for this sample configuration and therefore, the difference between G_{Ic} for crack initiation and crack propagation was negligible (results of Figure 3-17). The interlaminar fracture toughness in crack growth for the CFRPs based on the ZnO pre-sputtered and hot-water exposed fibers (i.e. W) was 16% less that the reference CFRPs (i.e. R). The reason could be a weak adhesion between the carbon fibers and the pre-sputtered amorphous ZnO layer. However, the interlaminar fracture toughness in crack initiation showed a slight improvement (4%).

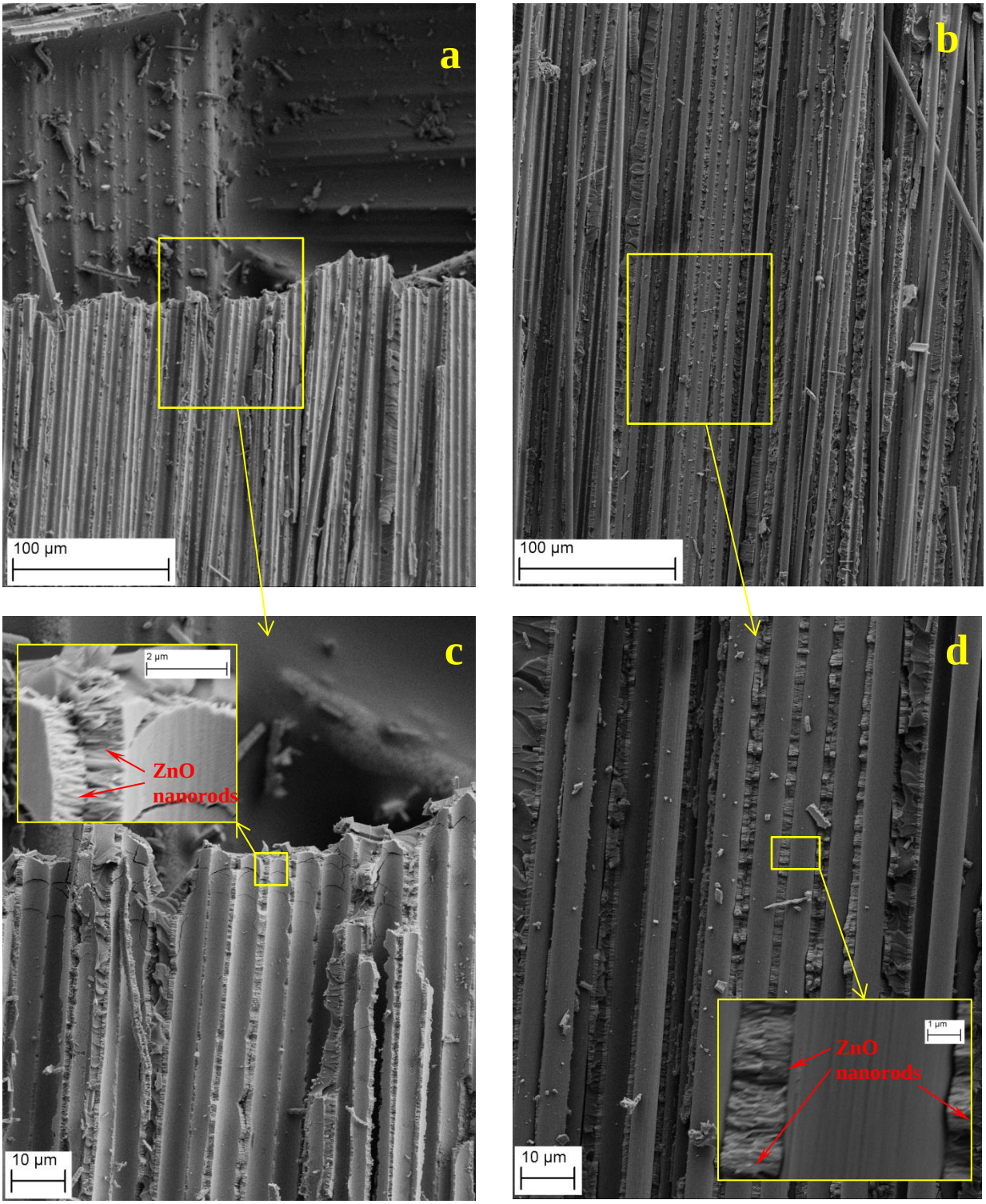

Figure 3-18. SEM micrographs of the interlaminar fracture faces of CFRP based on ZnO nanorods grown fibers. (a and c) are from one face, and (b and d) are from the opposite face.

3.5 Conclusions

Graphitic structure by design (GSD) technique was employed to grow MWCNTs over un-sized woven carbon fibers. Two different topologies of MWCNTs frosts were considered to grow: Uniform growth of CNTs forest and checkerboard patterned CNTs forest. To unravel the effects of exposure to GSD method environment, some as-received carbon fibers were exposed to the GSD temperature and the gas mixture, except they lacked the catalyst layer and therefore lacked MWCNTs growth at the end. A hydrothermal ZnO nanorods synthesis technique was utilized to grow ZnO nanorods over the carbon fibers. Again, some as-received carbon fibers were immersed in DI water as hot as the aquatic solution in the hydrothermal process, to untangle the effects of the process environment. Hybrid CFRPs based on differently surface-treated fibers were fabricated. Double cantilever beam (DCB) tests were performed following the ASTM standard for Mode I interlaminar fracture toughness (G_{Ic}) of fiber reinforced polymer composites. Outstanding improvements of 34% and 23% in G_{Ic} of the CFRPs were achieved via patterned and uniform growth of MWCNTs over carbon fibers. Fractographs taken by a scanning electron microscope (SEM) revealed that the mechanical interlocking of the polymers in-between the CNTs, CNTs pull-out and rupture, matrix/CNT frictional slip, and matrix micro-cracks at the fiber/matrix interface were the energy dissipating mechanisms yielding the improvements in G_{Ic}. On the other hand, dramatic drop in G_{Ic} (37%) was observed in the samples possessing surface grown ZnO nanorods. The fractographs revealed that the interlaminar crack propagated between the ZnO nanorods forests and their substrate carbon fibers, rather than propagating between the ZnO nanorods forests of opposing interlaminar faces.

Chapter 4. **Finite element analysis of interlaminar crack growth in hybrid carbon nanotubes/ZnO nanorods grafted carbon fiber reinforced polymer composites**

4.1 Overview

In the previous chapter, hybrid carbon fiber reinforced polymer composites (CFRPs), comprising either surface-grown carbon nanotubes (CNTs) or zin oxide (ZnO) nanorods, were designed and tested via double cantilever beam (DCB) tests to investigate the effects of the nano-reinforcements on the CFRPs' Mode I interlaminar fracture toughness. In this chapter, finite element method (FEM) was employed to simulate the interlaminar crack growth behavior of the hybrid CFRPs under Mode I crack opening loading conditions embodied by DCB tests. A commercial finite element software package, ABAQUS, was utilized to perform the numerical simulations. First, utilizing the virtual crack closure technique (VCCT), which is based on linear elastic fracture mechanics (LEFM) assumptions, preliminary FE models were developed to attain optimum mesh size and number of load increments. Then, VCCT-based FE models were developed for different samples configurations as tested in the experimental studies. Mode I interlaminar fracture toughness values utilized in these FE models were average values taken from the experimental measurements of the corresponding sample. In another set of simulations, cohesive elements were used to simulate the interlaminar crack propagation behavior of the hybrid CFRPs to study the effect of different surface treatments on the CFRPs' interlaminar strength against crack propagation, as well as their ultimate crack opening. These simulations revealed that the hybrid CFRP based on uniform MWCNs grown fiber exhibited 55% higher interlaminar strength compared to the reference CFRP based on raw fibers and via patterned

growth of MWCNTs, the ultimate crack opening of the CFRPs improved by 20%. As discussed in the previous chapter, due to the nature of woven CFRPs, unstable crack growth behavior was observed in the DCB experiments. In order to simulate such crack propagation behavior, the fluctuations in the interlaminar fracture toughness values along the crack length were taken into account and another VCCT-based set of simulations were performed. This method was successful in depicting the experimental mechanical behavior of the CFRPs obtained in the experiments.

4.2 Introduction

Fiber reinforced polymer composites (FRPs) are considered as a new generation of structural materials with broad applications in aerospace, automotive, sporting goods, etc. [1,2]. Despite their outstanding in-plane stiffness and strength to weight ratios, FRPs suffer from insufficient out-of-plane and interlaminar performance. Particularly in the interlaminar region, conventional multilayered FRP laminates are insubstantial. Therefore, their resistance against delamination damage is a fundamental challenge in several FRPs application [85,101]. The delamination damage resistance in the FRPs can be evaluated by interlaminar fracture toughness in different modes: Mode I – crack opening mode where the delaminated faces open away from each other, Mode II – in-plane shear mode where delamination grows due to an in-plane shear force or displacement perpendicular to the crack front, and Mode III: out-of-plane shear mode where the delamination grows due to an out-of-plane shear force or displacement parallel to the crack front.

Delamination damage in laminated composites can be triggered by an impact loading or a manufacturing geometric discontinuity, e.g. ply drops, bonded joints, etc. and cause severe loss of structural performance and fatigue life of the FRPs [4,61]. Therefore, accurate prediction of fracture behavior in the interlaminar region of the FRPs is crucial. There are two major

techniques for simulating the interlaminar crack propagation behavior of the FRPs using finite elements method (FEM); virtual crack closure technique (VCCT), and cohesive elements or cohesive zone modeling (CZM). VCCT, which was firstly proposed by Rybicki and Kanninen [61,62] applies a fracture mechanics technique to evaluate the energy release rates (G). The main assumption used in this technique is that the strain energy released as a crack propagates by a small amount is equal to the work needed to close the same crack. Depending on the crack propagation mode, the energy release rates of G_I, G_{II} and G_{III} can be computed using the nodal forces and displacements. This method can be effectively implemented via FE analysis by ABAQUS. This software package is capable of predicting the onset of crack initiation, as well as simulating stable and unstable crack propagation behavior [63]. However, for applying this method the initial crack front should be determined prior to the simulation, which could be very challenging to predict for complex crack geometries and loading situations [61]. Use of cohesive elements is an alternative way to simulate the interlaminar crack propagation phenomenon. Cohesive elements, which are based on Dugdale-Barenblatt cohesive zone approach [64,65], obey a strength-based failure criterion indicating the onset of crack softening process. Two major types of cohesive elements have been used in the literature; point cohesive elements, which are identical to non-linear spring elements [66,67], and continuous interface elements, which are finite- or zero-thickness volume elements connecting solid elements among which the fracture grows [68,69]. Zero-thickness volume elements can also be implemented in FEM using ABAQUS.

4.2.1 Virtual crack closure technique (VCCT)

In general, all crack closure methods are based on Irwin's closure integral [101-103]. These methods are based on the assumption that the energy released when a crack is extended by a

certain amount is equal to the work needed to close the crack by the same amount. The distinction between different crack closure methods is how to calculate the released energy or the work needed. In the crack closure technique, which is also called two-step method, (shown in Figure 4-1) when a crack is extended from a to $a + \delta a$ two steps are needed in order to calculate the amount of released energy.

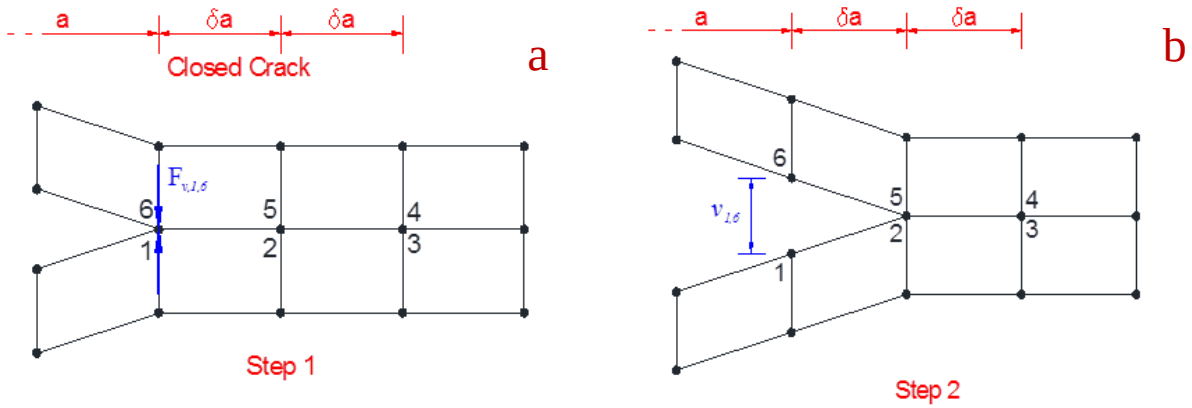

Figure 4-1. Crack closure technique (two-step method), (a) step one when the crack is closed, and (b) step two when crack is extended [101].

In this case, the energy release rate can be expressed by equation (4.1),

$$G_I = \frac{1}{2bd}(v_{1,6}F_{v,1,6}) \tag{4.1}$$

where G_I is the Mode I energy release rate, $F_{v,1,6}$ is the vertical force between nodes 1 and 6 in step 1, $v_{1,6}$ is the vertical displacement between nodes 1 and 6 in step 2, b is the width and d is the length of the elements at the crack tip. Inferred from equation (4.1), calculating the energy release rate requires two separate finite element analysis (steps 1 and 2). An alternative approach that requires single step to determine the energy release rate has been proposed [63,101]. This method is called modified or virtual crack closure technique (VCCT). The main assumptions in this method are identical to the two-step method. However, VCCT assumes that the state of the

crack tip would not change when crack extends from $a + \delta a$ to $a + 2\delta a$. Figure 4-2 shows the state of crack required to calculate the energy release rate.

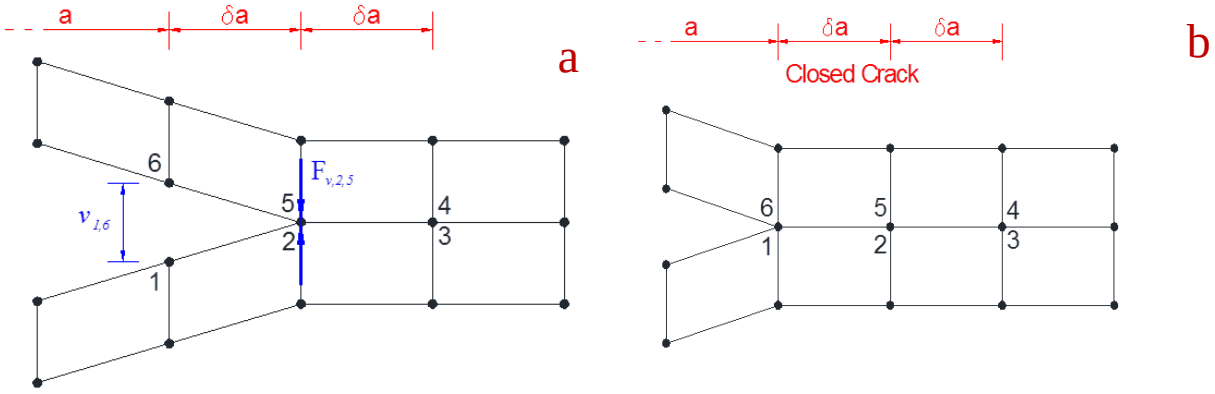

Figure 4-2. Virtual crack closure technique (VCCT), (a) when the crack is extended, and (b) when crack closes (similar to step 1 in the two-step method) [101].

Based on these assumptions, and right after one step of finite element analysis, the energy release rate can be calculated by equation (4.2).

$$G_I = \frac{1}{2bd}(v_{1,6}F_{v,2,5}) \tag{4.2}$$

Where, $F_{v,2,5}$ is the vertical force between nodes 2 and 5 at the crack tip, and $v_{1,6}$ is the vertical displacement between nodes 1 and 6 (one δa before crack tip).

Based on the calculated energy release rate, a fracture criterion can be defined by equation (4.3).

$$f = \frac{G_I}{G_{Ic}} \tag{4.3}$$

Where f is fracture criterion and G_{Ic} is the Mode I interlaminar fracture toughness. In the FEA, crack propagation starts when f reaches 1.0 within a tolerance range given by equation (4.4).

$$1.0 \leq f \leq 1.0 + f_{tol} \tag{4.4}$$

Where f_{tol} is the assumed tolerance for fracture criterion. When $f > 1 + f_{tol}$, the time increment needs to be cutback in order to satisfy the fracture criterion of equation (4.4). In the case of unstable crack growth problem, multiple nodes are allowed to separate at one time-increment. In this case, an unstable growth tolerance can be assumed for the fracture criterion as in equation (4.5).

$$1.0 + f_{tol} \leq f \leq 1.0 + f_{tol}^{u} \tag{4.5}$$

Where f_{tol}^{u} is the unstable crack growth tolerance. When this criterion is satisfied, no cutback in time would be considered. Instead, multiple nodes ahead of the crack tip would debond and their nodal forces be released at that time increment until $f < 1$. However, a cut back in time will be needed when $f > 1 + f_{tol}^{u}$. When the time increment is considered small enough, no upper limit for fracture criterion is needed, i.e., $f_{tol}^{u} = \infty$.

4.2.2 Cohesive elements

Cohesive elements can be two-dimensional or three-dimensional elements, usually with zero thickness, connecting the two faces of an interlaminar region in a composite laminate. Figure 4-3 illustrates a typical 8-node 3-D element. The thickness of the element is initially zero (t=0) and the debonding faces are shown on the element.

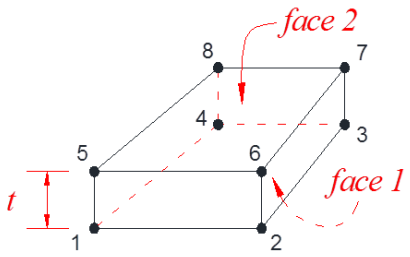

Figure 4-3. Schematic of an 8-node zero-thickness (t=0) cohesive elements. Faces 1 and 2 are initially overlaid and upon a tensile traction, debonding.

For pure Mode I loading condition, bilinear softening constitutive behavior, presented in Figure 4-4, has been commonly used in the literature [61,63]. This constitutive behavior represents the traction-separation relation inside cohesive elements. The traction-separation curve starts with a linear elastic portion followed by a degradation (or softening) line. The area under the traction-separation curve represents the energy release rate (G_{Ic}).

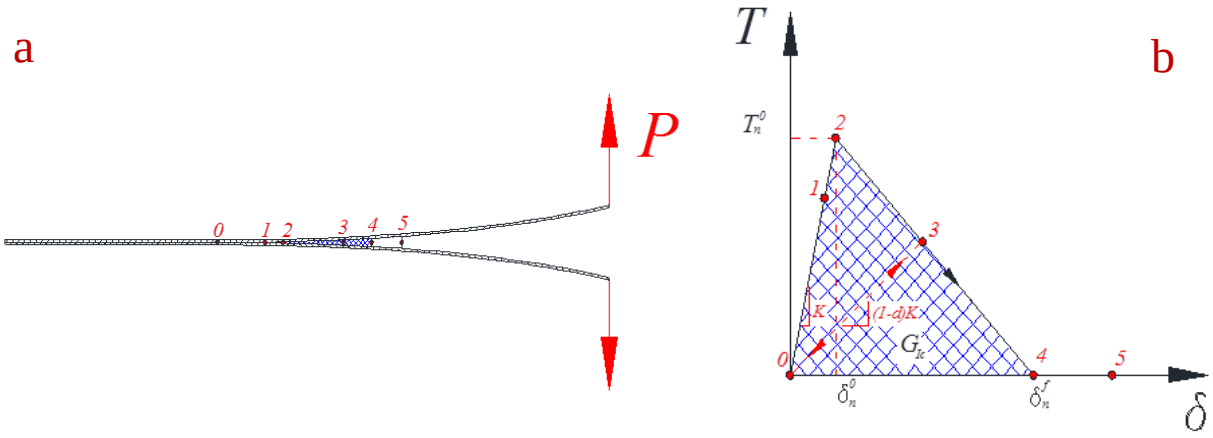

Figure 4-4. (a) Mode I loading on separating faces attached with cohesive elements, and (b) Bilinear traction-separation behavior for cohesive elements. The numbers on the curve shows the traction-separation status of different points on the separating faces of (a).

Cohesive elements can experience loading and unloading before they are fully damaged. Depending on the maximum separation they encounter during the loading history, their traction-separation curve for unloading could follow different stiffness. A mathematical representation for the bilinear constitutive behavior for the cohesive elements could be presented by equation (4.6) [61].

$$T = \begin{cases} K\delta \rightarrow \delta_n^{max} \leq \delta_n^0 \\ (1-d)K\delta \rightarrow \delta_n^0 < \delta_n^{max} < \delta_n^f \\ 0 \rightarrow \delta_n^{max} > \delta_n^f \end{cases} \tag{4.6}$$

Where, T is traction, δ is separation, δ_n^0 is the separation at damage initiation, δ_n^{max} is maximum separation experienced by the element during loading history, δ_n^f maximum separation where the element is fully damaged (or ultimate crack opening), K is stiffness ($K = \frac{T_n^0}{\delta_n^0}$), T_n^0 is maximum traction to initiate the damage (also called, interlaminar strength), and d is damage variable which can be defined as in equation (4.7).

$$d = \frac{\delta_n^f(\delta_n^{max} - \delta_n^0)}{\delta_n^{max}(\delta_n^f - \delta_n^0)} \tag{4.7}$$

Therefore, the damage variable is 0 at damage initiation (point 2 in Figure 4-4) and 1.0 at the last point where the element is fully damaged (point 4 in Figure 4-4).

4.2.3 Application in simulating Mode I delamination in hybrid CFRPs

Various mechanical and chemical approaches have been reported in the literature [4,6-8,26,55,56,87,96,99,104-106] to improve the interlaminar fracture toughness of the FRPs. The major challenge however, has been the negative effect of these methods on the in-plane performance of the FRPs [4,9]. Among these methods, integrating nano-sized reinforcements into the composites structures has had the minimal deteriorating effect on the in-plane mechanical performance of the FRPs. In the previous chapter, the effects of integrating surface grown multiwall carbon nanotubes (MWCNTs) and ZnO nanorods, and their synthesis environment on the interlaminar fracture toughness of hybrid CFRPs were investigated experimentally. In this chapter, Mode I interlaminar fracture toughness tests (DCB tests) of the designed hybrid CFRPs are simulated via FEM. 3D models of DCB specimens were developed utilizing ABAQUS. In the first set of simulations, optimum mesh size and number of load increments were achieved in order to effectively simulate the interlaminar crack growth

behavior. Afterwards, the VCCT was utilized in a new set of FEA simulations, for simulating the crack growth behavior of different designed CFRPs. In this models, average Mode I interlaminar fracture toughness values (G_{Ic} values), obtained from the experiments, were utilized. Stable crack growth behavior was observed as a result of this set of FEAs. Cohesive elements were employed in a new set of FEAs in order to simulate the crack growth behavior of the designed CFRPs and investigate the effect of different surface treatment on the interlaminar strength and ultimate crack opening of the CFRPs.

For the last set of FE models, fluctuations in the experimental measurements of G_{Ic}s were taken into account, in order to accurately simulate the unstable interlaminar crack growth nature of the designed CFRPs.

4.3 Method

4.3.1 Optimum loading increment and mesh size

A 3D model of a DCB specimen with identical dimensions to the reference sample tested in the experiments was developed. The model comprised two deformable solid shells with dimensions of 100.0×24.9 mm^2 representing the two separating parts of a DCB specimen. In order to create a pre-cracked DCB sample, each face was meshed coarsely in the pre-cracked and finely in the crack propagation regions, such that 900 elements were seeded in the crack propagation region. Figure 4-5 shows the meshed 3D model of the DCB specimen. The type of elements used in the model was solid 4-node shell (S4) elements. The length of the pre-cracked region was equal to the experimental sample's (34.0 mm for this case). The overlaying nodes from either faces of the model in the crack propagation region were tied together initially, and the VCCT fracture propagation criteria was defined between them. Mode I interlaminar fracture toughness (G_{Ic}) of

0.345 (N/mm) was input to the simulations. For boundary conditions, the nodes at the end of the specimen were constrained from moving in z-direction and rotating about y-direction. The nodes located along the lines at the tip of the DCB model were tied to the middle nodes of their corresponding line in order to simulate the piano hinges used in the experiments. Similar to the experiments, the loading input was applied on the hinges as a displacement with a constant rate throughout each simulation. The simulation terminated when the total separation at the hinges reach 40.0 mm. Figure 4-5(a) shows the created 3D model with all the inputs and Figure 4-5(b) shows the model with fully propagated interlaminar crack at the end of the simulation.

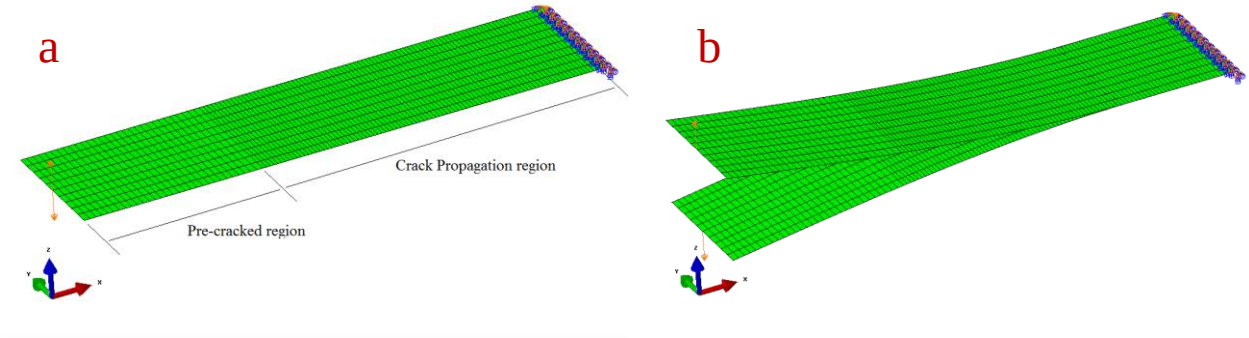

Figure 4-5. (a) 3D model of a DCB test specimen with boundary conditions and input loading, coarsely meshed in the pre-cracked region and finely meshed in the crack propagation region. (b) The model after crack propagation.

Six simulations were carried out for the DCB specimen shown in Figure 4-5 with different pre-considered number of loading increments. Different simulations possessed 5, 50, 100, 150, 350, and 1000 pre-considered loading increments to achieve the 40 mm displacement input at the hinges. The simulations were compared together as far as actual number of loading increments, number of divergent increments (in which the FE solver needed a cutback in time), FEA computation times, and the shape of load-displacement response of the FE models. As an outcome of this analysis, fully discussed in the next section, the simulation with 350 loading

increment was observed to have the optimum results. Therefore, the rest of the simulations were set to have 350 load increments.

For the next set of simulations, differently meshed models were developed. These models possessed 500, 900, 2400, and 4800 elements at the crack propagation region. The results of these simulations were compared together and optimum mesh size was selected among the different meshed DCB models. Figure 4-6 shows the various meshed models for this set of simulations. Among these models, the optimum number of elements in the crack propagation region belonged to the model with 2400 elements in the crack propagation region. The procedure of choosing this model is discussed in the next section.

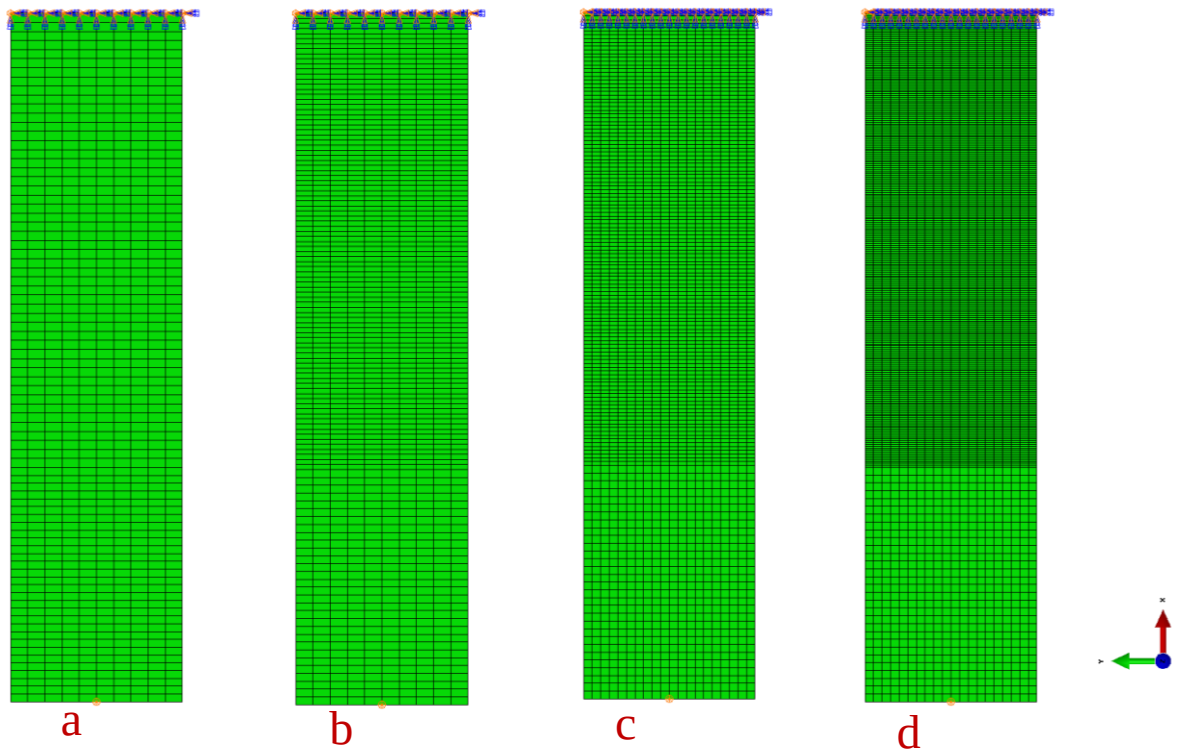

Figure 4-6. 3D models of a DCB specimen meshed with (a) 500, (b) 900, (c) 2400, and (d) 4800 elements in the crack propagation region.

4.3.2 VCCT for stable crack growth

From the previous sets of simulations, the optimum number of loading increment and element size suitable for a stable crack growth simulation were determined. Therefore, seven new FE models were developed for different DCB sample configurations. The designation of these FE models are identical to their experimental counterpart samples. The dimensions and the G_{Ic} values used for developing these models were obtained from averaging the experimental values. The linear orthotropic material model was chosen for the shell elements. However, since the loading is a simple concentrated force in a double cantilever beam (DCB) the most important material constant would be the elastic modulus along the beam span. This value was chosen from the results of the second chapter where the same material system was experimentally tested in tension. However, the E_1 values were normalized with regards to their fiber volume fractions. The other material constants are taken from [107]. The orthotropic material properties and the interlaminar fracture toughness values used in modeling the different sample configurations are listed in Table 4-1.

Table 4-1. Material properties employed for the FE models

config.	$E_1 = E_2$ (GPa)	E_3 (GPa)	ν_{12}	$\nu_{13} = \nu_{23}$	G_{12} (GPa)	$G_{13} = G_{23}$ (GPa)	G_{Ic} (kJ/m^2)
R1	52.5	10.0	0.1	0.18	7.0	5.0	0.3445
H	53.7	10.0	0.1	0.18	7.0	5.0	0.4005
PG	52.6	10.0	0.1	0.18	7.0	5.0	0.4628
UG	51.7	10.0	0.1	0.18	7.0	5.0	0.4191
R2	60.8	10.0	0.1	0.18	7.0	5.0	0.3874
W	60.5	10.0	0.1	0.18	7.0	5.0	0.3257
Z	58.8	10.0	0.1	0.18	7.0	5.0	0.2368

The VCCT approach was employed to simulate the stable interlaminar crack growth behavior of different sample configurations.

4.3.3 Cohesive elements for stable crack growth

A new set of FE models was created for studying the crack behavior utilizing cohesive elements. The 3D models were the same as the previous simulations. However, 8 node zero-thickness cohesive elements were added to the models in between the middle laminas in the delamination crack propagation region. Two parameters were necessary to define the behavior of the cohesive elements; stiffness (K in equation (4.6)), interlaminar strength (T_n^0 in equation (4.6)) and G_{Ic}. The load-displacement responses of the FE models were examined via several trial simulations with variable cohesive stiffness and interlaminar strength values, in order to achieve a good agreement with the experimental results. The details of the captured results are discussed in the next section. However, the results of the simulations turned out to be insensitive to the cohesive stiffness value, and highly sensitive to the interlaminar strength value. Furthermore, the higher interlaminar strength values resulted in sharper load-displacement curves. As a result of this set of numerical trials, the values of the interlaminar strength (T_n^0s) for different sample configurations were achieved. Ultimate crack openings (δ_n^fs) were also calculated for different CFRPs using the G_{Ic} and T_n^0 values. Ultimate crack opening could be indicating the capability of the bridging fibers to keep the crack closed.

4.3.4 VCCT for unstable crack growth

As observed in the experimental results, unstable crack growth behavior was the dominant response of the DCB specimens. Due to this sort of behavior, variable interlaminar fracture toughness values were measured along the crack length during the experiments. In order to accurately mimic the load-displacement and crack growth response of the DCB experimental

tests, random G_{Ic} values were assigned to the nodes along the crack growth path. However, the randomly assigned G_{Ic} values, possessed average values and standard deviations identical to the average experimental values and the standard deviations of each sample configuration. As a result, the FE model can be viewed as an additional experimental specimen. The G_{Ic} values assigned to the nodes along the crack growth regions, for different sample configuration, are shown in the plots of Figure 4-7 and Figure 4-8. Similar to section 4.3.2, the VCCT was employed in this set of simulations.

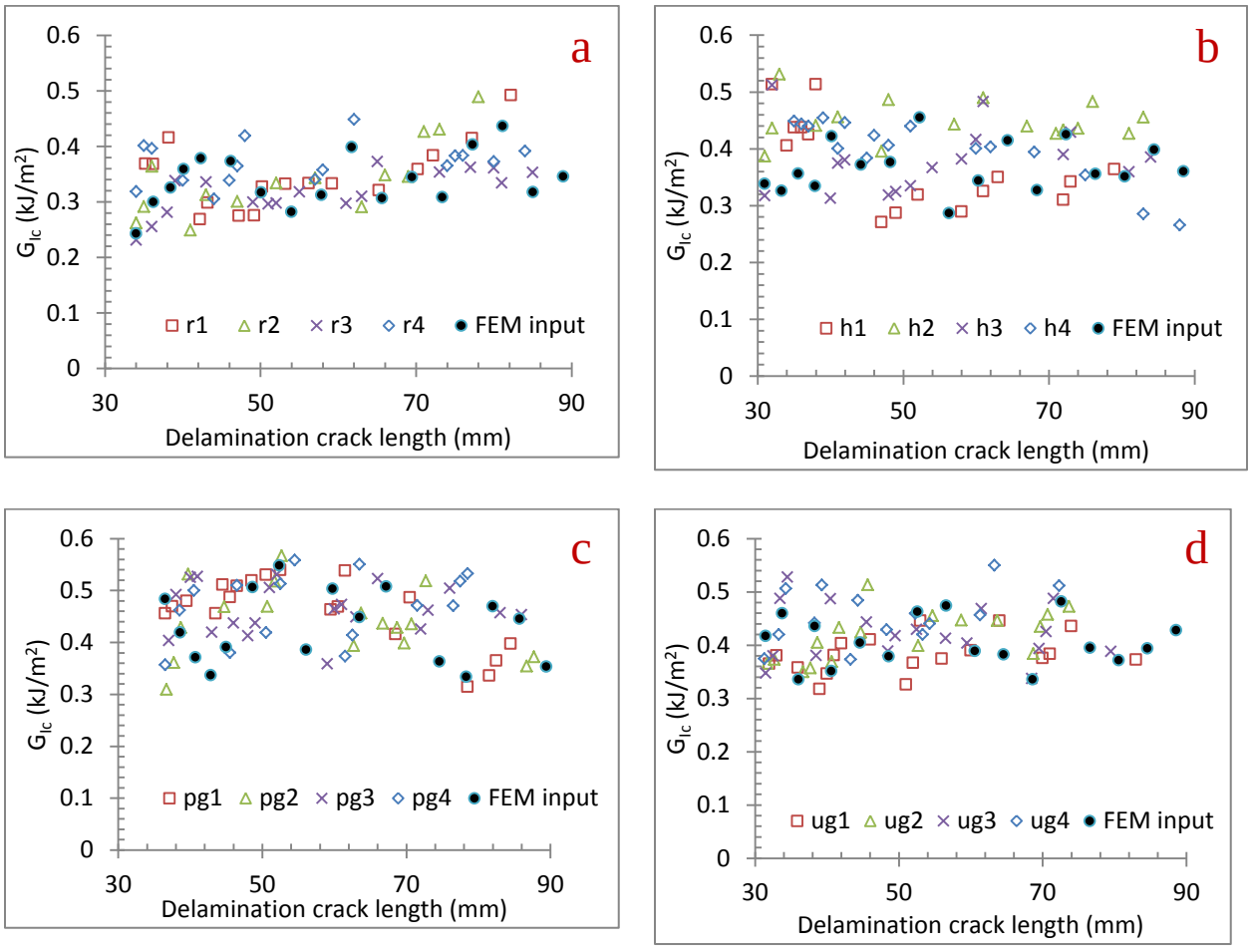

Figure 4-7. The input interlaminar fracture toughness values assigned to the nodes along the crack propagation region for (a) R1, (b) H, (c) PG, and (d) UG sample configurations. The experimental results are also shown in the plots.

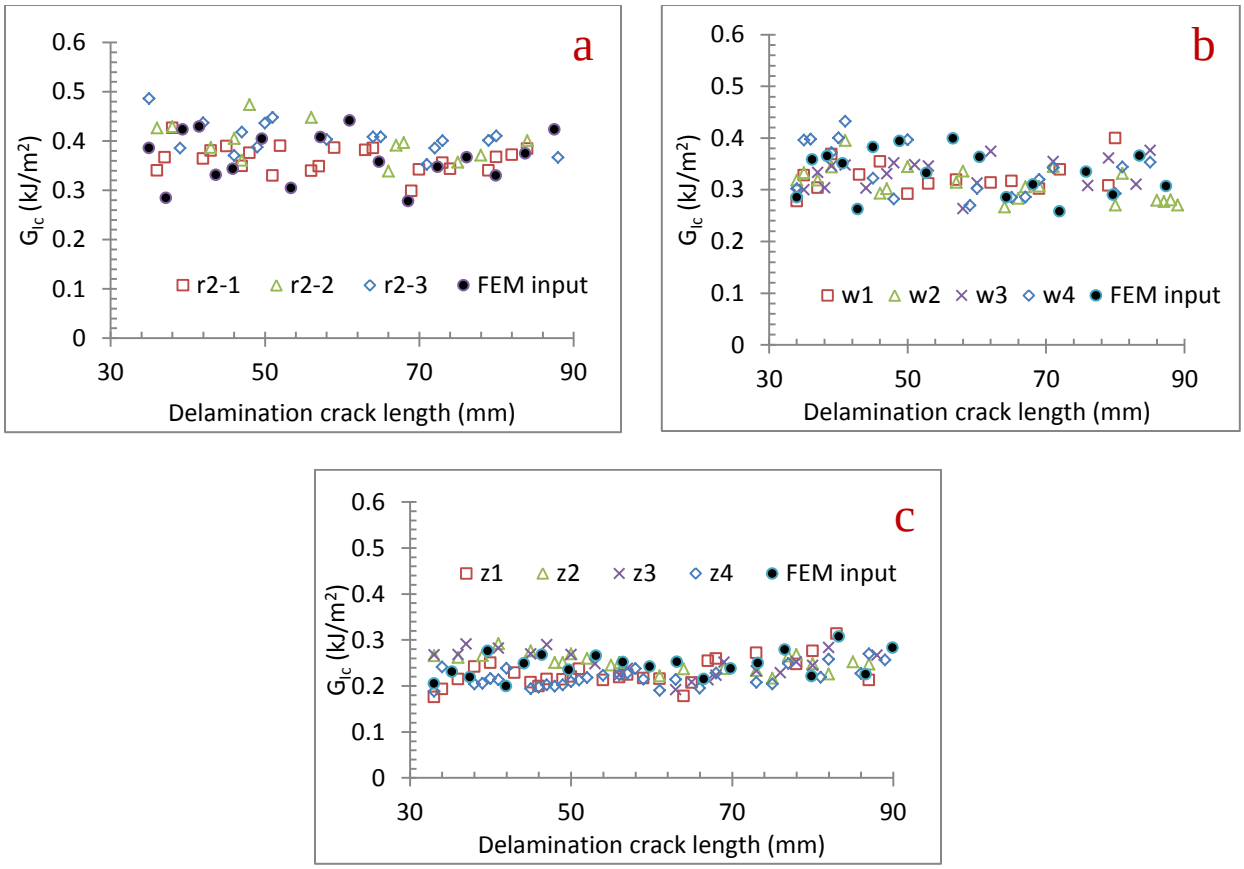

Figure 4-8. The input interlaminar fracture toughness values assigned to the nodes along the crack propagation region for (a) R2, (b) W, and (c) Z sample configurations. The experimental results are also shown in the plots.

4.4 Results and discussion

4.4.1 Optimum loading increment and mesh size

As mentioned in the previous section, a 40 mm displacement was applied at the hinges of the 3D DCB models. In order to capture an accurate load-displacement response, this input displacement loading needed to be applied via enough number of small load increments. Six simulations were run with different pre-considered number of load increments. The ABAQUS solver was allowed to change the load increments to converge the running simulation. Table 4-2 lists these simulations and their captured results.

Table 4-2. Simulations for determining the optimum number of loading increments.					
Simulation number	Number of pre-considered load increments	Number of load increments needed for convergence	Number of cut-backs in load increments	Computation time (s)	Load-displacement curve
1	5	75	75	561	Unsatisfactory
2	50	82	64	543	Unsatisfactory
3	100	105	11	411	Unsatisfactory
4	150	152	-	483	Unsatisfactory
5	350	352	-	940	Satisfactory
6	1000	1002	-	2543	Satisfactory

The first three simulations needed several cutbacks in load increments by the solver to reach a converging solution. However, their load-displacement response curves were not satisfactory. Figure 4-9 shows the load-displacement response of DCB models at the hinges.

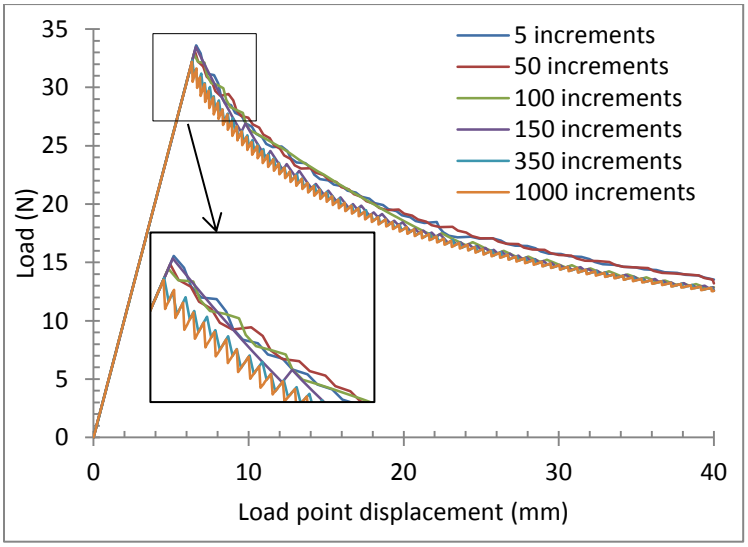

Figure 4-9. Load-displacement curves of the simulation with different numbers of increments.

Fourth simulation with 150 pre-considered load increments did not need any cutback in load increment. However, the magnified inset in Figure 4-9 suggests that the only simulations with

satisfactory load-displacement response were the last two simulations. The last simulation with the finest load increment (6^{th} simulation) possessed the best load-displacement curve. However, this simulation took 2543 s of computation time, which is almost 2.5 times the time needed for 5^{th} simulation. Therefore, the optimum simulation, as far as the computation time and the load-displacement response, was the 5^{th} simulation with 350 pre-considered number of load increment.

As mentioned in the previous section, in order to reach an optimum mesh size, four different models were developed with different mesh sizes in the crack propagation region. The simulations are listed in Table 4-3 and their load-displacement curves are shown in Figure 4-10.

Table 4-3. Simulations for determining the optimum mesh size.

Number of simulation	Number of elements	Element size (mm × mm)	Computation time (s)	Smoothness of response curve
5-1	500	(2.490 × 1.320)	581	Unsatisfactory
5-2	900	(2.490 × 0.733)	940	Unsatisfactory
5-3	2400	(1.245 × 0.550)	3001	Satisfactory
5-4	4800	(1.245 × 0.275)	11387	Satisfactory

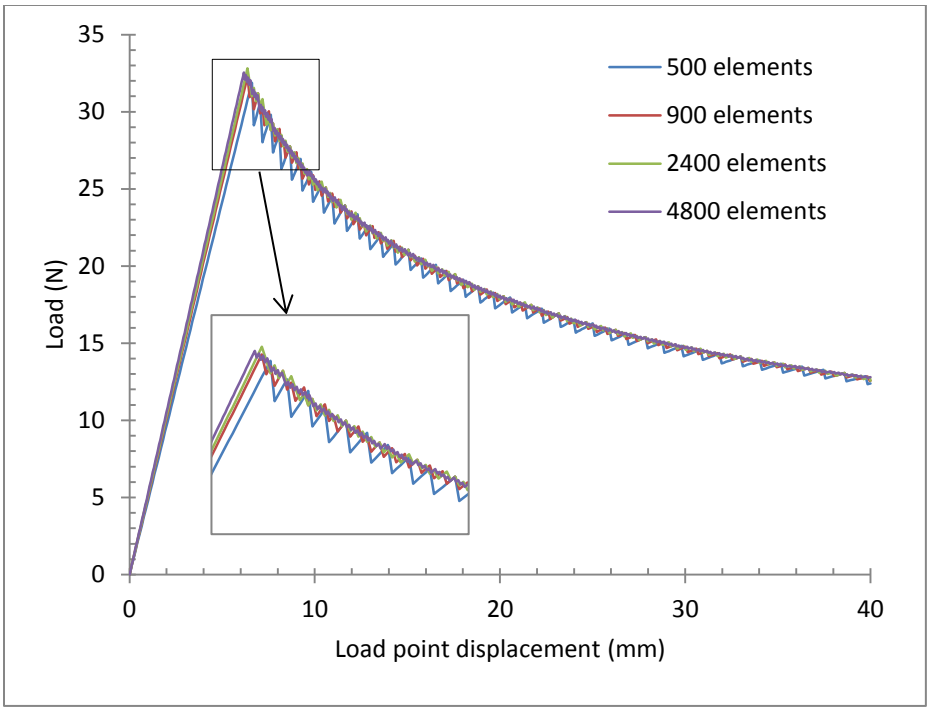

Figure 4-10. Load-displacement curves of the simulation with different number of elements.

As observed in the magnified inset of Figure 4-10, simulations 5-1 and 5-2 did not result in smooth enough load-displacement curves, while the last two simulations (5-3 and 5-4) yielded smoother load-displacement behavior. The finer mesh sized simulation (5-4) produced the smoothest curve. However, the computation time needed for this simulation was almost 3.5 times the simulation with 2400 elements (5-3). Therefore, the optimum model as far the mesh size and load increment was determined to have 2400 element in the crack propagation region solved in 350 load increments.

4.4.2 Stable interlaminar crack growth using VCCT

One simulation per sample configuration was performed in order to investigate the stable crack growth behavior of the 3D models of the DCB samples. Figure 4-11 and Figure 4-12 show the load-displacement curves of different FE models in comparison with the experimental results.

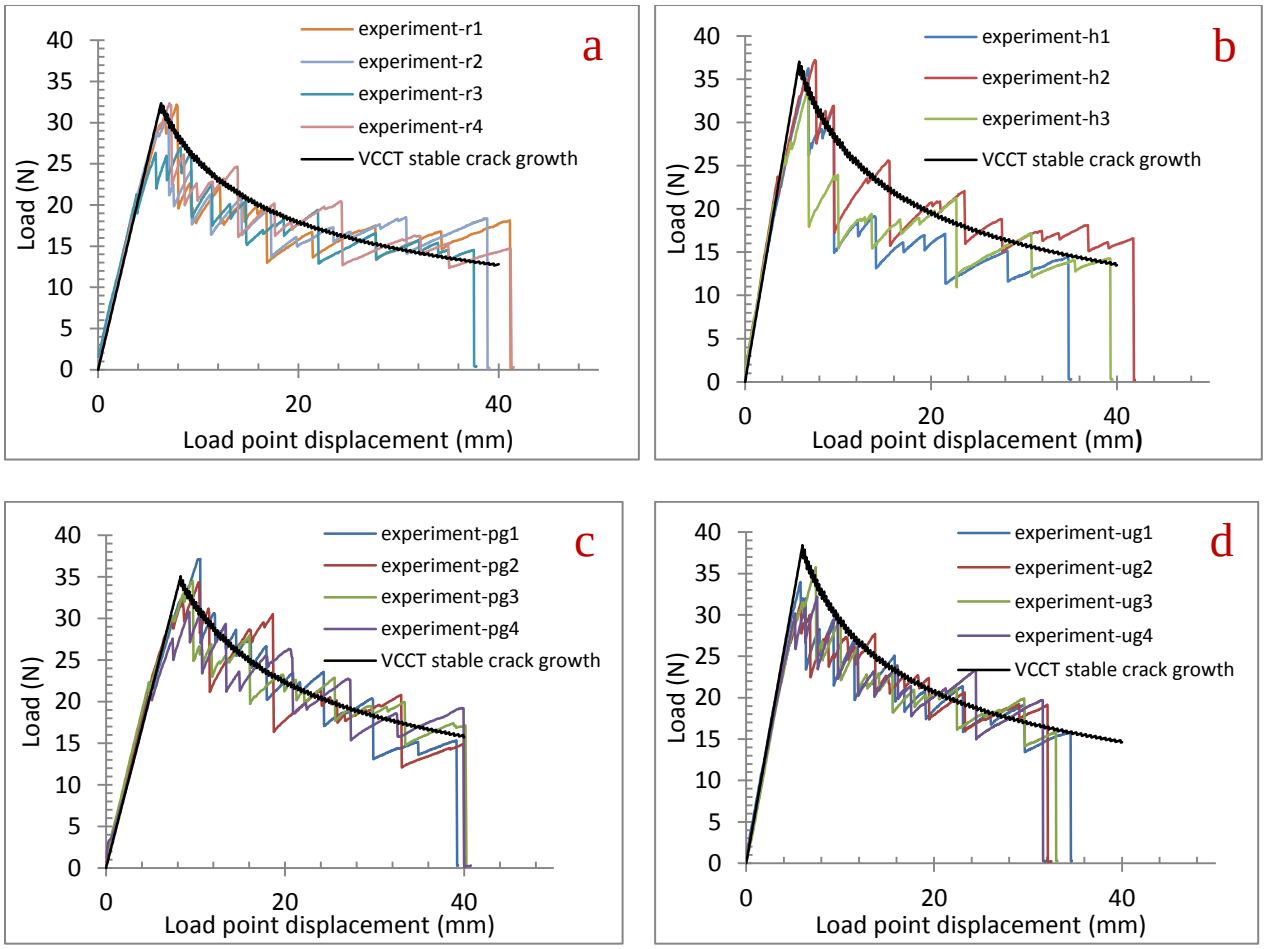

Figure 4-11. Load-displacement curves of the simulations of stable crack growth using VCCT for (a) R1, (b) H, (c) PG, and (d) UG sample configurations. The experimental results are also shown in the plots.

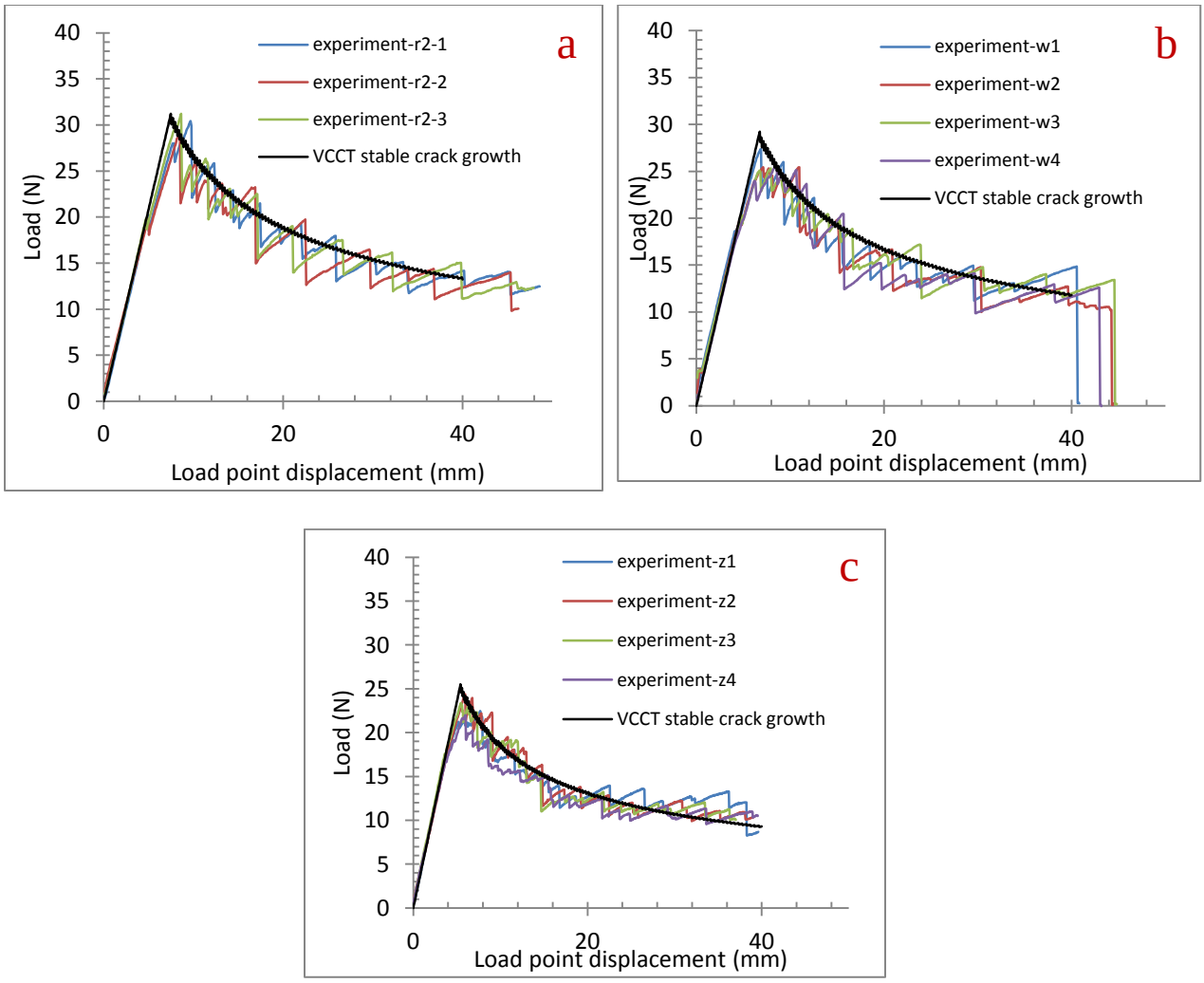

Figure 4-12. Load-displacement curves of the simulations of stable crack growth using VCCT for (a) R2, (a) W, and (c) Z sample configurations. The experimental results are also shown in the plots.

Figure 4-11 and Figure 4-12 show that the stable crack growth was unable to capture the fluctuations in the load, as the crack grows. However, the FEM curves pass through the local load peaks of the experimental results. This is due to the fact that the experimental interlaminar fracture toughness values were measured at these local peak points, where cracks jumped to grow. These interlaminar fracture toughness values measured at the peak points were averaged and used in the FE models as a constant value through the crack growth region. Figure 4-13 and

Figure 4-14 show the crack growth behavior of the FE models in comparison with the experimental observations. The FE results are in good agreement with the experimental results.

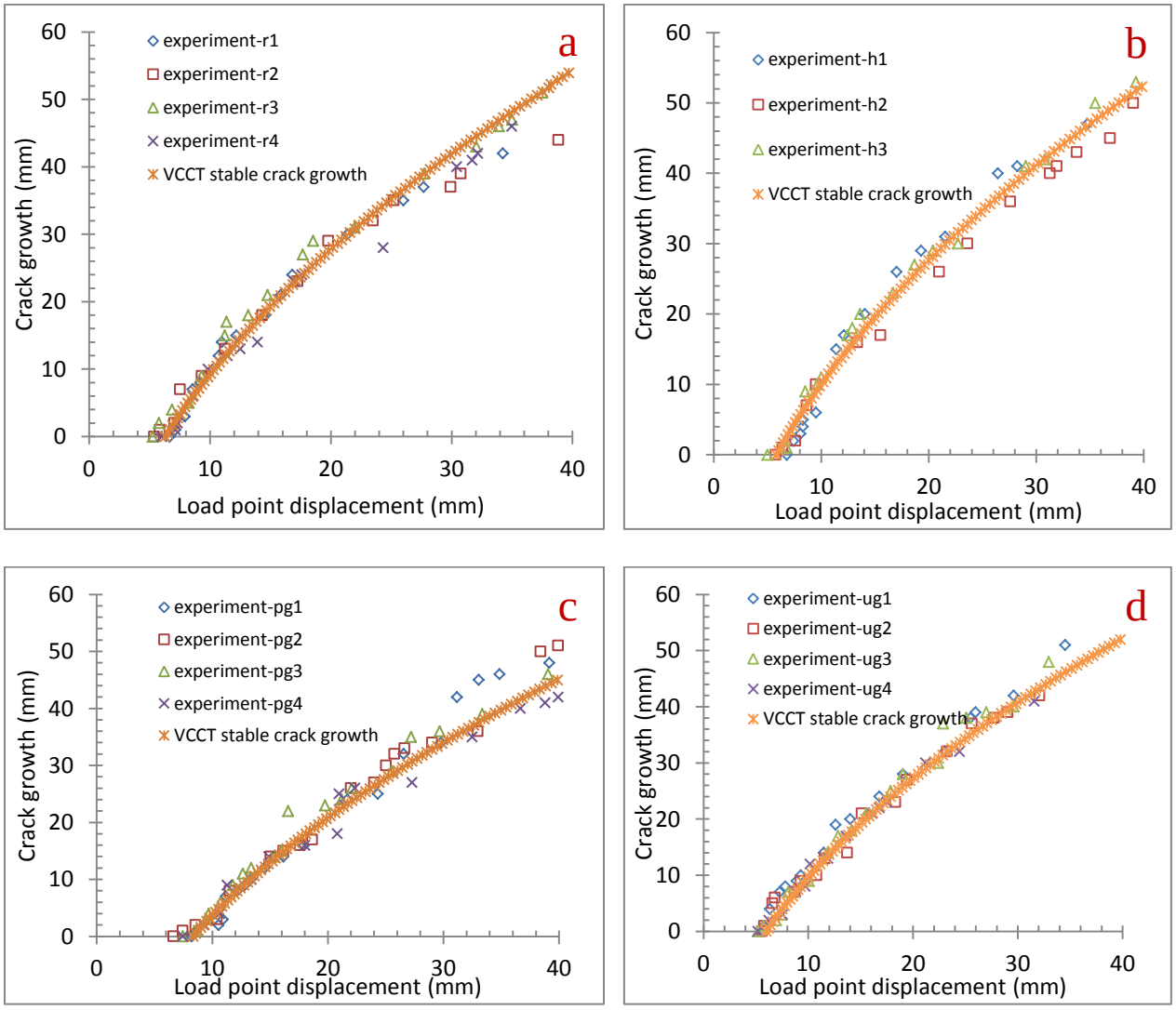

Figure 4-13. Crack growth results of the stable crack growth simulations with VCCT in comparison with the experimental results for (a) R1, (b) H, (c) PG, and (d) UG sample configurations.

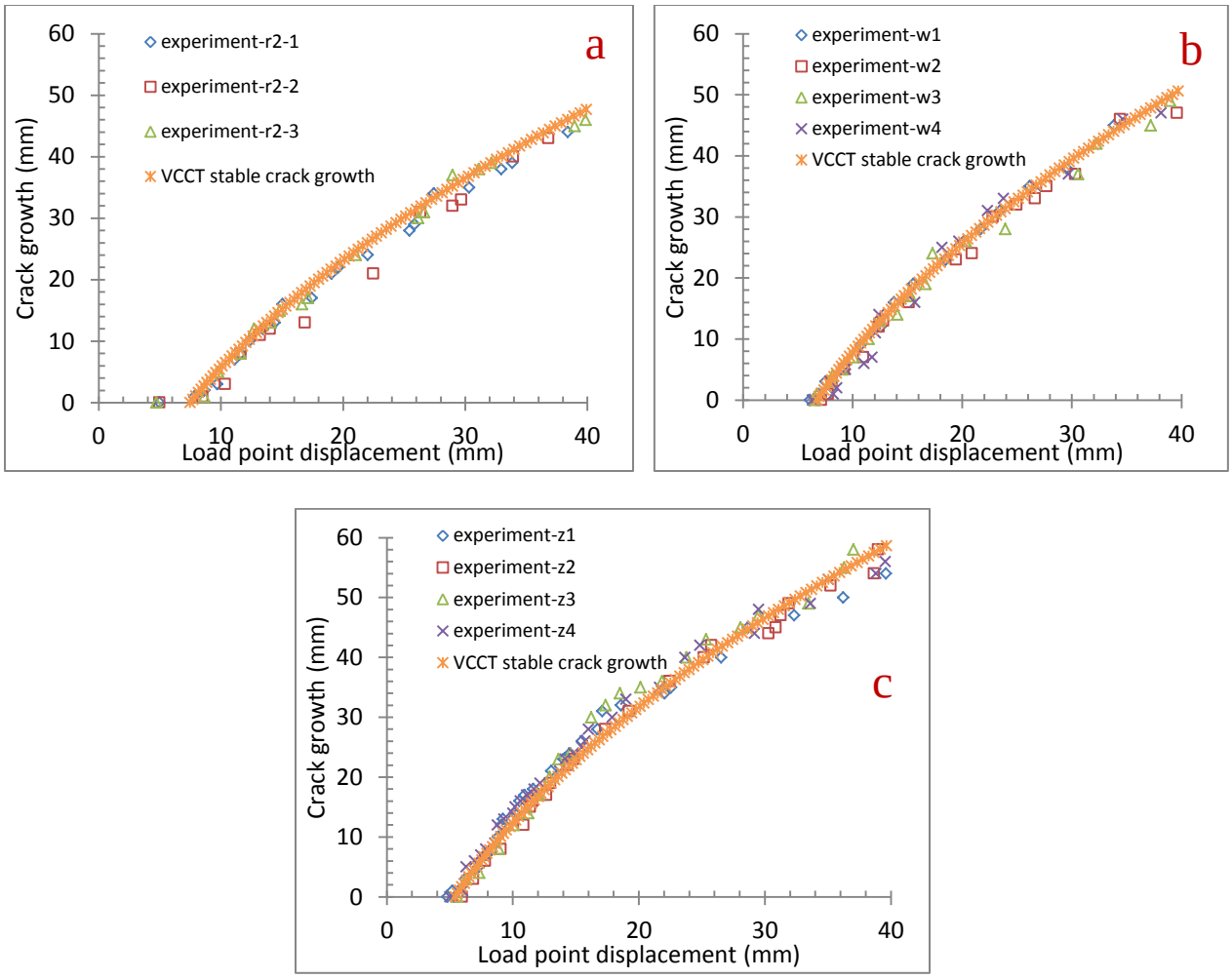

Figure 4-14. Crack growth results of the stable crack growth simulations with VCCT in comparison with the experimental results for (a) R2, (b) W, and (z) Z sample configurations.

4.4.3 Interlaminar crack growth simulations using cohesive elements

As mentioned in the previous section, cohesive elements were added to the models in the interlaminar region in order to simulate the crack growth behavior for the purpose of estimating interlaminar strengths of the designed hybrid CFRPs. Trial simulations were run using various input values for interlaminar strength. For each simulation the load-displacement curves were obtained and compared to the experimental results. The slope of a line passing through the origin and the point with the highest load on the curve was calculated for each simulation. The slope of

an identical line for each experimental load-displacement curve was also calculated. Amongst the different simulations, the simulation with the closest slope value to the average value of the experimental results was chosen to be the primary simulation with the utmost agreement with the experimental results. In other words, the input interlaminar strength in this simulation was considered to be the interlaminar strength value for its CFRP configuration counterpart. Figure 4-15 and Figure 4-16 show the load-displacement curves of the simulations with cohesive elements in comparison with the experiments.

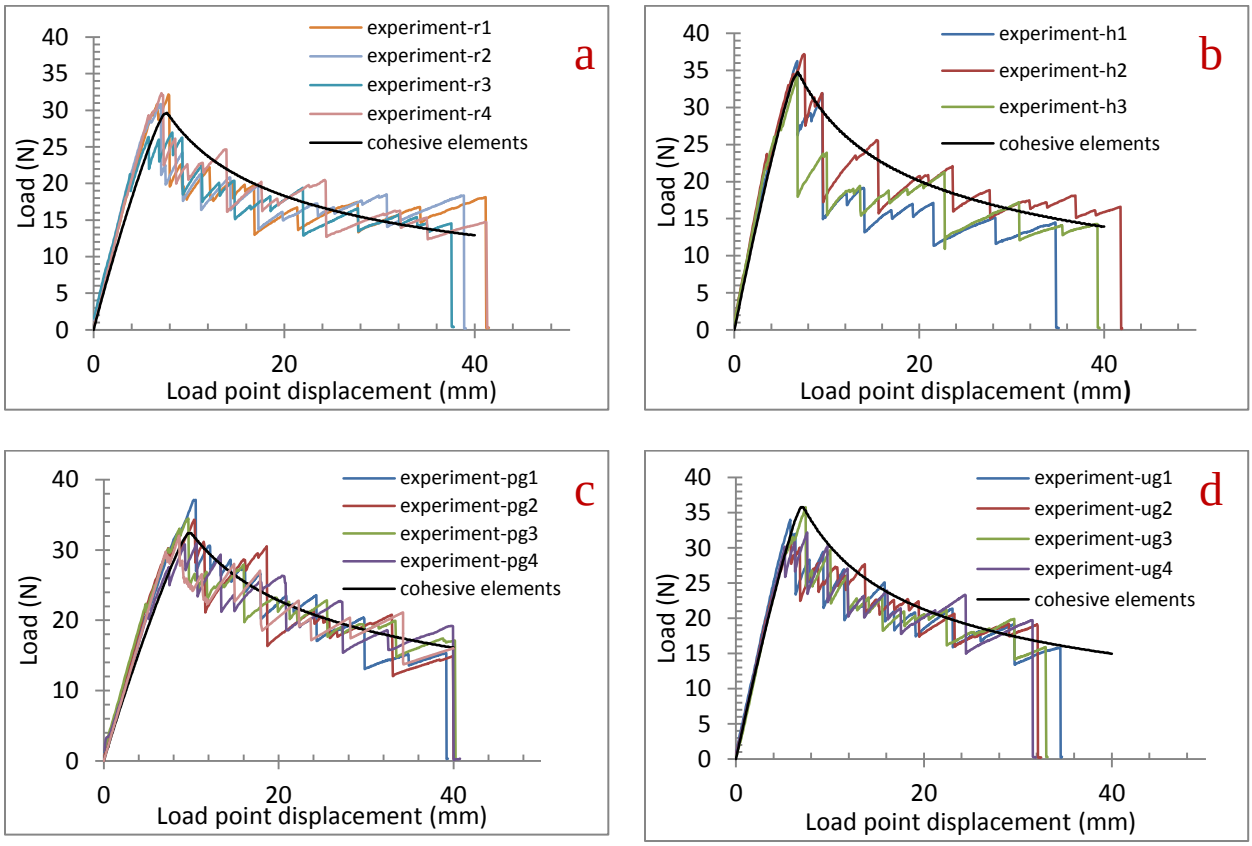

Figure 4-15. Load-displacement curves of the stable crack growth simulations using cohesive elements in comparison with the experimental results for (a) R1, (b) H, (c) PG, (d) UG sample configurations.

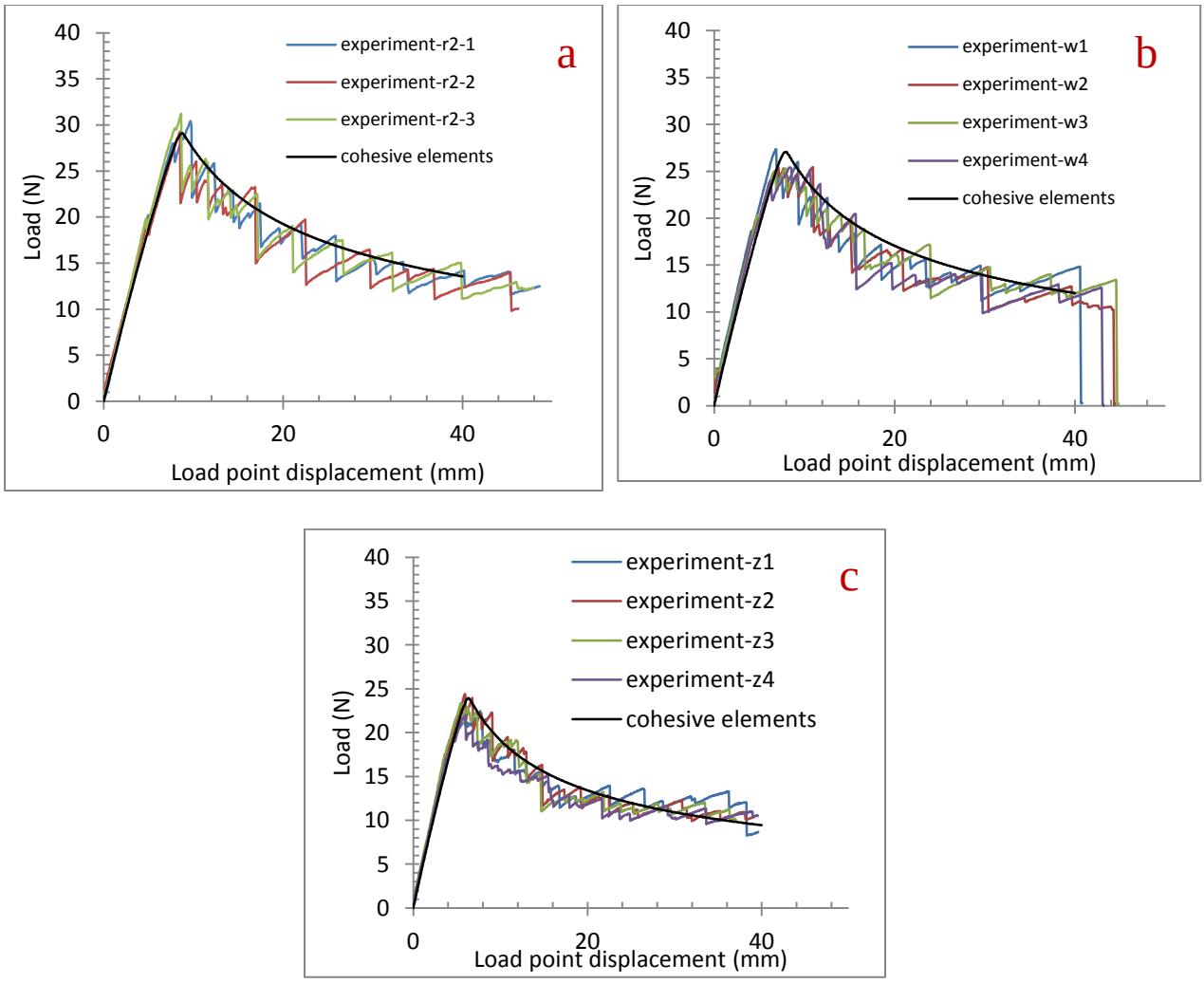

Figure 4-16. Load-displacement curves of the stable crack growth simulations using cohesive elements in comparison with the experimental results for (a) R2, (b) W, and (c) Z sample configurations.

It was seen that, similar to the results of the stable crack growth modeling with VCCT (Figure 4-11 and Figure 4-12), the load displacement curves of the FEMs based on cohesive elements could also capture the local peaks of the experimental results. However, this method was unable to capture the fluctuation existed in the curves obtained from the experiments. Using the results of the simulations, the interlaminar strength (T_n^0 in Figure 4-4) and ultimate crack

opening (δ_n^f in Figure 4-4) for the designed hybrid CFRPs were calculated and shown in Figure 4-17.

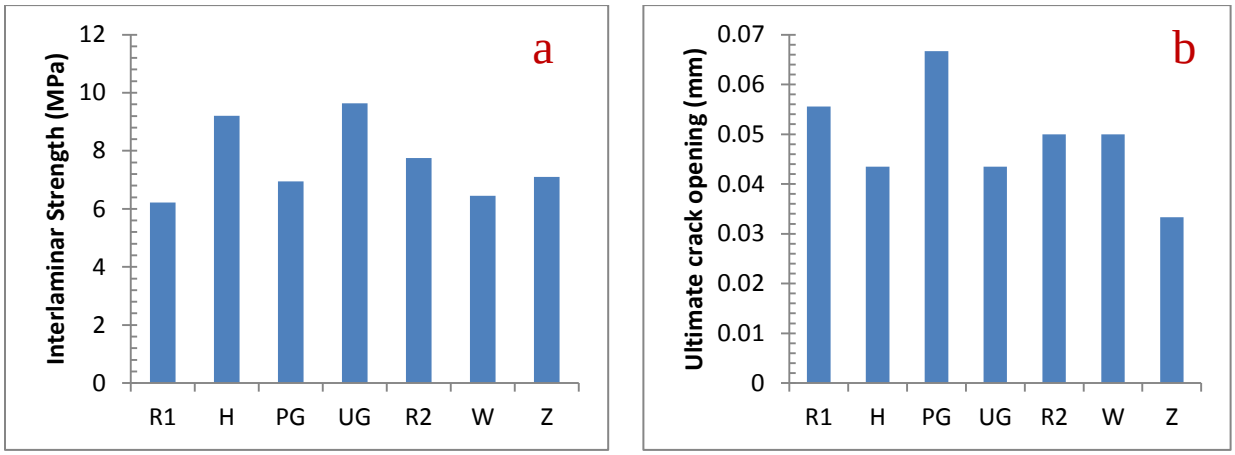

Figure 4-17. Interlaminar strength (a) and ultimate crack opening (b) values for the designed hybrid CFRPs based on first reference (R1), heat-treated (H), patterned GSD grown MWCNTs (PG), uniform GSD grown MWCNTs (UG), second reference (R2), hot-water exposed (W), ZnO nanorods grown (Z) fibers.

The hybrid CFRP based on the uniform GSD grown MWCNTs fibers (UG) possessed the highest interlaminar strength (55% higher than the reference CFRP). This improvement could be due to the promoting effects of the surface grown MWCNTs on the fiber matrix interface at the interlaminar region. On the other hand, the hybrid CFRP based on the patterned GSD growth MWCNTs fibers (PG) showed the highest ultimate crack opening (20% improvement). The outstanding tensile strength and strain-to-failure of this hybrid CFRP [29] can be responsible for this improvement causing the bridging fibers to stand the load longer before the final crack opening. However, the weak adhesion between the ZnO nanorods and the carbon fibers has decreased the interlaminar strength and ultimate crack opening of the CFRPs, 8.3% and 33.3% respectively.

Using cohesive elements, the crack growth behavior of the FE models was captured and plotted in Figure 4-18 and Figure 4-19 in comparison with the experimental results.

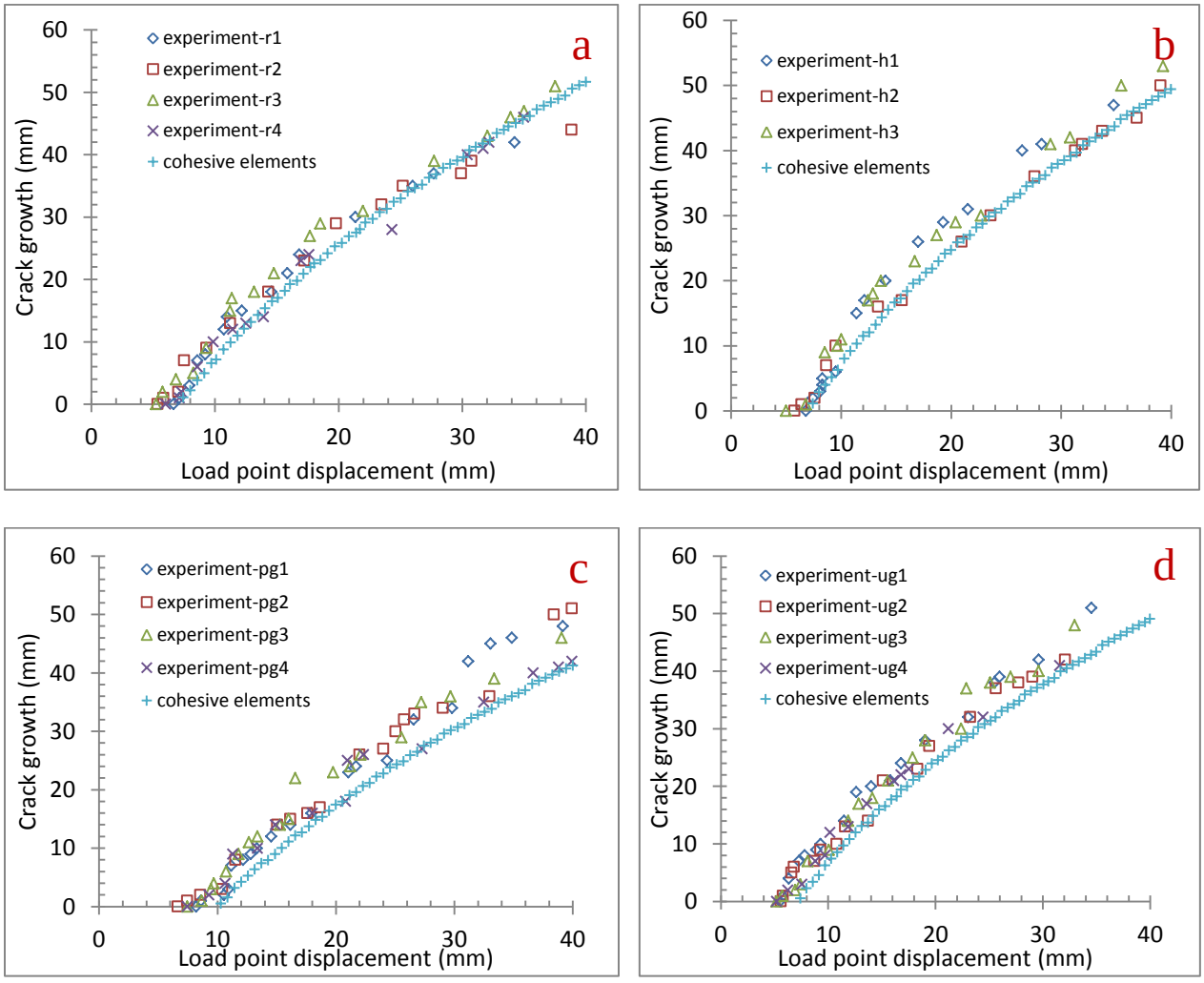

Figure 4-18. Results of the stable crack growth simulations using cohesive elements in comparison with the experimental results for (a) R1, (b) H, (c) PG, and (d) UG sample configurations.

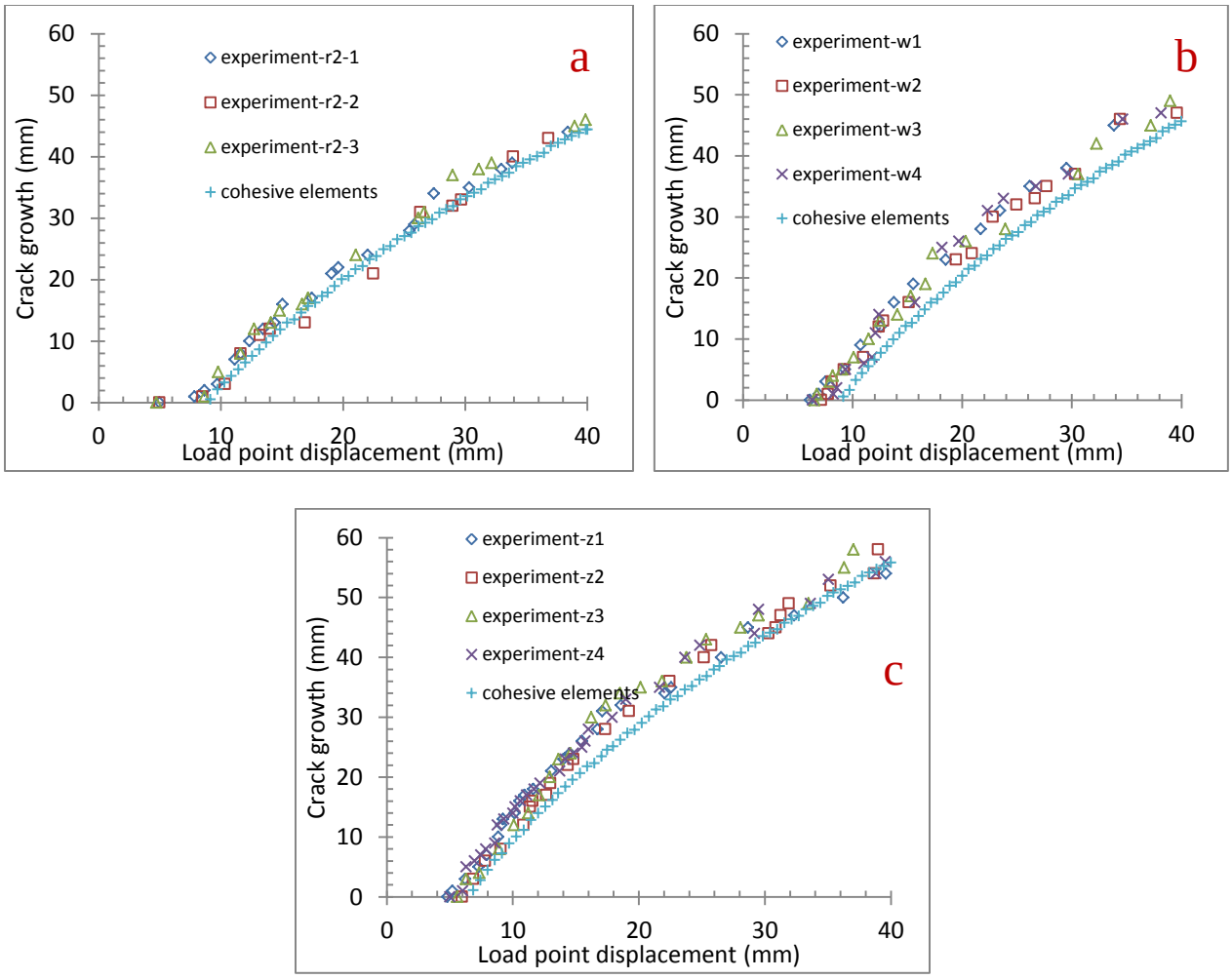

Figure 4-19. Results of the stable crack growth simulations using cohesive elements in comparison with the experimental results for (a) R2, (b) W, and (c) Z sample configurations.

Inferred from the results of Figure 4-18 and Figure 4-19, the FE simulations of cohesive elements for almost all the configurations, underestimated the crack growth length. The reason is that in the FEAs using the cohesive elements, the crack front is where the cohesive elements are fully damaged. In contrast, in the FEAs based on VCCT, the crack front is where the two overlaying nodes just separated.

4.4.4 Unstable crack growth modeling with VCCT

In Chapter 3, experiments suggested that the crack growth behavior of the designed hybrid CFRPs was unstable. Therefore, the stable crack growth modeling using either cohesive elements or VCCT with average G_{Ic} for all the crack propagation area could not successfully mimic the experimental mechanical response of the DCB specimens. Integrating the uncertainty in the measured G_{Ic} along the crack growth region, VCCT method was used to numerically model the unstable crack growth behavior of the designed hybrid CFRPs. Using the input G_{Ic} values along the crack length, represented in Figure 4-7 and Figure 4-8, the FE models were developed. The load-displacement curves of the results are shown in Figure 4-20 and Figure 4-21.

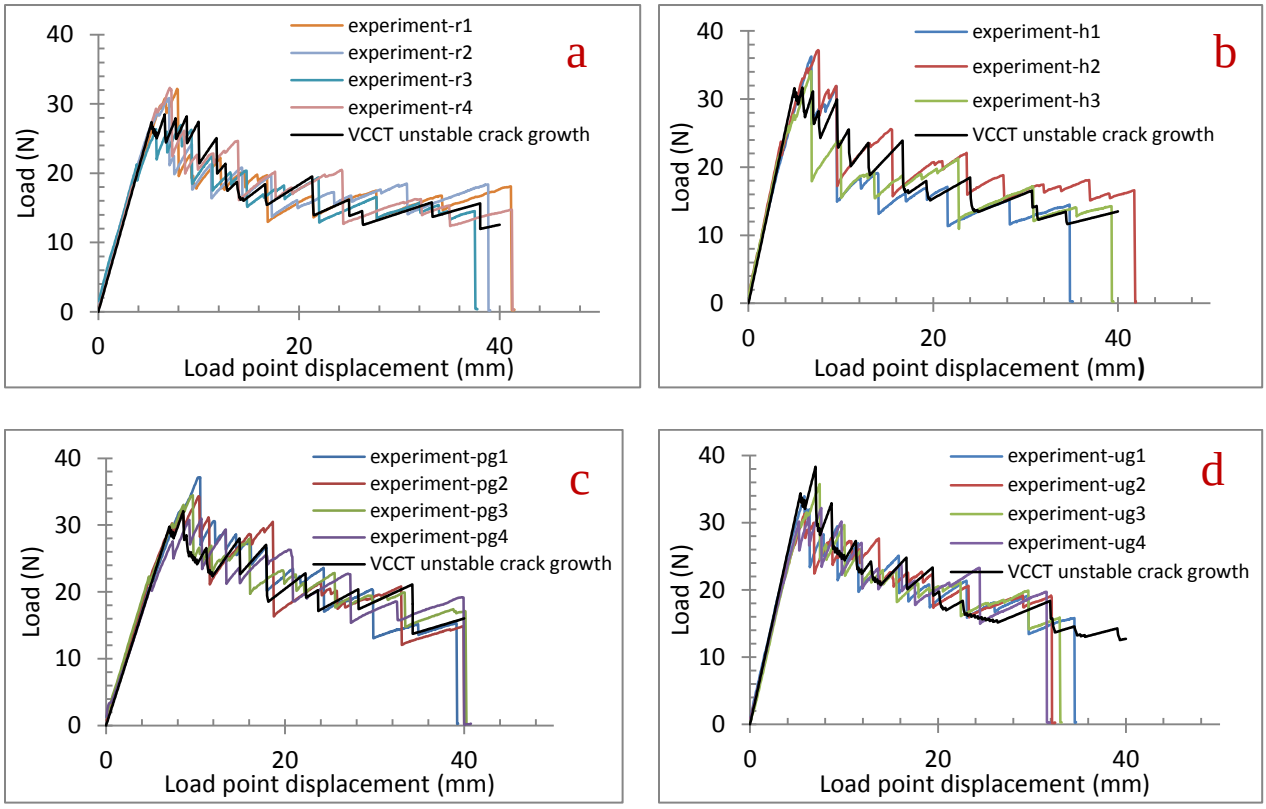

Figure 4-20. Load-displacement curves of the simulations of unstable crack growth using VCCT for (a) R1, (b) H, (c) PG, and (d) UG sample configurations. The experimental results are also shown in the plots.

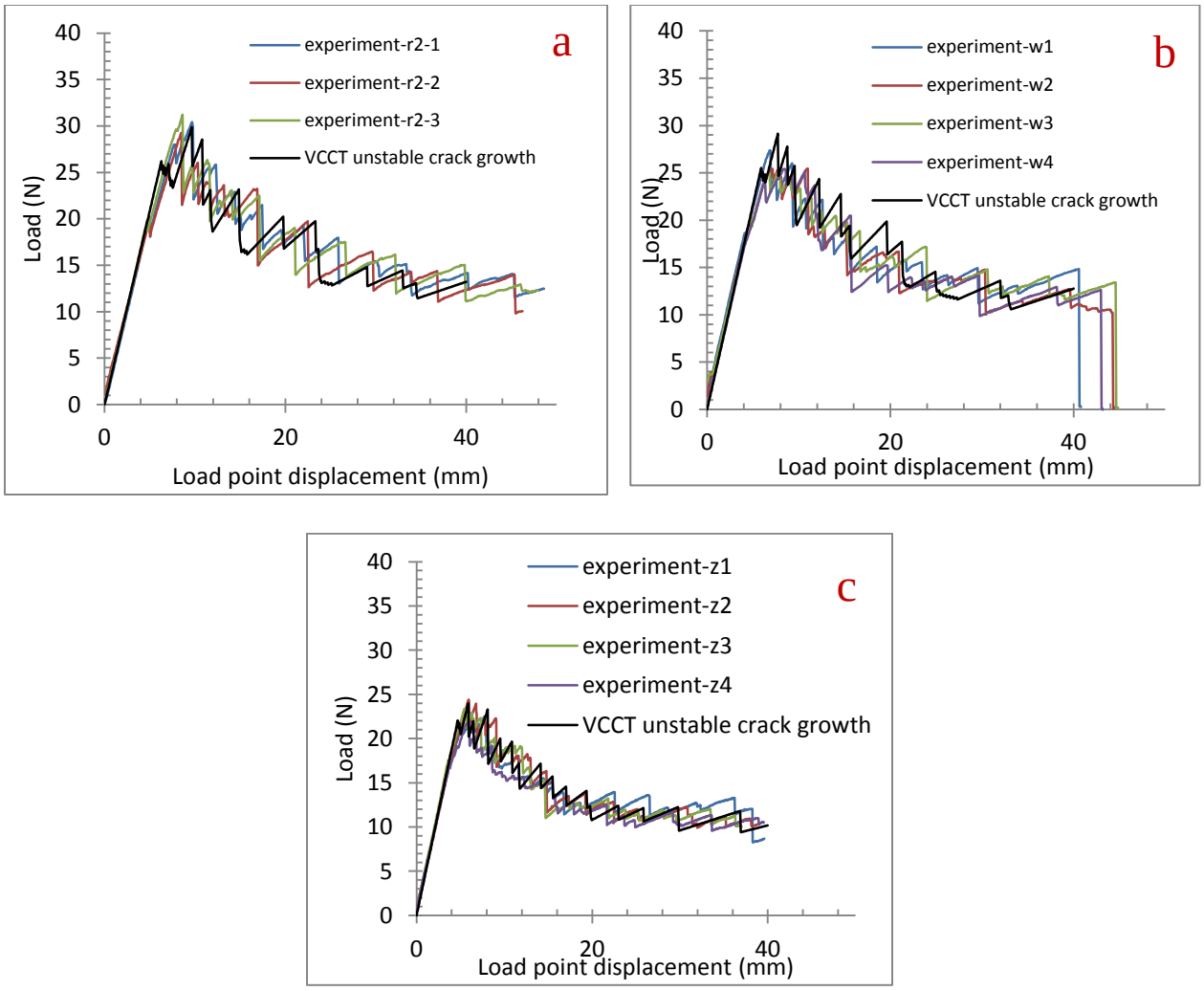

Figure 4-21. Load-displacement curves of the simulations of unstable crack growth using VCCT for (a) R2, (b) W, and (c) Z sample configurations. The experimental results are also shown in the plots.

Inferred from the load-displacement curves of Figure 4-20 and Figure 4-21, the mechanical response of the FE models developed using this method are almost undistinguishable from the experimental curves. The crack growth responses of these FE models are also shown in Figure 4-22 and Figure 4-23.

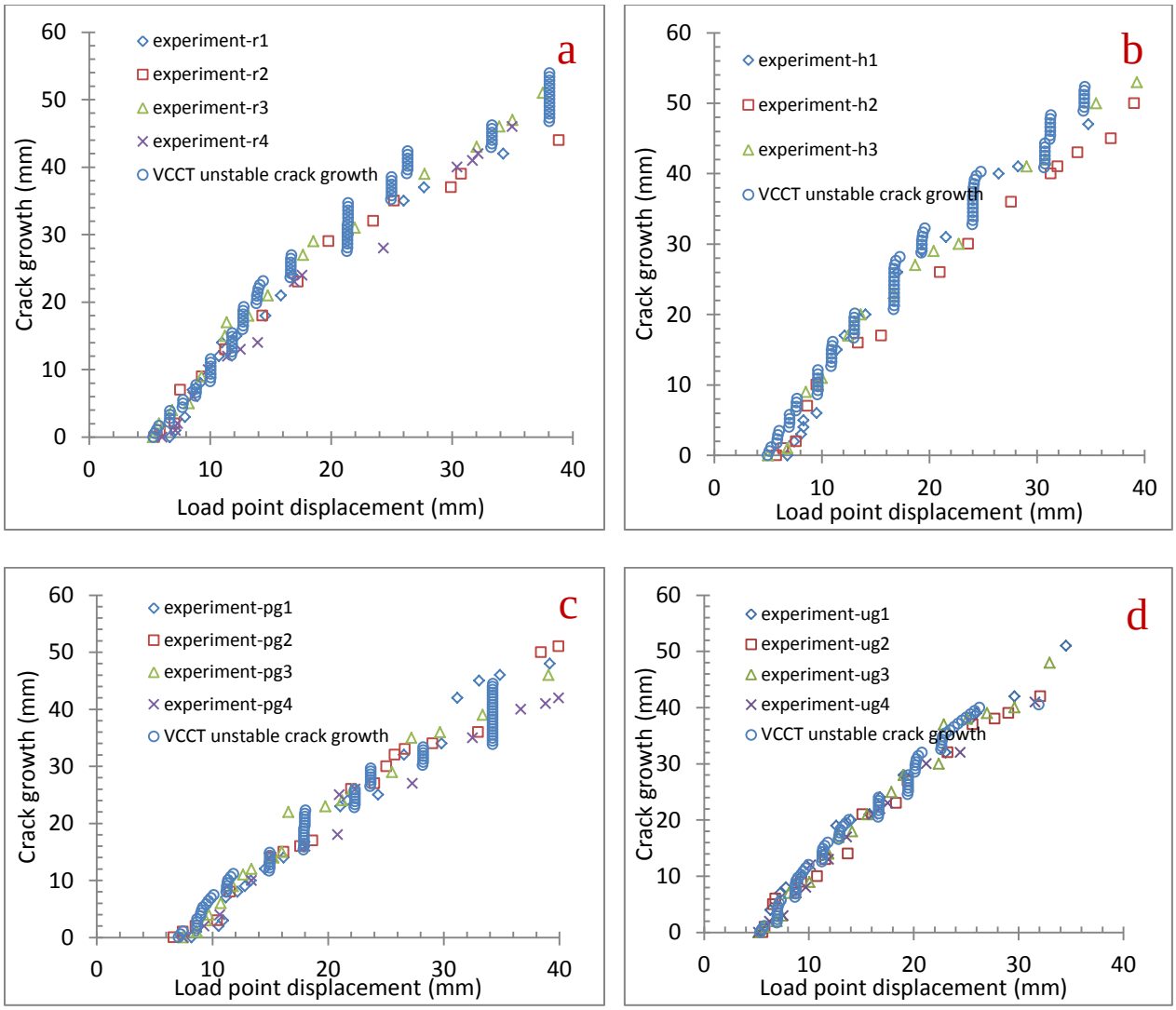

Figure 4-22. Results of the unstable crack growth simulations with VCCT in comparison with the experimental results for (a) R1, (b) H, (c) PG, and (d) UG sample configurations.

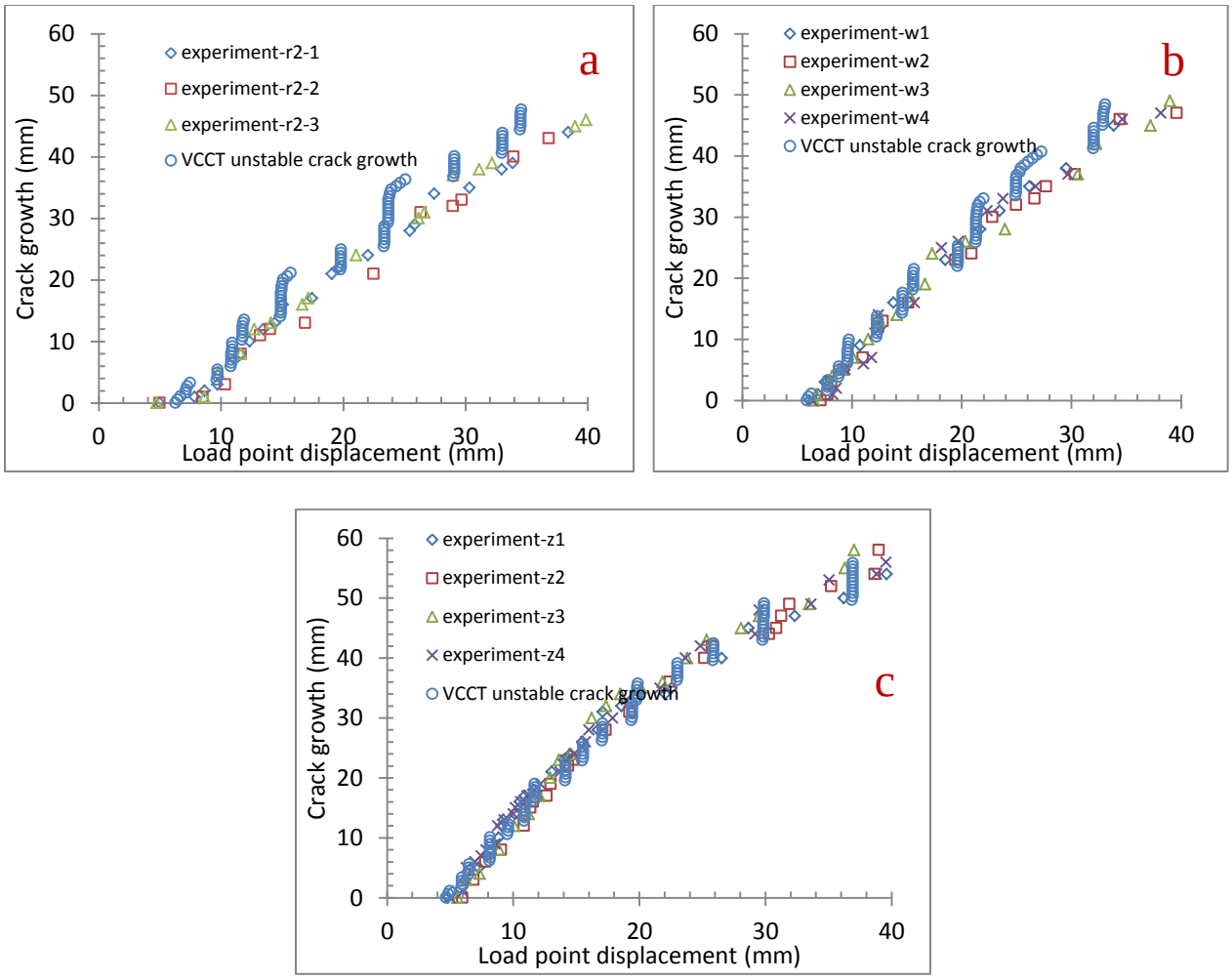

Figure 4-23. Results of the unstable crack growth simulations with VCCT in comparison with the experimental results for (a) R2, (b) W, and (c) Z sample configurations.

The FEM showed great agreement with the experimental results. It is worth noting that the vertical lines shaped by the circular markers of the FEM results represent the sudden jumps in the crack length due to the nature of unstable crack growth.

4.5 Conclusions

Finite element analysis was employed to simulate the Mode I interlaminar crack growth behavior of hybrid carbon fiber reinforced polymer composites. At first, virtual crack closure technique

(VCCT), which is based on linear elastic fracture mechanics (LEFM) assumptions, was employed to obtain optimum FE model parameters, i.e. mesh size and number of load increments. Then, VCCT-based FE models were developed for different CFRPs sample configurations to simulate the stable crack growth behavior of the CFRPs. The mode I interlaminar fracture toughness values used in these FE models were average values taken from the experimental measurements of the corresponding sample. In a new set of simulations, cohesive elements were used to simulate the interlaminar crack propagation behavior of the hybrid CFRPs to study the effect of different surface treatments on the CFRPs' interlaminar strength against crack propagation, as well as their ultimate crack opening. As a result of this set of simulations, it was seen that the hybrid CFRP based on uniform MWCNs grown fiber possessed 55% higher interlaminar strength compared to the reference CFRP based on raw fibers and via patterned growth of MWCNTs, the ultimate crack opening of the CFRPs improved by 20%. Due to the nature of woven CFRPs, unstable crack growth behavior was observed in the DCB experiments. In order to simulate this kind of crack propagation behavior, the fluctuations in the interlaminar fracture toughness values along the crack length were taken into account and another VCCT-based set of simulations were performed. This method was successful in capturing the mechanical behavior of the CFRPs obtained in the experiments.

Chapter 5. **A hybrid ZnO nanorod/carbon nanotube/carbon fiber reinforced polymer composite; synthesis, in-plane and out-of-plane mechanical characterization**

5.1 Overview

In the present investigation, a low-temperature hydrothermal synthesis technique is employed to grow zinc oxide (ZnO) nanorods on the surface of woven carbon fiber fabrics. Also, multi-walled carbon nanotubes (MWCNTs) are grafted on the surface of the carbon fiber fabrics and on top of the ZnO nanorods, utilizing a relatively low temperature synthesis technique. These two synthesis techniques expose the carbon fibers to various surface treatments; for the ZnO growth, the fibers undergo the following: sputter-coating with amorphous ZnO, solution-soaking, and ZnO nanorods growth. While the MWCNT growth entails exposure to elevated temperatures. Different fibers based on these surface treatments were prepared and their corresponding carbon fiber reinforced polymer composite (CFRP) laminates were fabricated. The in-plane mechanical performance of the different CFRPs was studied via tension tests. The dynamic out-of-plane energy dissipation capabilities of the CFRPs were examined utilizing high velocity (~90 m/s) impact tests. The CFRPs' impact progressive damage mechanism was also investigated employing quasi-static spherical punch tests. Scanning electron microscopy (SEM) was utilized for examining the quality and topology of the grown nano-reinforcements. Photography was utilized to probe the delamination area of the hybrid CFRPs after impact. Comparing the results of the hybrid MWCNT/ZnO nanorod/CFRP with those of reference CFRP undergone no surface treatment, 21% and 4% improvements were observed in impact energy absorption and tensile strain to failure of the CFRPs, respectively.

5.2 Introduction

Due to their outstanding in-plane strength and stiffness to-weight ratio, carbon fiber reinforced polymer composites (CFRPs) are replacing traditional structural materials. The excellent in-plane mechanical properties of CFRPs, as well as their ease of manufacturing made them suitable for numerous structural applications such as aerospace structures, automotive frames and civil infrastructures [2]. Despite their excellent mechanical properties along the fibers direction (on-axis), CFRPs lack sufficient off-axis and out-of-plane mechanical properties which makes them prone to interlaminar delamination. In order to grasp the implications of these deficiencies, studying the damage mechanisms occurring inside the CFRPs' structure under different loading scenarios is essential. When a CFRP laminate is subjected to an in-plane loading, various failure mechanisms would take place, i.e. cohesive matrix fracture, adhesive fiber/matrix interface debonding, and fibers fracture. While transversely loaded (e.g. impact), a complex mixture of different energy absorbing damage mechanisms such as matrix cracking caused by transverse shear, fiber fracture and kinking referred to as trans-laminar fracture, and delamination mainly caused by mode II shear fracture [4].

Although there are various methods for enhancing the CFRPs' weak out-of-plane performance, e.g. stitching [6], fiber surface treatment [7], and interleaving with toughened polymer [4,8], some of these methods induce damage to the carbon fibers and, therefore, deteriorate the in-plane mechanical properties of the entire CFRP [4]. Incorporating nano-sized reinforcement into the CFRPs' structures is a potential remedy for their inadequate out-of-plane performance [9]. Carbon nanotubes (CNTs) possess excellent physical, mechanical multifunctional properties, and extremely high aspect ratios [4]. Hence, a great body of research was devoted to investigating the effects of incorporating CNTs on the CFRPs' through-thickness and in-plane performance [4,9].

There are various routes to incorporate the CNTs into CFRPs' structure. The most straightforward route entails directly mixing the CNTs with the polymer matrix prior to the composites fabrication [9]; use a polymer matrix enriched with CNTs. This method was proven to enhance the toughness, stiffness and creep resistance of the polymer [10-12] and therefore, utilizing this mechanically enhanced polymer in the composites fabrication has improved the matrix dominated mechanical properties of the CFRP. For instance, in our previous work [86], via well-dispersing 2.0 wt.% of multiwalled CNTs (MWCNTs) into a polymer matrix of a CFRP, 21%, 26% and 12% improvements in its impact energy dissipation, vibration attenuation, and strain to failure were achieved, respectively. However, the inherent tendency of the CNTs to form agglomerates, and the excessive viscosity of the CNT-polymer mixture restrict this method from incorporating high CNTs concentrations into CFRPs [9]. Alternatively, in order to eliminate the problems associated with the CNT mixing method, grafting CNTs onto the carbon fibers surfaces could provide high concentration of CNTs where they are most needed, i.e. the immediate fiber/matrix interface, and in-between the different laminae of a CFRP [9]. The most utilized route to grow CNTs over carbon fibers is catalytic chemical vapor deposition (CCVD) [4,18-23]. Although some improvements were observed in the matrix dominated mechanical properties, e.g. interlaminar shear strength [18], significant degradations in the in-plane performance of the CFRPs were also reported [19,22,23]. This degradation is attributed to the relatively high temperatures (700-1200 °C) the CCVD requires, which damages the carbon fibers and therefore deteriorates the in-plane properties of the CFRPs. For example, a 40% drop in tensile strength of a hybrid CFRP was observed when growing CNTs on carbon fibers in a 700°C CCVD environment [19]. In contrast, employing the CCVD approach on the fibers more thermally resistant than carbon fibers (e.g. SiC fibers) [26], major improvements in mode I

interlaminar fracture toughness, flexural strength, flexural toughness, and damping capability were achieved.

In order to lessen the damages induced by the CCVD elevated temperatures, a relatively novel protocol for grafting the MWCNTs on carbon fibers has been proposed [27,28], which requires lower temperature (550 °C) than CCVD's. This method, referred to as graphitic structures by design (GSD), was utilized in a recent investigation by the authors [29] and no significant degradation in on-axis and off-axis tensile properties of the hybrid CFRP was observed when employing GSD to grow certain topologies of CNTs. Furthermore, optimally patterned growing the CNTs over the carbon fiber surfaces resulted in 11% and 19% enhancements in on- and off-axis tensile strength of the hybrid CFRPs, respectively [29]. The out-of-plane performance of hybrid CFRPs reinforced with GSD grown MWCNTs was also improved [22], e.g. 56% improvement in flexural loss modulus. In a more recent study [30], utilizing the GSD patterned growth of CNTs over carbon fibers yielded a 127% improvement of the impact energy dissipation of a CFRP.

Zinc oxide (ZnO) nanorods are other nano-sized reinforcing anisotropic structures which can hybridize the CFRPs. They can be radially grown on the surface of carbon fibers in order create hierarchical reinforcements [31,32]. Different methods have been used to synthesize ZnO nanostructures; vapor-phase transport [33], metalorganic chemical vapor deposition [34], sputtering [35], molecular beam epitaxy [36], thermal evaporation [37] and vapor-liquid-solid [38,91]. Most of these methods require elevated temperatures, and therefore could lead to the degradation of the carbon fibers resulting in reduced in-plane mechanical properties. Furthermore, some of the aforementioned methods follow complex procedures and require advanced equipment. Alternatively, hydrothermal synthesis, which is a solution-based low

temperature (70~90 °C) technique, can successfully grow ZnO nanorods radially on the carbon fibers. This method was employed to whiskerize the carbon fibers with ZnO nanorods [32] and more than 100% improvement in fiber/matrix interfacial shear strength was reported which proves the excellent enhancement in fiber/matrix adhesion which is a key factor in both in-plane and out-of-plane performance of the CFRPs. For example, in recent investigations [39,40], via hydrothermally growing ZnO nanorods on woven carbon fiber fabrics, flexural vibration attenuation, and stress relaxation modulus of a hybrid CFRP were improved by 50% and 65%, respectively. Utilizing identical synthesis technique, the interlaminar shear strength of a hybrid CFRP was also improved by 55% [41].

In general, high aspect ratio one-dimension nano reinforcements (e.g. ZnO nanorods and CNTs) offer large surfaces for frictional interactions inside the structure resulting in an increase the crashworthiness of the entire structure when the damage interacts with these nano-structures. Another energy dissipation mechanism that ZnO nanorods can benefit from is the coupling (and thus energy exchange) between the mechanical and electrical responses of the ZnO crystalline structure when mechanically loaded. ZnO nanorods possess piezoelectric and semiconductor properties making the hybrid CFRPs suitable for numerous applications, e.g. solar cells, sensors, structural health monitoring (SHM) and energy harvesting devices [42-45]. In a recent study [46], the hydrothermal ZnO synthesis was utilized to manufacture hybrid CFRP beams for energy harvesting applications.

In this study, a hydrothermal synthesis technique was utilized in order to grow ZnO nanorods onto the woven carbon fiber fabrics. The GSD method was also employed to graft the MWCNTs on top of the carbon fiber fabrics. MWCNTs were also grown on the surfaces of the ZnO nanorods utilizing the GSD method in order to make hybrid CNT-ZnO-carbon fiber

reinforcements. Field emission scanning electron microscopy (FE-SEM) was utilized to examine the quality of the grown nano-reinforcements. The consequences of the synthesis environment, i.e. exposure to water, amorphous pre-sputtered ZnO, as well as adding the different nano-reinforcements -separately and collectively- were investigated on light of the in-plane and out-of-plane mechanical performance of the CFRPs. The in-plane on-axis mechanical properties of the hybrid CFRPs were investigated via quasi-static tension tests. The dynamic out-of-plane properties of the hybrid CFRPs were tested utilizing high velocity (~90 m/s) impact tests. High speed imaging was utilized to measure the velocity of the impactor before and after perforating the composite laminates during the impact tests in order to calculate the impact energy absorption performance for the different hybrid CFRPs. The damage pattern and delamination severity were characterized using photography of the face and the cross section through the perforations of the damaged laminates, respectively. Furthermore, in order to clarify the impact damage mechanisms in the hybrid composite laminates, quasi-static spherical punch tests were implemented and analyzed for the different CFRP configurations.

5.3 Materials and Methods

For manufacturing the CFRP laminates, plain-woven Thornel® T650 PAN-based carbon fiber fabric was used as primary reinforcements. To remove the polymer sizing of the as-received fibers – so that the nano reinforcements attach better to the fiber, they were initially heated to 550 °C for 30 min under inert atmosphere (N_2). To further process the carbon fibers, square samples of 130 × 130 mm2 were cut from the de-sized fiber fabrics. As explained before, in order to grow ZnO nanorods onto the carbon fiber fabrics, a hydrothermal ZnO synthesis technique was performed which is explained in details elsewhere [39]. Prior to conduct the hydrothermal synthesis, an ATC Orion high vacuum sputtering system, by AJA international,

was utilized to deposit a 75 nm thick layer of amorphous ZnO on both sides of the de-sized fabrics. This pre-sputtered ZnO layer provides initiation seeds for the hydrothermally growing ZnO nanorod crystals on the surface of the carbon fibers. The synthesis technique utilizes an aquatic solution of zinc acetate dihydrate ($Zn(O_2CCH_3)_2$ $2H_2O$) and hexamethylenetetramine (HMTA) in deionized (DI) water using 30 mM concentrations of each chemical. In order to grow the ZnO nanorods, the pre-coated samples were immersed in the abovementioned solution and kept in a convection oven at 85 °C for 6 hours. For unraveling the effect of exposing the fabrics to hydrothermal environment, some ZnO pre-coated samples were soaked in DI water and heated up to 85 °C for 6 hours.

MWCNTs were also grown on identical de-sized carbon fibers. Depending on the samples configuration, they were grafted either on the amorphous ZnO pre-sputtered fabric samples or on the ZnO nanorods grown samples. The MWCNT growth process was performed following the GSD protocol explained elsewhere [27,28]. Prior to start the GSD process, a 2 nm thick layer of a catalyst metal (nickel) was deposited on both surfaces of the fabrics using the same magnetron sputtering system. The GSD CNT growth process was carried out inside a quartz tube reactor equipped with a thermal controller and three-input gas mass flow controllers. Briefly, the GSD process starts with a reduction step, under an H_2/N_2 gas mixture atmosphere at 550 °C for 2hr. Then, the process is followed by the flushing step in which the tube reactor is flushed with N_2 gas to get rid of any residuals of the previous process. Subsequently, the CNTs growth step begins, maintaining the constant temperature at 550 °C for 1hr under a $C_2H_4/H_2/N_2$ environment. In order to unravel the effect of GSD heat treatment and gas environment on the carbon fibers, some carbon fabric samples with no pre-coated nickel layer were exposed to identical heat-

treatment and gas mixtures as in the GSD process. Consequently, they didn't have any radially grown MWCNTs on their surfaces.

At the end of all the surface treatments and nano-reinforcement growths, 6 distinctive fiber samples' configurations were achieved. The samples designation and the process they underwent are listed in Table 5-1.

Table 5-1. Different designed sample configurations.

Label	**Treatment undergone**	**Grown nano-reinforcement**
R	As-received carbon fiber fabric	none
RD	De-sized fibers	none
WH	De-sized fibers, coated with amorphous ZnO, immersed in hot water, exposed to GSD procedure heat treatment.	none
WG	De-sized fibers, coated with amorphous ZnO, immersed in hot water, GSD method CNT growth.	MWCNTs over fibers
GH	De-sized fibers, coated with amorphous ZnO, hydrothermal ZnO nanorod growth, exposed to GSD procedure heat treatment.	ZnO nanorods over fibers
GG	De-sized fibers, coated with amorphous ZnO, hydrothermal ZnO nanorod growth, GSD method CNT growth.	MWCNTs over ZnO nanorods

In order to examine the quality of the grown nano-structures over the carbon fibers, a 5200 Hitachi FE-SEM electron microscope operating at 5 keV was used. The matrix used to form the designed hybrid CFRPs is Aeropoxy™, manufactured by PTM&W Industries Inc. that comprises a resin (PR2032), and a hardener (PH3665). The laminate fabricating was carried out utilizing a vacuum- and pressure-assisted hand layup system. Each composite laminate comprised 3 layers from the fabrics manufactured and listed in Table 5-1. The fabrics and composite laminates were

weighed before and after fabrication, respectively, and the fiber volume fractions were calculated. The fiber volume fractions of the fabricated CFRPs and the laminate thicknesses are listed in Table 5-2.

Table 5-2. Fiber volume fractions and thickness of different fabricated composite laminates

CFRP name	**R**	**RD**	**WH**	**WG**	**GH**	**GG**
V_f *(%)*	57.9	49.7	51.5	51.0	47.6	49.9
Thickness (mm)	0.76 ± 0.021	0.81 ± 0.025	0.80 ± 0.021	0.81 ± 0.022	0.86 ± 0.062	0.88 ± 0.024

For the tension tests, tensile coupons of 125.0 × 12.5 mm2 were cut from the fabricated panels. For the impact tests, panels of 130 × 130 mm2 were used, and for the spherical punch tests samples of 60.0 × 60.0 mm2 were cut from the composite panels. For each of the six fabric configurations, eight samples were tested in tension, four samples under impact and four samples for the spherical punch tests. The tensile tests were carried out following the ASTM-D3039/D3039M-08 standard, utilizing an Instron® 4400R testing frame under 1.0 mm/min constant crosshead speed. An MTS extensometer was coupled to the data acquisition system to record the strain. The stress vs. strain data for different test coupons were recorded and analyzed in order to report the samples' elastic modulus, ultimate strength and strain to failure. The high velocity impact tests were carried out utilizing an in-house designed one-stage gas gun [86,108] subjecting the composite panels to an 8.4 g steel spherical impactor with a 12.7 mm diameter with an average impact velocity of 88.25±2.12 m/s. A Photron® high-speed camera was used to capture the trajectory of the impactor, before and after the impact, at 30,000 frames per second speed. A MATLAB® image processing code was used to process the images captured by the camera in order to accurately measure the impactor speeds pre- and post- penetration.

Damage faces of the impacted samples were photographed for different sample configurations in order to compare the damage patterns of different configurations. Furthermore, the impacted samples were cut along the perforations zone and their cross-sections were photographed and the delamination lengths induced by the impact tests were measured. In order to examine how the differently designed CFRPs contribute to energy dissipation during impact loading, interlaminar regions of the impacted samples were also studied using the FE-SEM microscopy.

The quasi-static spherical punch tests were carried out using a hardened steel hemispherical punch with 12.7 mm diameter. The samples were clamped down to a rigid jig with a 20.0 mm diameter unclamped area open to the penetrator punch and the same Instron® testing frame coupled with a data acquisition system was used to record the punch force vs. penetration distance for the tests samples. The punch tests were carried out under a constant crosshead speed of 1.0 mm/min.

5.4 Results and Discussions

5.4.1 Scanning Electron Microscopy of the synthesized nano-reinforcements

The hydrothermally grown ZnO nanorods are shown in the SEM micrograph of Figure 5-1(a). The inset micrograph inside Figure 5-1(a) shows a magnification of a patch of ZnO nanorods forest which has been pulled off a carbon fiber; so it reveals the length of the grown ZnO nanorods. Figure 5-1(b) shows MWCNTs grown via the GSD method on a carbon fiber. Comparing the two nano-reinforcements, the ZnO nanorods were successfully grown as arrays of straight rods, whereas MWCNTs formed a wavy entangled network, nevertheless, both making hierarchical fibers suitable for manufacturing hybrid CFRPs. Figure 5-1(c) shows that the GSD

grown MWCNTs were also successfully grown on the ZnO nanorod. The inset image inside Figure 5-1(c) shows the curly MWCNTs grown over the straight ZnO nanorods.

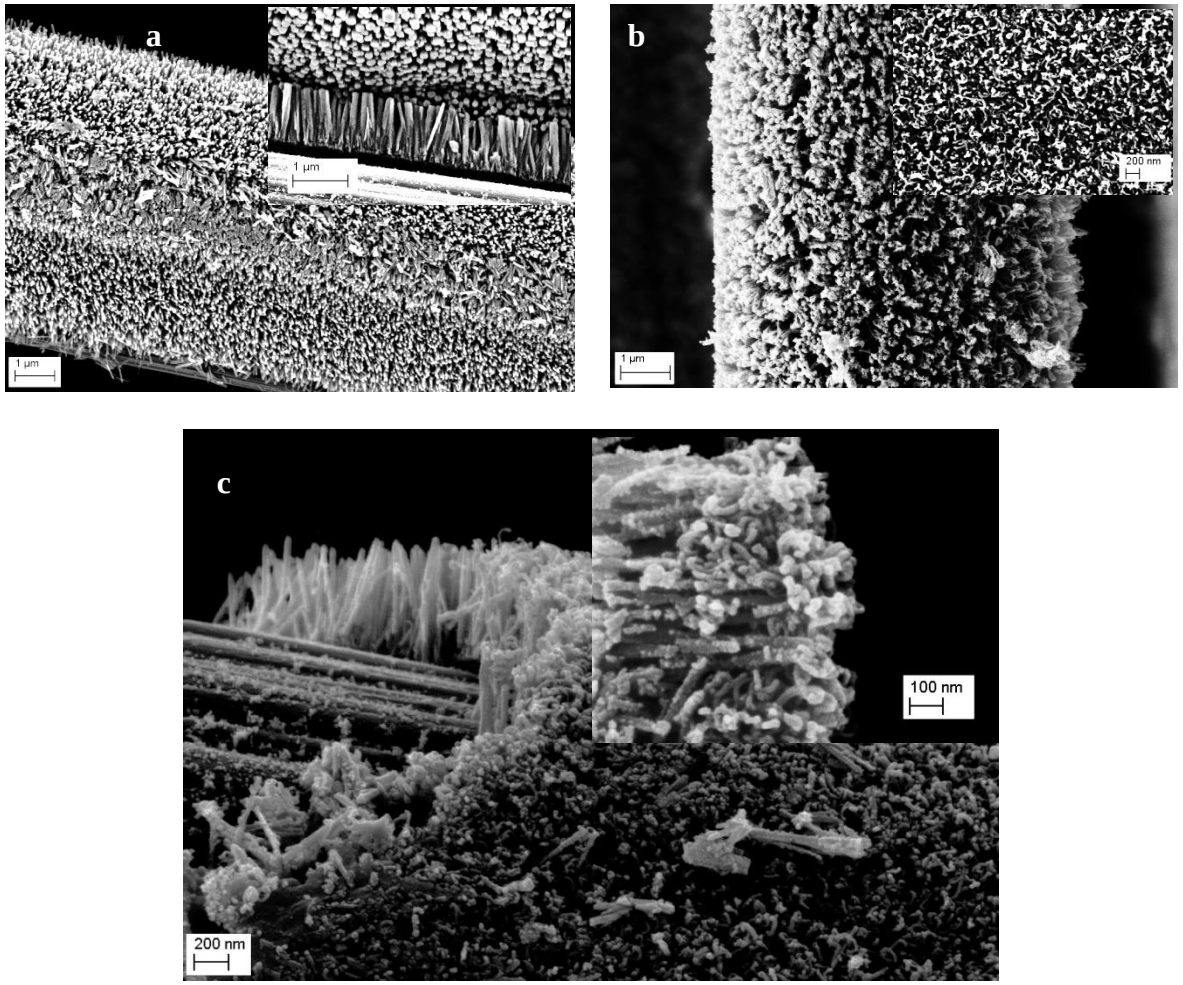

Figure 5-1. SEM micrographs of carbon fibers grafted with (a) ZnO nanorods; (b) GSD grown MWCNTs; (c) GSD grown MWCNTs over ZnO nanorods.

5.4.2 In-plane Tensile Performance of the Hybrid CFRPs

Figure 5-2 exemplifies representative stress-strain curves for the designed CFRPs. All six CFRP configuration tensile samples showed initial linear elastic behavior up to the strains around 0.4%. As the load increases, they deviate from linear behavior due to matrix cracking and individual fiber breakages. For the CFRP based on the as-received fibers (i.e. R sample), two significant

drops in the load can be observed which illustrates partial delamination occurred between the three laminae resulting in reduction in the load bearing ability. This might be due to week interlaminar region in this specific configuration. For the samples comprising nano-reinforcing materials (Figure 5-2(b)), reduction in the slope of the stress-strain curves, which implies stiffness reduction occurs gradually. This gradual descent in stiffness indicates a more ductile behavior in the hybrid CFRPs prior to their final failure. This could be attributed to better shear lagging capabilities stemming from better adhesion in the fiber/matrix interface and in the interlaminar region.

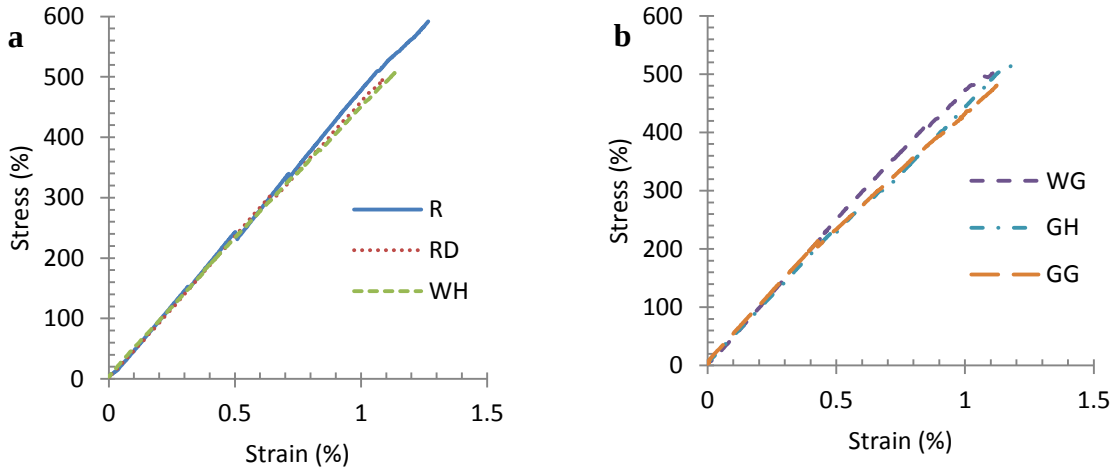

Figure 5-2. Representative stress-strain curves for (a) the CFRPs with no nano-reinforcements, i.e. CFRPs based on R (as-received), RD (de-sized), and WH (amorphous ZnO pre-coated, hydrothermal water immersed and GSD heat-treated) fibers; (b) Stress – strain curves for the CFPRs with nano-reinforcements, i.e. CFRPs based on WG (amorphous ZnO pre-coated, hydrothermal water immersed and GSD method CNT grown), GH (hydrothermally ZnO nanorods grown and GSD heat-treated), and GG (hydrothermally ZnO nanorods grown and GSD method CNT grown) fibers.

The slope of the stress-strain curves of the CFRPs up to the strain value of 0.30% was considered as their elastic moduli. The tensile strength of the designed CFRPs was considered to be the maximum stress value in the stress-strain data, and the strain to failure to be the strain value at

the last data point of the curves. Figure 5-3 reports the average values and the standard deviations for the CFRPs' (a) elastic modulus, (b) tensile strength, and (c) strain to failure.

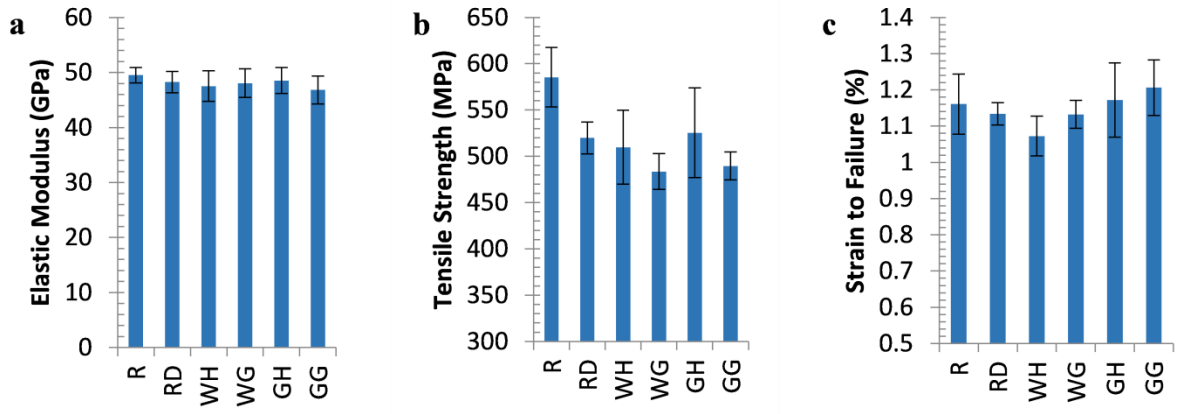

Figure 5-3. Average values of the (**a**) elastic modulus, (**b**) tensile strength, and (**c**) strain to failure, for the CFRPs based on R (as-received), RD (de-sized), and WH (amorphous ZnO pre-coated, hydrothermal water immersed and GSD heat-treated) WG (amorphous ZnO pre-coated, hydrothermal water immersed and GSD method CNT grown), GH (hydrothermally ZnO nanorods grown and GSD heat-treated), and GG (hydrothermally ZnO nanorods grown and GSD method CNT grown) fibers.

As shown in Figure 5-3(a), the elastic modulus of the CFRPs remains almost unchanged when the fiber underwent various surface treatments. It is due to the fact that the elastic modulus of the CFRPs along the fibers direction is mainly dominated by the carbon fibers' structures. Therefore, it can be inferred that the surface treatment performed on the carbon fibers did not damage the carbon fibers' cores. However, comparing the tensile strengths of the R and RD samples, an 11.1% reduction was observed. The heat-treatment associated with the de-sizing process could be the reason for this reduction in the CFRPs strength. Comparing the rest of the sample configurations with the reference sample (R), this reduction in strength is evident. Although the nano-reinforcing whiskers (MWCNTs and ZnO nanorods) grown on the surface of the carbon fiber fabrics couldn't compensate for this reduction in the tensile strength, they improved the

hybrid CFRPs to exhibit more ductile behavior and improved the strain to failure of the CFRPs by 4.5% in the case of the hybrid CFRP grown by both MWCNTs and ZnO nanorods. This is due to improving the adhesion in the fiber/matrix interface enhancing the stress transfer performance of the matrix around the fibers which is responsible for ductility of the CFRPs.

5.4.3 Out-of-plane high-velocity impact and quasi-static punch performance of the hybrid CFRPs

The high velocity impact tests were performed on the designed CFRPs and the velocity of the spherical impactor pre- and post- penetration was measured and the dissipated kinetic energies were calculated. The absorbed energies in the impact tests are shown in Figure 5-4(a). The quasi-static spherical punch tests were also carried out for all the sample configurations and the perforations force vs. cross-head displacements curves were obtained, shown in Figure 5-5. The require energy for penetrating the samples were calculated using integrating the area underneath the force vs. displacement curves of the Figure 5-5.

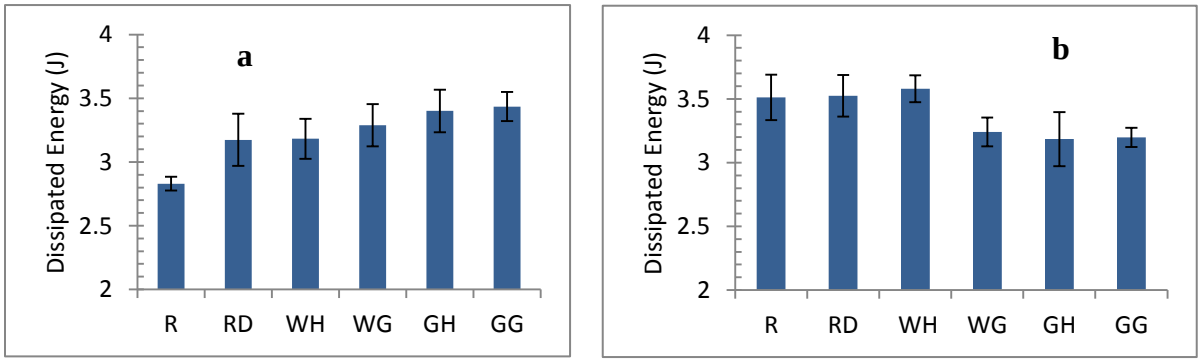

Figure 5-4. Dissipated energies for (**a**) high velocity impact; and (**b**) quasi-static spherical punch tests, for the CFRPs based on R (as-received), RD (de-sized), and WH (amorphous ZnO pre-coated, hydrothermal water immersed and GSD heat-treated) WG (amorphous ZnO pre-coated, hydrothermal water immersed and GSD method CNT grown), GH (hydrothermally ZnO nanorods grown and GSD heat-treated), and GG (hydrothermally ZnO nanorods grown and GSD method CNT grown) fibers.

These calculated energies are the dissipated energies during the quasi-static penetrating the samples using a spherical punch with identical geometry to the impactor ball in the impact tests. These energies are shown in Figure 5-4(b).

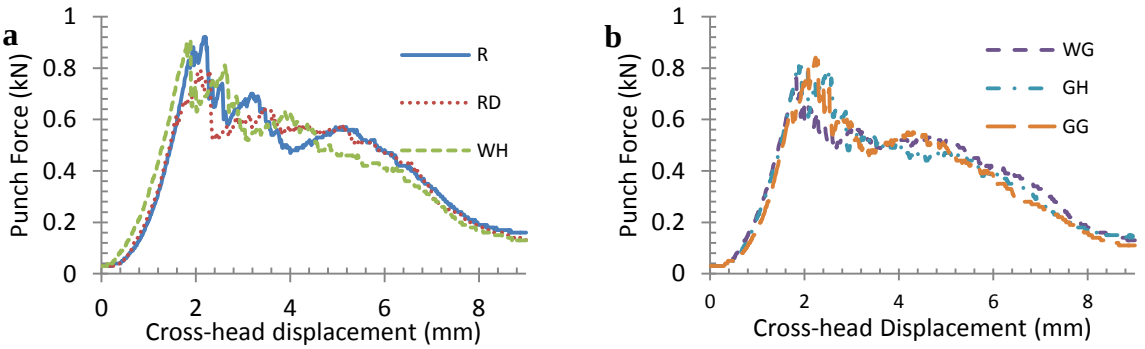

Figure 5-5. Representative punch force vs. cross-head displacement curves of the quasi-static spherical punch tests for (**a**) the CFRPs with no nano-reinforcements, i.e. CFRPs based on R (as-received), RD (de-sized), and WH (amorphous ZnO pre-coated, hydrothermal water immersed and GSD heat-treated) fibers; (**b**) the CFPRs with nano-reinforcements, i.e. CFRPs based on WG (amorphous ZnO pre-coated, hydrothermal water immersed and GSD method CNT grown), GH (hydrothermally ZnO nanorods grown and GSD heat-treated), and GG (hydrothermally ZnO nanorods grown and GSD method CNT grown) fibers.

Inferred from the dissipated impact energy data of Figure 5-4, the hybrid CFRPs with nano-reinforcing whiskers (WG, GH, and GG samples) dissipated more energies compared to the samples with no nano-reinforcements (R, RD, and WH samples). For example, the hybrid CFRP with both nano-reinforcing whiskers (GG sample) dissipated 21% more impact energy than the reference sample did. This is due to the fact that the hierarchical fibers in the interlaminar region could anchor better into the matrix resulting in higher interlaminar shear strength and, therefore, more energy dissipation during an impact loading. As shown in the force vs. displacement curves of Figure 5-5(a), the CFRPs with no nano-reinforcements exhibit three distinct load peaks, equivalent to the number of CFRP layers. This would confirm that theses CFRP laminates, due to lack of enough reinforcement in the interlaminar direction, firstly delaminated and then each

layer failed separately. In contrast, the force vs. displacement curves of Figure 5-5(b), which correspond to the hybrid CFRPs reinforced with MWCNTs (WG), ZnO nanorods (GH), both MWCNTs and ZnO nanorods (GG) showed smoother curves after the primary first peak, confirming less delamination damage than the CFRPs with no nano-reinforcements. These results were emphasized by the photographs of the side view of the perforated cross sections of the impacted samples (Figure 5-6).

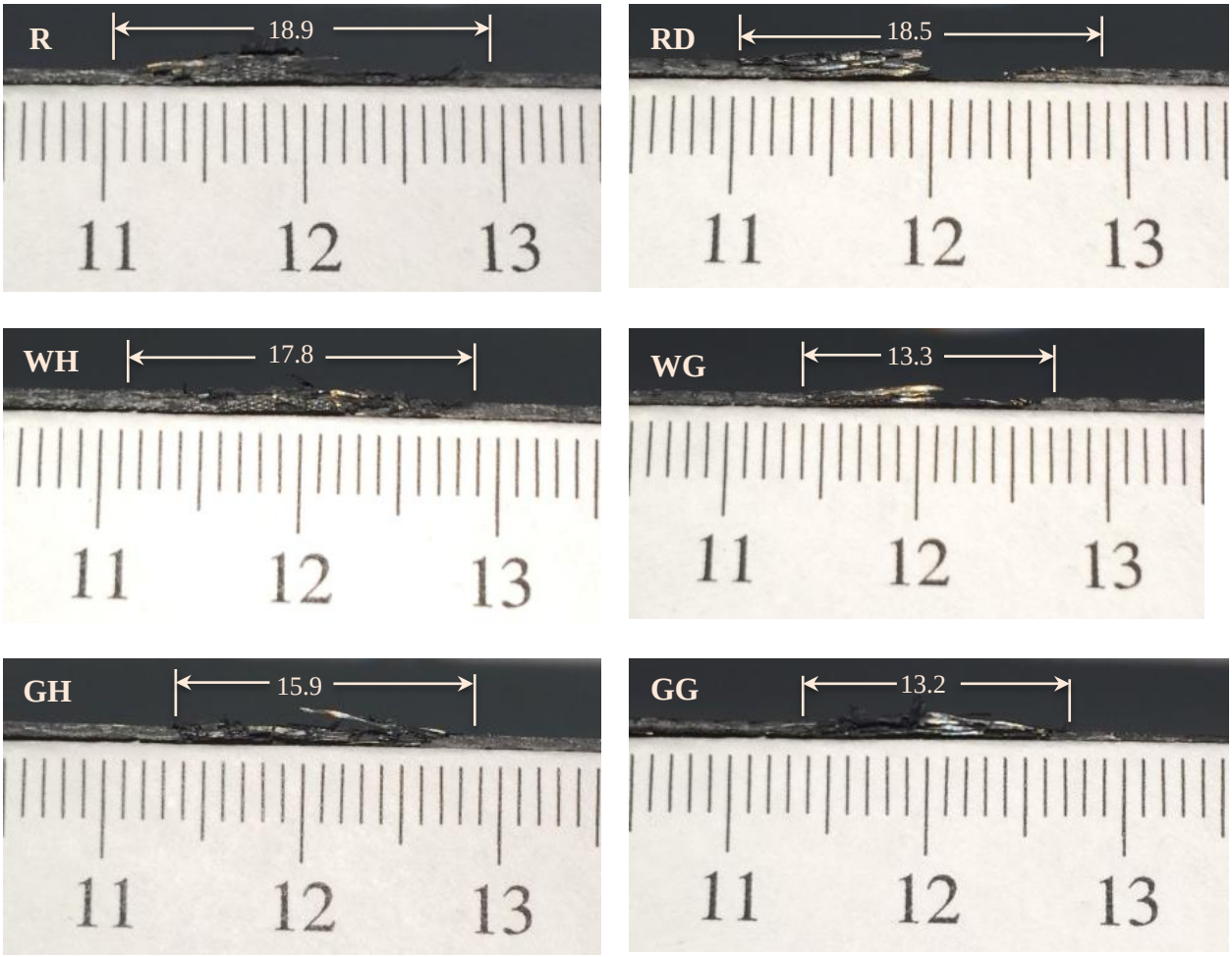

Figure 5-6. Delaminated cross sections of the impacted designed CFRPs based on R (as-received), RD (de-sized), and WH (amorphous ZnO pre-coated, hydrothermal water immersed and GSD heat-treated) WG (amorphous ZnO pre-coated, hydrothermal water immersed and GSD method CNT grown), GH (hydrothermally ZnO nanorods grown and GSD heat-treated), and GG (hydrothermally ZnO nanorods grown and GSD method CNT grown) fibers.

The delamination lengths were accurately measured and labeled on the images of Figure 5-6. The GG sample exhibited the least delamination length compared to the R sample; it showed 30% less delamination length after impact.

Referring to the energy dissipation results of Figure 5-4, it can be see that the hybrid CFRPs reinforced with the nano-whiskers (WG, GH, and GG samples dissipate comparable energies in impact (Figure 5-4(a)) and quasi-static punch (Figure 5-4(b)) tests. However, for the CFRPs lacking nano-whiskers (R, RD, and WH samples), the dissipated energies of quasi-static tests are much higher than those for the impact. It is well established [109] that, if both the dynamic impact and quasi-static punch tests share identical boundary conditions, they should dissipate almost same amount of energy. As seen in the delamination lengths of Figure 5-6, the delamination damages for the R, RD, and WH samples were very close to the diameter of the unclamped area of the jig used in the punch tests. For these specific samples configurations, as delamination reaches the boundaries of the unclamped area, the delaminated layers of the composite panels slip against one another and hence, more energy dissipates in the quasi-static punch tests than in impact.

In addition to delamination damage, matrix cracking and fiber breakage damages are two major energy dissipating damage mechanisms for a CFRP when subjected to an impact loading. Nano-sized whiskers in the fiber/matrix interface region are potential matrix crack stopping mechanisms, which can impede the matrix crack from propagating toward the fibers. On the other hand, improved fiber/matrix adhesion, resulted from the hierarchical structure of hybrid reinforcements, can improve the stress transfer capabilities of the matrix in the interphase region and therefore, make the composites behave more ductile and dissipate more energy. More ductility of the CFRPs hybridized with nano-reinforcements observed in tensile tests confirms

this conclusion. As a result of less ductility for the sample with no nano-reinforcement (e.g. R sample), the impacted panel started tearing apart before the CFRP deform and shape like the impactor. In other words, the impact damage pattern for the R sample (Figure 5-7(a)) is totally different than the one for GG sample (Figure 5-7(b)), where the pattern for the R sample is like a cross, while for the GG sample it is more circular.

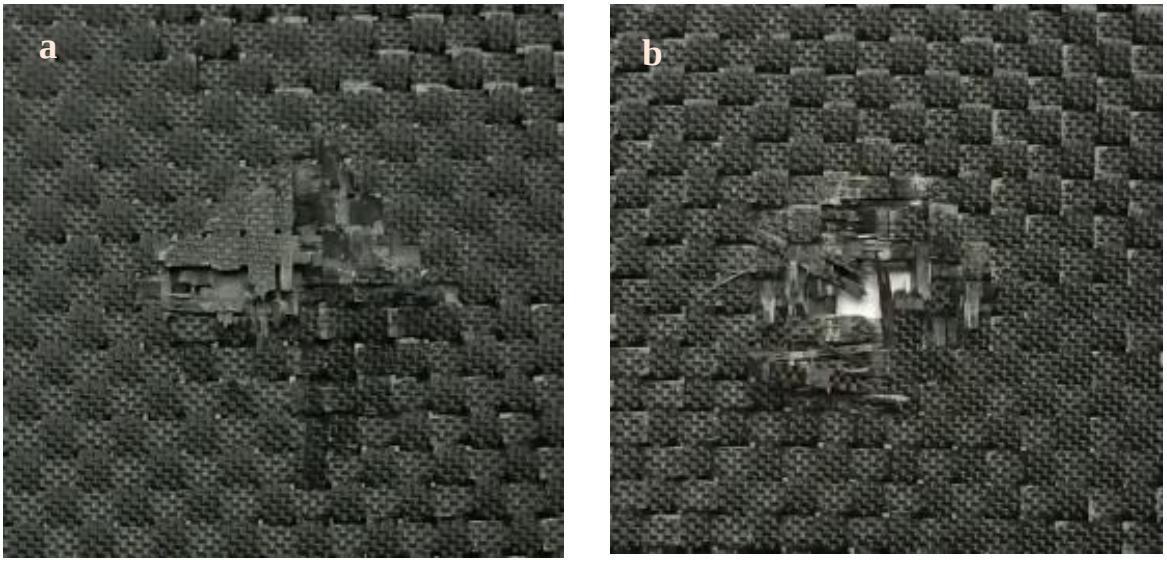

Figure 5-7. Impact damage patterns on the impacted CFRPs based on (**a**) R (as-received) and; (**b**) GG (hydrothermally ZnO nanorods grown and GSD method CNT grown) fibers.

In addition to the aforementioned damage mechanisms, another energy dissipating mechanism exclusive to the hybrid CFRPs are nano-whiskers pull out and breakage [4]. Such phenomena could be observed in Figure 5-8, SEM micrograph of the impacted GH sample, which is taken from the delamination area of the impacted hybrid CFRP nano-reinforced with ZnO (GH sample). In the figure the ZnO nanorods are observable in the image; they are broken and/or pulled out of the polymer matrix, indicating significant contribution to energy dissipation.

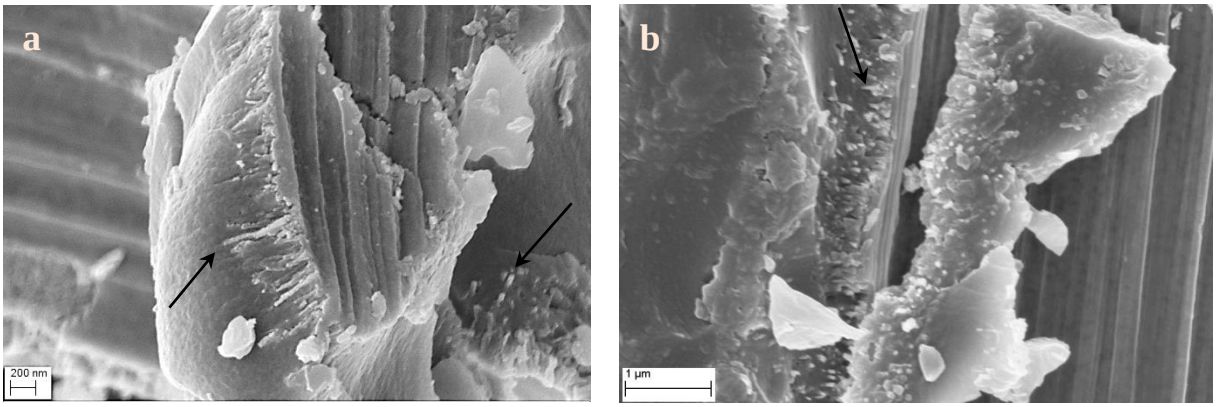

Figure 5-8. SEM micrographs of the delamination region in the hybrid CFRP reinforced with ZnO nanorods. Arrows point to observable nanorods in the images.

5.5 Conclusions

In the present work, a hydrothermal low temperature synthesis technique was employed to radially grow the ZnO nanorods onto the surface of woven carbon fiber fabrics. A relatively low temperature method, graphitic structure by design (GSD), was also utilized to grow multiwalled carbon nanotubes (MWCNTs) on top of the carbon fibers and/or ZnO nanorods. Scanning electron microscopy (SEM) was utilized to characterize the quality of the nano-reinforcements' growth. Carbon fiber reinforced polymer composites (CFRPs) based on carbon fibers with different surface treatments, associated with the two nano-reinforcements synthesis processes, were fabricated and their in-plane mechanical properties were investigated via quasi-static tensile tests. The out-of-plane performance of the different CFRPs was also studied utilizing high velocity impact tests. The impact energy dissipation capabilities of the hybrid CFRPs were measured and several impact damage progression mechanisms were investigated using the aid of quasi-static spherical punch testes. The delamination damages of different CFRPs were determined using photography of the cross section of the perforated samples. Although the in-plane tensile strength of the CFRPs dropped more than 10% due to exposing the fibers to the nano-reinforcements synthesis environments, the strain to failure of the hybrid CFRPs showed

some improvements through shear lagging capabilities of the improved fiber/matrix interface. Furthermore, via growing MWCNTs, ZnO nanorods, and MWCNT/ZnO nanorod nano-reinforcements over the carbon fiber fabrics, the dissipated impact energies of the CFRPs were improved 16%, 20%, and 21%, confirming the significant improvements in the delamination resistance of the hybrid CFRPs. These results were reinforced via measuring the delamination lengths of the impacted samples, where 30% less delamination zone was obtained in the CFRP hybridized by MWCNT/ZnO nanorod nano-reinforcing whiskers compared to the CFRP with no surface treatment.

Chapter 6. **Fatigue in hybrid carbon nanotubes/ZnO nanorods grafted carbon fiber reinforced polymer composites**

6.1 Overview

In this study, carbon fibers underwent two different nano-reinforcements synthesis techniques to produce hierarchical reinforcements; (a) graphitic structure by design (GSD) method was used to grow multi-walled carbon nanotubes (MWCNTs), and (b) hydrothermal technique was employed to grow zinc oxide (ZnO) nanorods over the carbon fibers. The carbon fibers with surface grown ZnO nanorods or CNTs were utilized to fabricate hybrid carbon fiber reinforced polymer composites (CFRPs). In order to unravel the effect of the different parameters encountered in the nano-reinforcement growth techniques (e.g., exposure to the GSD temperature, uniform or patterned CNT growth topologies, exposure to hydrothermal environment, and ZnO nanorods growth), carbon fibers underwent various surface treatments. Carbon fiber reinforced composite (CFRP) laminates were fabricated based on the different surface-treated fibers. The different CFRPs were examined under tensile loading to obtain their tensile strengths, as well as their elastic moduli and strain-to-failures. The surface grown CNTs promoted the tensile strength of the CFRPs by 12% and 19%, via uniform and checkerboard-patterned growth morphologies, respectively, over the carbon fiber fabrics. However, 6% reduction in the tensile strength of the CFRPs was observed via growing relatively long ZnO nanorods over the carbon fibers. The designed CFRPs were also tested under tension-tension fatigue to reveal the effects of the different nano-reinforcements growth on the fatigue behavior of the CFRPs. Stress-life (S-N) curves were obtained at stress levels of 85%, 90% and 95% of the CFRPs' tensile strength at the cycling stress ratio of 0.10. A remarkable fatigue damage tolerance was observed in the CFRPs

based on uniform and patterned grown CNT fibers. Almost two decades of fatigue life extension was achieved via CFRPs based on surface grown MWCNTs.

6.2 Introduction

Fiber reinforced polymer composites (FRPs) are relatively new structural materials with broad applications in aerospace, automotive, sport goods, etc. due to their high stiffness and strength to weight ratios [1,2]. FRPs should possess enough tolerance under not only monotonic loadings, but also under cyclic loadings to be qualified as alternatives to traditional structural metal alloys. Therefore, improving the fatigue life of FRPs is of great interest. It is well known that the fatigue life in FRPs is controlled mostly by the polymer matrix resistance to crack. The pre-fatigue cracks in the matrix will propagate and cause fibers' fracture, resulting in fatigue failure of the FRPs [70]. Comparing the two commonly used fibers in fabricating FRPs, i.e. glass and carbon fibers, carbon fibers exhibit higher stiffness than the glass fibers. Therefore, when the FRPs are under on-axis loadings, for identical levels of stresses in CFRPs and Glass FRPs (GFRPs) structure, GFRPs experience higher strains. This elevated strain, when present in a brittle polymer matrix, would initiate matrix cracks resulting in shortening the fatigue life of the GFRPs. Therefore, CFRPs are considered to be more resistant to on-axis high-cycle fatigue loading than GFRPs [70-72]. However, the presence of geometrical discontinuities, and in general, stress raisers, e.g. voids, holes, warp-weft cross-overs in woven fabrics, etc., would trigger matrix cracks causing the fatigue damage to initiate and progress. Avoiding all the aforementioned matrix crack initiators is almost unfeasible during the fabrication and use of CFRPs. Hence, improving the CFRPs' fatigue life using alternative routes need to be sought.

Almost all of the reported efforts focus on modifying the polymer matrix in order to achieve higher fracture toughness. High fracture toughness of the polymer matrix furnishes high

resistance to crack initiation and growth in the matrix, and therefore, improves the FRPs fatigue life. Utilizing nano-sized reinforcing additives into polymer matrix has been reported to have promising effects in improving their fracture toughness. For example, in a relatively recent study by Bortz et al. [73], well-dispersed graphene oxide nano-sheets improved the mode I fracture toughness of an epoxy by 28-110%. A significant improvement of 1580% in fatigue life of the nanocomposite was also observed. The graphene oxide nano-sheets' capabilities in pinning the fatigue cracks inside the polymer was the basis for this extended fatigue life. Despite the foreseen potential of incorporating the nano-sized reinforcements into the CFRPs structure, not many studies are reported on the fatigue behavior of hybrid CFRPs so far. Grimmer and Dharan [70] dispersed 1.0 wt.% of multi-walled carbon nanotubes (MWCNTs) into an epoxy matrix, and while there were no changes observed in the tensile strength of the GFRPs, significant improvement was observed in their tension-tension fatigue life. Davis et al. [74] utilized special CNTs in different weight percentages, in order to make hybrid CFRPs. They reported 1-2 orders of magnitude improvements in tension-tension fatigue life of the CFRP via incorporating 0.3 wt.% of fluorine XD-CNTs (industrial grade CNTs comprising a blend of SW- DW- and MW-CNTs). However, they reported no improvements in the fatigue life for lower CNTs contents of 0.2 wt.% or less, suggesting that this CNT content was not adequate for hindering the fatigue crack growth inside the matrix. In a recent investigation by Knoll et al. [75], incorporating 0.3 wt.% MWCNTs, improved the fatigue life of a hybrid CFRP by 5 folds. The well dispersion of the nano-reinforcements is crucial in improving the fatigue performance of the hybrid FRPs. For example, in a recent study [76], incorporating 0.5 wt.% MWCNTs showed no improvement, while adding 1.0 wt.% MWCNTs led to significant degradation in the fatigue life of a hybrid GFRP. In general, utilizing high content of nano-fillers can be severely limited by the difficulty

of dispersing them into polymeric matrices [15]. For example, the inherent tendency of CNTs to agglomerate limits their viable mixing weight percent to less than 3.0 wt.% [22,87]. The CNTs agglomerates disprove the mechanical performance of the host matrix, as they provide possible stress concentration sites inside the host material. In addition, mixing a minute weight percent of CNTs into a polymeric matrix dramatically increases the polymer's viscosity preventing the matrix from defusing in-between the fibers during the composite fabrication process [9].

Alternatively, in order to avoid the dispersion problems associated with the mixing methods, nanostructures can be grown over the surface of fibers prefabricating the composites. This approach produces hybrid hierarchical reinforcements, potentially capable of providing the composites with a stronger fiber/matrix interface. In addition, the existence of the nanostructures in the vicinity of the fibers can contribute to hinder the matrix cracks from propagating into the fibers. However, some growth methods could be destructive to the fibers, resulting in poor in-plane mechanical performance of the hybrid FRPs. As an example, chemical vapor deposition (CVD) is the most common approach to grow CNTs, which requires relatively high temperatures (700-1100 °C). Although great improvements in the interlaminar fracture toughness of the CVD-CNT grown hybrid FRPs have been reported in the literature [26,87,96], this temperature range imposes destructive effects on the in-plane mechanical performance of the FRPs; both glass and carbon fibers are sensitive to these elevated temperatures [19,22]. An alternative method to CVD is graphitic structures by design (GSD), which utilizes relatively low temperatures (550 °C) [27,28], has been reported to improve the in-plane and out-of-plane mechanical performance of carbon fiber reinforced polymer composites (CFRPs) [22,29,30]. The simplicity of the equipment and nontoxicity of the gases utilized in the GSD technique are among the advantages of this method over the CVD method. In addition, the GSD technique enables the growth of CNT

frosts in various patterns and topologies over the fibers, as CNTs would grow where the catalyst metal is pre-deposited. This capability was utilized previously [29,30] to promote the benefits of the CNT growth simultaneously for both the in-plane and the out-of-plane performance of the CFRPs. However, GSD still moderately induces damage to the in-plane mechanical performance of FRPs based on glass fibers (GFRPs) [88].

In lieu to CNTs, zinc oxide (ZnO) nanorods can be grown over fibers to produce hybrid reinforcements [31,32]. In addition to the mechanical benefits, ZnO is a semi-conductive and piezoelectric material. These unique characteristics of ZnO facilitate their application in energy harvesting and structural health monitoring of the hybrid FRPs [46,89,90]. There are several techniques to synthesize ZnO nanorods; vapor-phase transport [33], metalorganic chemical vapor deposition [34], sputtering [35], molecular beam epitaxy [36], thermal evaporation [37] and vapor-liquid-solid [38,91]. Most of these methods employ elevated temperatures, which are destructive to carbon fibers, and require complex synthesis setup. Alternatively, hydrothermal synthesis is a low temperature (~90 °C) solution-based technique, capable of successfully growing ZnO nanorods over carbon fibers [31,32]. Employing this technique yielded improvements in fiber/matrix interface shear strength [32], interlaminar shear strength [41], vibrations attenuation [39,41], in-plane on-axis and off-axis tensile strengths [41,92], creep behavior [40] and high-velocity impact energy dissipation [92] of CFRPs.

In the present work, the GSD and the hydrothermal synthesis techniques were employed to grow multiwalled CNTs (MWCNTs) and ZnO nanorods, respectively, over woven carbon fiber fabrics. In order to unravel the effect of different parameters included in the nano-reinforcement growth techniques (exposure to the GSD temperature, uniform or patterned CNT growth topologies, exposure to hydrothermal environment, and ZnO nanorods growth), carbon fibers

underwent various surface treatments. Field emission scanning electron microscopy (FE-SEM) was utilized to examine the quality of the grown nano-reinforcements. Composites based on these carbon fibers were fabricated. The designed hybrid CFRPs were examined in tension tests, to obtain their tensile strengths, as well as their elastic moduli and strain-to-failures. The CFRPs then tested in tension-tension fatigue experiments to see the effect of nano-reinforcements growth on the fatigue behavior of the CFRPs. Stress-Life (S-N) curves were obtained at stress levels of 85%, 90% and 95% of the CFRPs' tensile strength at the cycling stress ratio of 0.10. Fractographs were taken using the FE-SEM to scan the fracture surfaces of the CFRPs with different configurations after fatigue failure, in order to understand the fatigue damage mechanisms in the designed CRRPs and the role of surface grown nano-reinforcements to resist against these mechanisms.

6.3 Materials and methods

6.3.1 Preparing the fibers for nano-reinforcement synthesis procedures

Un-sized plain-woven SGP196 (IM7-GP, provided by Hexcel Inc.) carbon fiber fabric (6 K filaments count in a tow) was used as the main reinforcements. Square samples of 130 × 130 mm^2 were cut from the fiber fabrics along the warp and weft directions to perform the desired surface treatments.

The GSD MWCNTs synthesis technique requires pre-deposition of a catalyst meal (i.e. nickel in this study) on the surface of the carbon fibers. The CNTs growth initiates from the area where the catalyst material is pre-deposited. For growing uniform CNTs forests over the carbon fiber fabrics, a uniform layer of nickel was needed. An ATC Orion (AJA international, Inc.) high vacuum sputtering system was utilized to deposit a 2 nm thick layer of nickel on both sides of the

square fabric samples under 3 mTorr pressure of argon gas where 200 W of power was supplied to the sputtering target. To achieve a checkerboard patterned CNTs forest over the carbon fiber fabrics, a perforated mesh template with a thread size of 76 μm and an opening edge size of 140 μm, was clamped on the fabrics prior to depositing the nickel layer.

Hydrothermal ZnO nanorods synthesis technique requires a pre-deposited ZnO layer over the carbon fibers to provide a substrate possessing a similar crystalline structure as ZnO nanorods have to initiate the growth process. The same magnetron sputtering system used in the aforementioned nickel sputtering was utilized here, supplied by 140 W of power, to deposit a 75 nm thick layer of amorphous ZnO on both sides of the square carbon fiber fabric samples.

6.3.2 MWCNTs synthesis by GSD technique

The MWCNTs growth process was performed following the GSD protocol explained elsewhere [27,28]. The GSD CNTs growth process was carried out inside a quartz tube reactor equipped with a thermal controller and three-input gas mass flow controllers. Briefly, the GSD process starts with a reduction step, under an H_2/N_2 gas mixture atmosphere at 550 °C for 2hr. Then, the process is followed by the flushing step in which the tube reactor is flushed with N_2 gas to get rid of any residuals of the previous step. Subsequently, the CNTs growth step begins, maintaining the constant temperature at 550 °C for 1hr under a $C_2H_4/H_2/N_2$ environment. In order to unravel the effect of GSD heat treatment and gas environment on the carbon fibers, some samples with no pre-coated nickel layer were exposed to identical heat-treatment and gas mixtures as in the GSD process. Consequently, they didn't possess any radially grown MWCNTs on their surfaces.

6.3.3 ZnO nanorods synthesis by hydrothermal technique

To grow ZnO nanorods over the carbon fiber fabrics, a hydrothermal ZnO synthesis technique was performed which is thoroughly explained elsewhere [39]. As explained earlier, prior to conduct the hydrothermal synthesis, a 75 nm thick layer of amorphous ZnO was deposited on both sides of the de-sized fabrics. This pre-sputtered ZnO layer provides initiation seeds for the hydrothermally growing ZnO nanorod crystals on the surface of the carbon fibers. The synthesis technique utilizes an aquatic solution of zinc acetate dihydrate ($Zn(O_2CCH_3)_2.2H_2O$) and hexamethylenetetramine (HMTA) in deionized (DI) water using 30 mM concentrations of each chemical. In order to grow the ZnO nanorods, the pro-coated samples were immersed in the abovementioned solution and kept in a convection oven at 85 °C for 8 hours. To unravel the effects of exposing the fabrics to the hydrothermal environment, some ZnO pre-coated samples were soaked in DI water and heated up to 85 °C for 8 hours. After completion of the synthesis process, the fibers were rinsed using DI water and dried overnight in the same oven at 85 °C.

6.3.4 Sample configurations and composite laminates fabrication

After all the different surface treatments on the carbon fibers, six distinctive sample configurations were achieved, which their designation and the process they underwent are listed in Table 3-1. The composite fabrication was carried out utilizing a vacuum- and pressure-assisted hand layup system. Aeropoxy™ (PTM&W Industries, Inc.) that comprises a resin (PR2032), and a hardener (PH3665) was used as the polymer matrix in order to fabricate the designed hybrid CFRPs. The composite laminates comprised 3 layers from the fabrics listed in Table 3-1.

Table 6-1. Different designed sample configurations		
Label	***Treatment undergone***	**Nano-reinforcements grown**
R	*As-received carbon fiber fabric (reference)*	none
H	*Reference, exposed to the heat treatment and gas environment of GSD method*	none
UG	*Reference, pre-coated with a uniform nickel layer, MWCNT growth by GSD method*	Uniform MWCNTs forest
PG	*Reference, pre-coated with a patterned nickel layer, MWCNT growth by GSD method*	Patterned MWCNTs forest
W	*Reference, pre-coated with uniform ZnO layer, exposed to hot water*	none
Z	*Reference, pre-coated with uniform ZnO layer, hydrothermal ZnO nanorods growth*	ZnO nanorods

The fabrics and composite laminates were weighed before and after fabrication, and knowing the density of the carbon fibers and matrix epoxy, the fiber volume fractions were calculated. Table 3-2 lists the fiber volume fractions of different composite laminates.

Table 6-2. Fiber volume fractions of composite laminates						
CFRP label	R	H	UG	PG	W	Z
V^f (%)	57.7±1.4	58.6±1.5	55.0±1.4	57.0±1.5	58.1±0.7	56.4±0.3

6.3.5 Characterization

In order to examine the quality of the grown nano-structures, either MWCNTs or ZnO nanorods, over the carbon fibers, a 5200 Hitachi FE-SEM electron microscope operating at 5 kV was used. Considering the difficulty of contrasting the topology of the MWCNTs forest patches grown in a checkerboard pattern over a cylindrical fiber surface, the GSD synthesis technique was carried out on a flat silicon wafer substrate, sputtered with a patterned nickel catalyst layer, and SEM

was performed on this sample. For the tension tests, tensile coupons of 125.0 × 12.5 mm^2, were cut from the fabricated composite panels. The tensile tests were carried out following the ASTM-D3039/D3039M-08 standard [94], utilizing an Instron® 4400R testing frame under 1.0 mm/min constant crosshead speed. An MTS extensometer was used to record the strain. The stress vs. strain data for different test coupons were recorded and analyzed to report the samples' elastic modulus, ultimate strength and strain to failure.

Tension-tension fatigue tests were performed for all the samples using an MTS hydraulic testing frame at loading frequency of 7.0Hz under a maximum to minimum stress ratio of 0.10 at three different maximum stress levels of 85.0%, 90.0%, and 95.0% of the corresponding samples' monotonic tensile strengths. The fatigue tests were performed following the ASTM D3479/D3479M−12 standard [110]. The number of cycles and the values of peaks and valleys for load and displacement at each loading cycle were recorded. The cyclic loading was continued until the final fracture of the specimens occurred. However, the tests were stopped when the number of cycles exceeds 1 million. The stress vs. life-cycles (S-N) curves were obtained for all the tested composite configurations according to ASTM Standard practice E739-10 [111]. According to the standard, 95% confidence bands were also created and introduced into the S-N curves.

Relative reduction in the CFRPs' stiffness over their life-time, so-called damage factor, was also calculated as in Equation (6.1)

$$DF = \frac{E_0 - E_N}{E_0} \tag{6.1}$$

Where, E_0 is the initial stiffness of the sample, E_N is the stiffness after N complete load cycles, and DF is the fatigue damage factor. The damage factor can change from 0.0 to 1.0 as the fatigue damage propagates inside the material and causes the CFRPs to lose stiffness.

6.4 Results and discussion

6.4.1 Scanning electron microscopy of the synthesized nano-reinforcements

The MWCNTs grown over the carbon fibers utilizing the GSD method are shown in micrographs of Figure 3-4(a). The inset picture is a magnified micrograph of the grown MWCNTs showing that the MWCNTs have ~20 nm diameters and wavy shapes. Figure 3-4 (b) shows the checkerboard pattern growth of CNT patches over a silicon wafer. The same pattern was used in preparing the PG sample configuration. The hydrothermally ZnO nanorods grown over the carbon fibers are shown in micrographs of Figure 3-5. The magnified inset micrograph in Figure 3-5(a), as well as Figure 3-5(b) show the nanorods possess ~2.0 μm length and ~20.0-100.0 nm diameter.

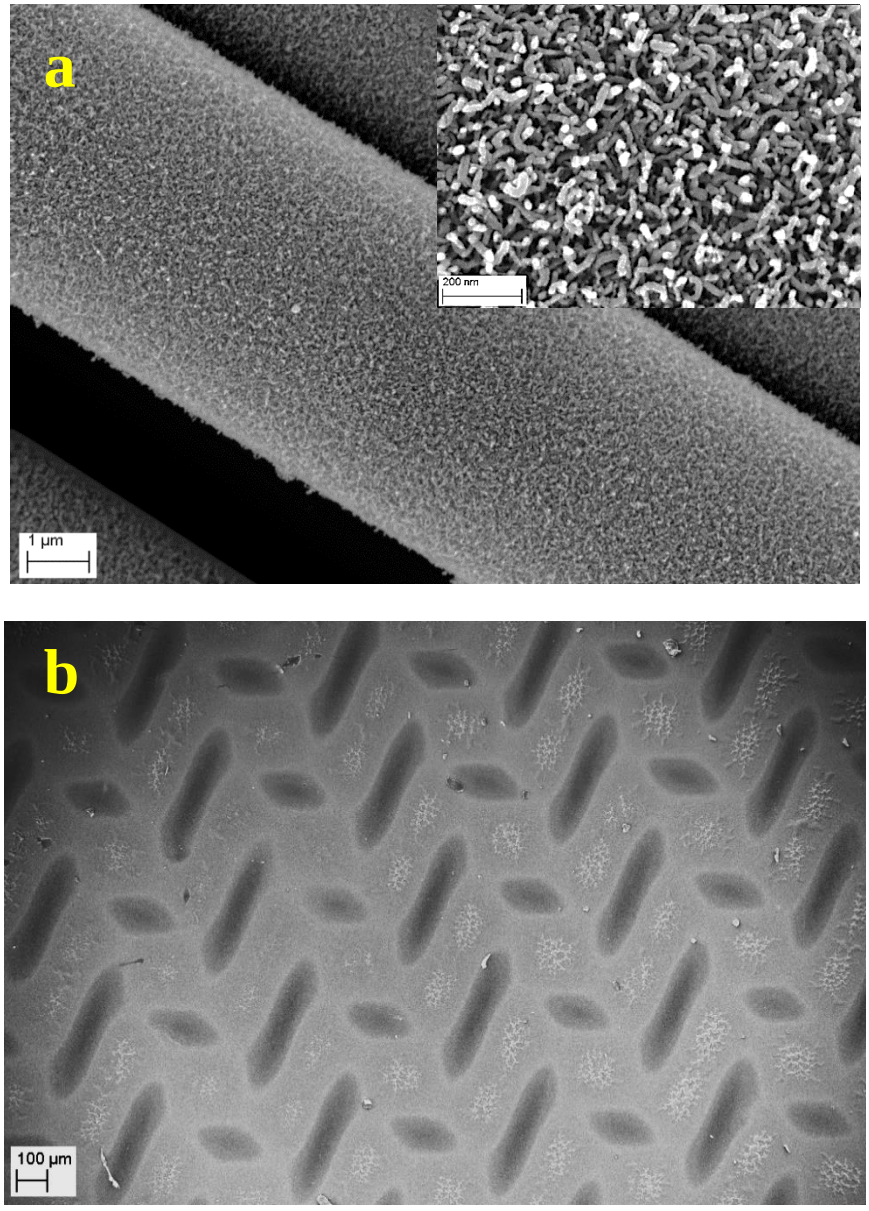

Figure 6-1. Scanning electron microscopy (SEM) micrographs of (a) GSD grown MWCNTs over carbon fibers in two different magnifications, and (b) MWCNT patches grown in a checkerboard pattern over a silicon wafer. Shining spots are MWCNT patches.

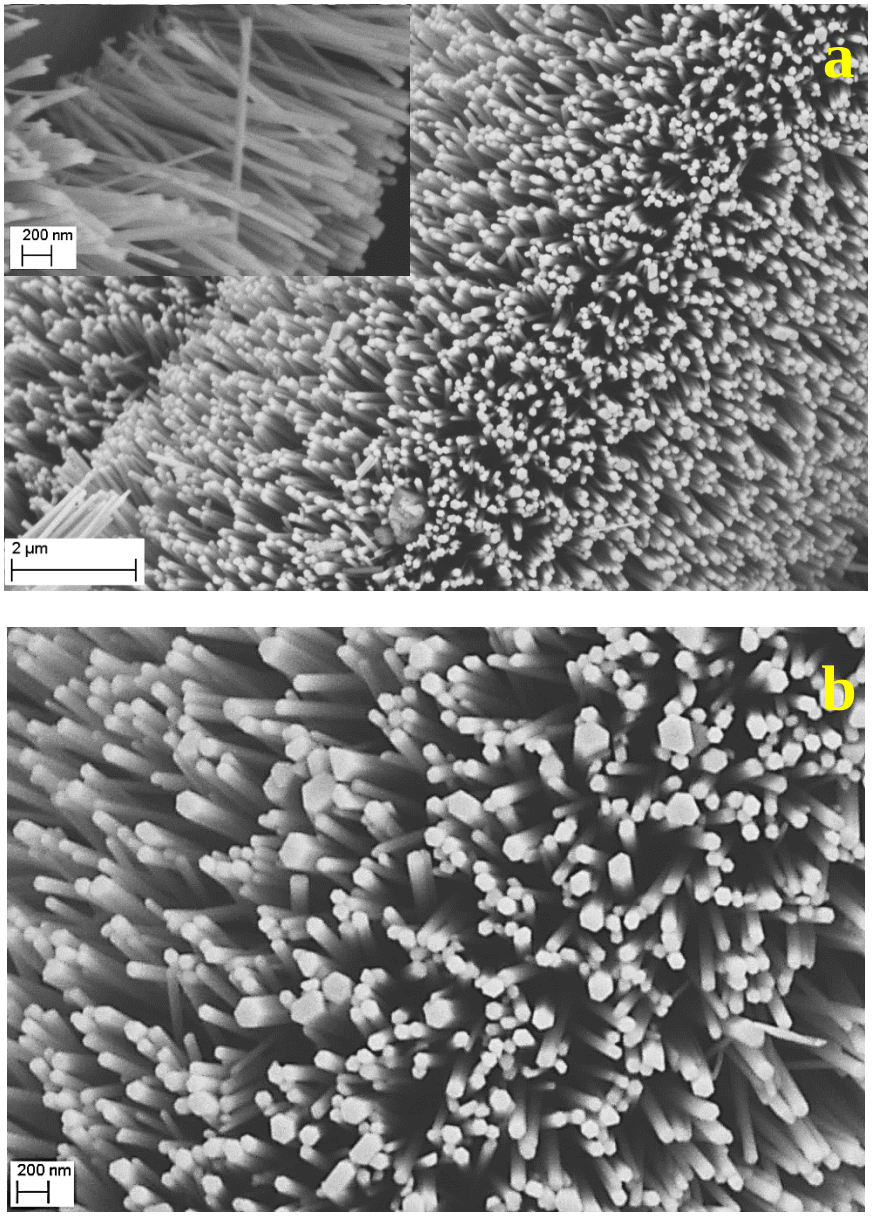

Figure 6-2. Scanning electron microscopy (SEM) micrographs of ZnO nanorods grown over carbon fibers, (a) the overall growth over a carbon fiber, the insert is higher magnification to estimate the nanorods' lengths, and (b) a magnified view to estimate the nanorods' diameters.

6.4.2 In-plane tensile performance of the hybrid CFRPs

Representative stress vs. strain curves for the designed CFRPs, obtained from the tension tests, are illustrated in Figure 3-6. Figure 6-4 reports the average values and the standard deviations for the CFRPs' (a) elastic modulus, (b) tensile strength, and (c) strain to failure. The slope of the

stress vs. strain curves of the CFRPs up to the strain value of 0.30% was considered as their elastic moduli. The tensile strength of the designed CFRPs was considered to be the maximum stress value in the stress vs. strain data, and the strain to failure to be the strain value at the last data point of the curves.

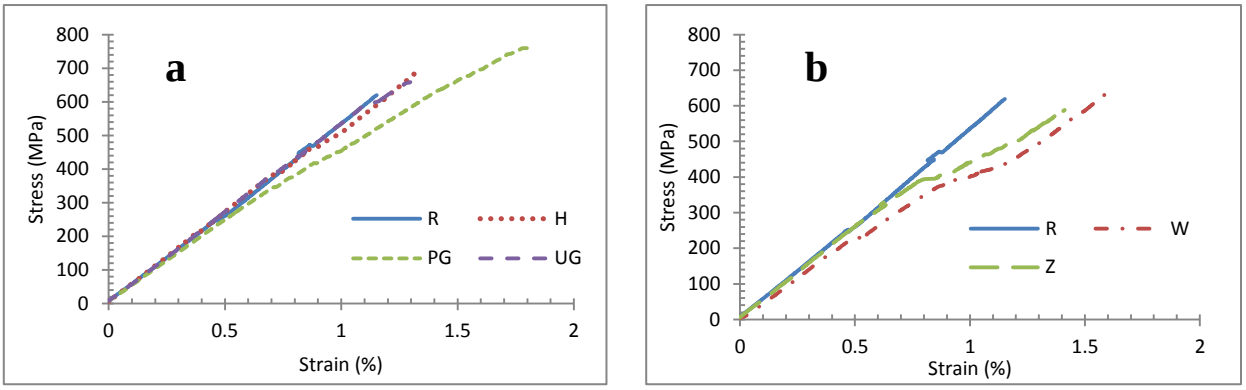

Figure 6-3. Representative stress vs. strain curves for the designed hybrid CFRPs based on (a) reference (R), heat-treated (H), patterned GSD grown MWCNTs (PG), and uniform GSD grown MWCNTs (UG) fibers, and (b) reference (R), hot-water exposed (W), and ZnO nanorods grown (Z) fibers.

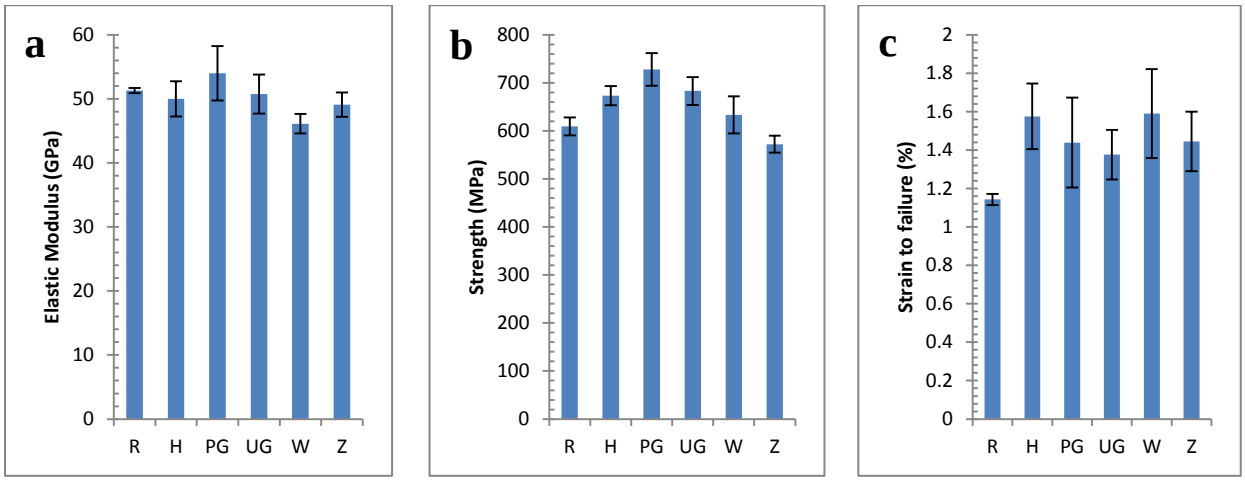

Figure 6-4. Average values of the (a) elastic modulus, (b) tensile strength, and (c) strain to failure, for the CFRPs based on reference (R), heat-treated (H), patterned GSD grown MWCNTs (PG), uniform GSD grown MWCNTs (UG), hot-water exposed (W), and ZnO nanorods grown (Z) fibers.

Figure 3-6 shows that all the CFRPs exhibited an initial linear-elastic behavior up to the strains around 0.4%. However, as the load increased their behavior delineated from linearity due to initiation of matrix cracking and some individual fiber breakages. The elastic modulus of the CFRPs mostly depends on the stiffness of the fibers. Therefore, surface treatments on the fibers should not affect the CFRPs stiffness unless they are damaged by the procedures. Inferred from Figure 6-4(a), it was seen that for most of the CFRPs configurations the elastic modulus remained unchanged except for the samples exposed to water (e.g. W and Z samples). Although the fibers were dried in an oven overnight after exposing to the hydrothermal environment, small amount of remaining moisture has caused a drop in the CFRPs stiffness.

As load increases, the cracks in the matrix could propagate towards the fibers, increasing the stress intensity close to the fibers, causing fiber breakages, unless the crack is stopped or deflected by the nano-reinforcements forests in the fiber/matrix interface region. In the case of individual fiber breakages, the stress transfer mechanism through the matrix in the fiber/matrix interface region aids the composite to withstand the load. The nano-reinforcements grown over the carbon fibers provide relatively stronger fiber/matrix interface potentially beneficial to the CFRPs strength and strain to failure. From the results of Figure 6-4(c) it was observed that all the CFRPs comprising surface grown nano-reinforcements exhibited improvements in the strain to failure compared to the reference CFRPs'. Via uniform and patterned growth of the GSD MWCNTs over the carbon fibers, 20% and 26% improvements were observed, respectively, in the strain to failure of the reference CFRPs. The CFRPs based on heat treated fibers (H) also showed an outstanding improvement in the strain to failure (37%) which can be attributed to the improvements in the fiber/matrix interface provided by small amount of the fibers oxidation during the heat treatment process. However, the CFRPs based on H fibers lacked nano

reinforcement and therefore were unable to block the matrix cracks propagating towards the fibers. Hence, while the CFRPs based on the UG and PG fibers exhibited 13% and 20% increase in the tensile strength of reference CFRPs, the CFRPs based on H fibers increased the tensile strength by only 10%. These results are in agreement with our previously published investigation [29].

The matrix cracks initiated in the interlaminar region can propagate in between the plies inducing delamination damage areas. The existence of the nano-reinforcements in the interlaminar region can block the crack from propagating. However, the cohesion between the fibers and the grown nano-reinforcement is a key to determine the resistance of the CFRPs to delamination damage. The CFRPs based on W and Z fibers illustrated large areas of delamination damage in the tension tests. The significant drops in their stiffness (i.e. the slope stress-strain curves of Figure 3-6(b)) were due to quick propagation of delamination damage. Figure 6-5 shows the examples of the fractured samples after monotonic tension tests. While almost no visual delamination damage was detected for the reference (R) and patterned GSD-MWCNTs grown (PG) fibers (shown in Figure 6-5(a) and (b) respectively), large delamination damages were observed for the water-exposed (W) and ZnO nanorod grown (Z) fibers (shown in Figure 6-5(c) and (d) respectively).

The insubstantial delamination damage resistance of the abovementioned CFRPs was the reason they exhibited no improvement in the tensile strength of the reference CFRPs.

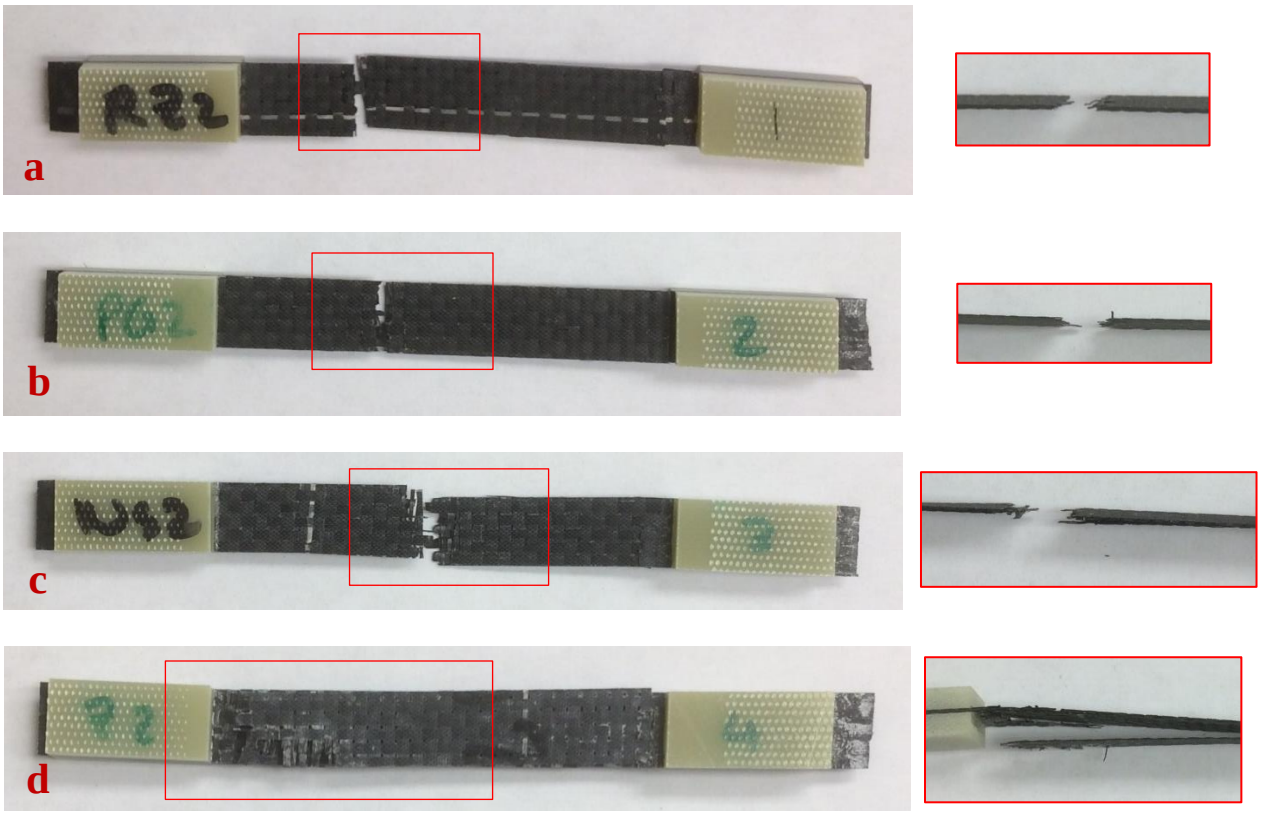

Figure 6-5. Fractured samples after quasi static tension tests for the CFRPs based on (a) reference (R), (b) patterned GSD grown MWCNTs (PG), (c) hot-water exposed (W), and (d) ZnO nanorods grown (Z) fibers. The side-views of the fractured faces are shown on the right.

6.4.3 Effect of GSD-MWCNT growth on CFRPs' fatigue performance

The fatigue tests were performed on the CFRPs based on reference (R), uniform MWCNT grown (UG) and patterned MWCNT grown (PG) fibers. Figure 6-6 shows the resulted S-N curves. In Figure 6-6(a), the stresses are presented as a portion of the corresponding CFRPs' ultimate tensile strength. The overrun data points are indicated with small arrows next to them. The 95% confidence bands for the measured stress ranges are also included.

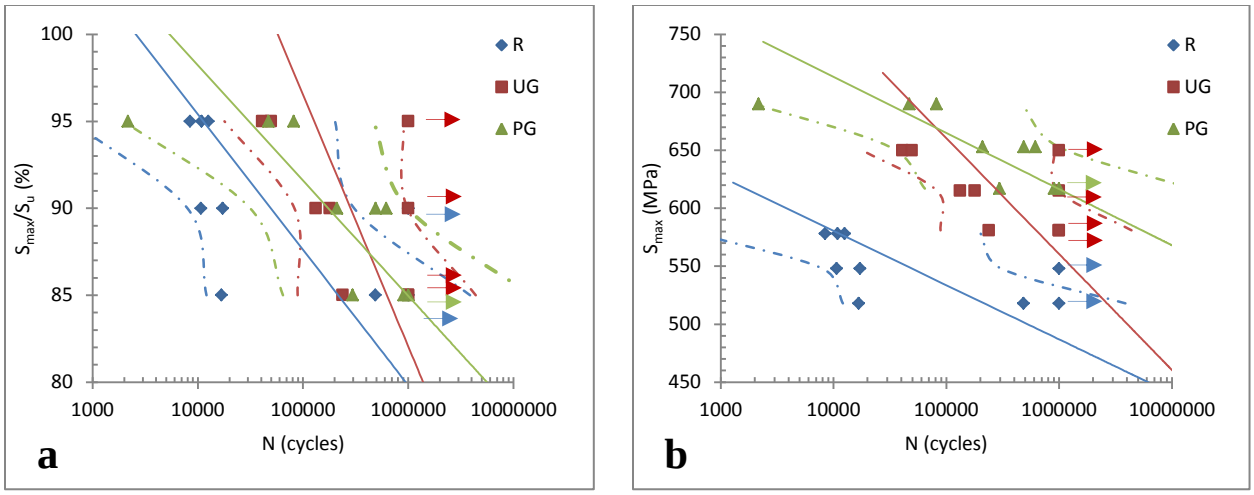

Figure 6-6. Stress-Life (S-N) curves for the fatigue performance of the CFRPs based on reference (R), patterned GSD grown MWCNTs (PG), and uniform GSD grown MWCNTs fibers. In (a) the vertical axis is maximum cyclic stress as a percent of the tensile strength and in (b) the vertical axis is the maximum cyclic stress.

As shown in Figure 6-6(a), at higher stress ratio levels (i.e. 95% S_u), the fatigue life of the CFRPs shows a decade improvement via GSD grown MWCNTs, while, at the lower stress levels (i.e. 85% S_u) this improvement is not significant. However, when the actual values of the input stresses are considered (shown in Figure 6-6(b)), exceptional life improvements were observed. For example, at the maximum cyclic stress around 580 MPa, the CFRPs with uniform GSD grown MWCNTs (UG) have almost 2 decades higher fatigue life compared to the reference CFRPs. Furthermore, the CFRPs with patterned GSD grown MWCNTs (PG) illustrated almost one decade higher fatigue life compared to the CFRPs based on the UG fibers. This noticeable fatigue life extension via the GSD grown MWCNTs can be interpreted as improvements in the damage tolerance of the CFRPs. Figure 6-7 shows the representative damage factor vs. loading cycle curves for the tested CFRPs. The S-N curves relations were calculated according to the ASTM standard and presented in equations (6.2), (6.3) and (6.4), respectively for the CFRP based on reference, uniform MWCNTs and patterned MWCNTs grown fibers.

$$Log(N) = 16.407 - 0.021S \tag{6.2}$$

$$Log(N) = 11.606 - 0.010S \tag{6.3}$$

$$Log(N) = 18.733 - 0.021S \tag{6.4}$$

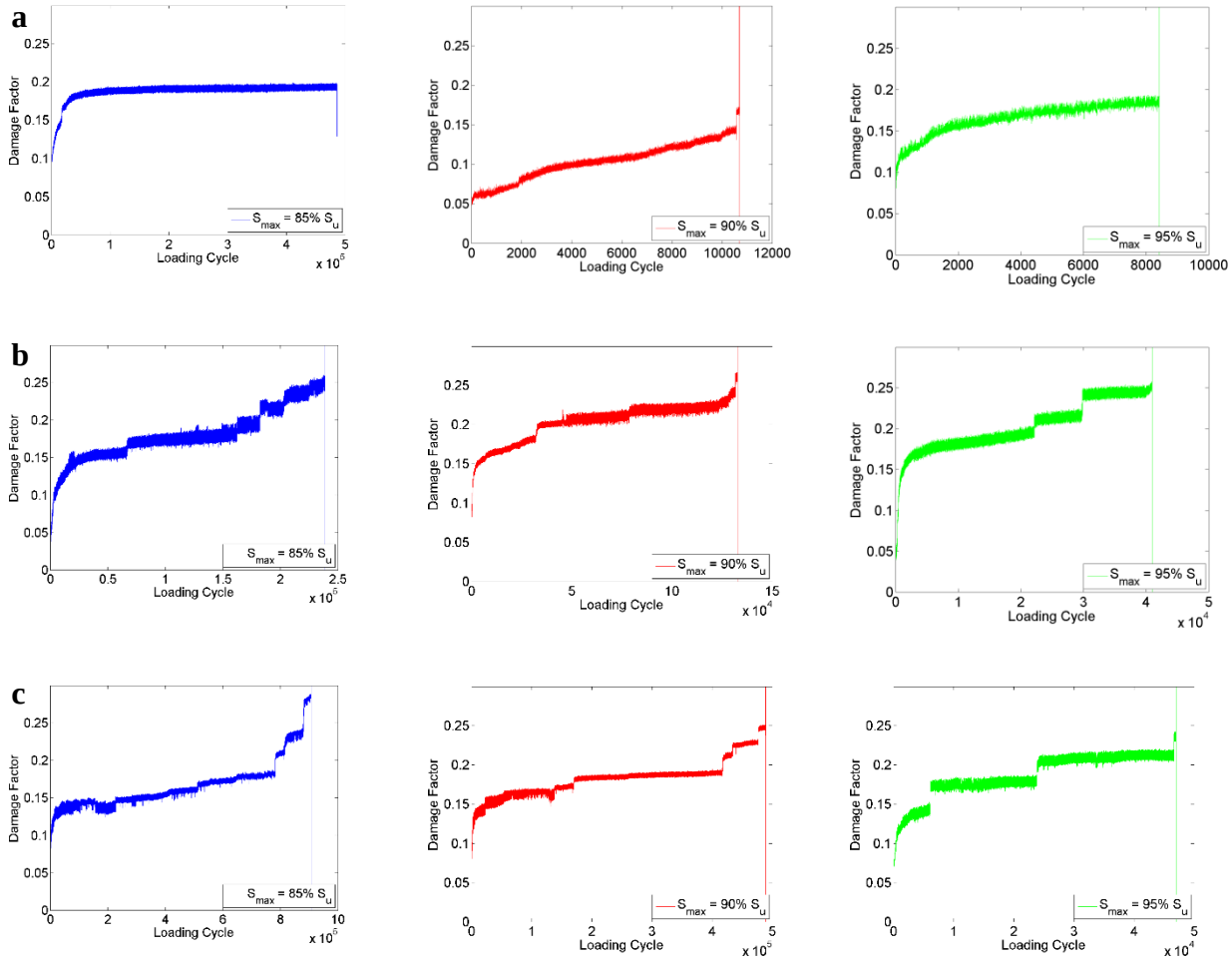

Figure 6-7. Representative damage factors vs. loading cycle curves for the CFRPs based on (a) reference, (b) uniform GSD grown MWCNT and (c) patterned GSD grown MWCNT fibers at three different stress levels.

Comparing the damage factor curves of Figure 6-7, it can be seen that the CFRPs with no MWCNTs (e.g. reference CFRPs) reached their final failure at lower damage factor (under DF=0.2 and around 0.18), while the CFRPs with MWCNTs all exceeded DF=0.2 and reached their final failure at damage factors around 0.25. From these results, it can be concluded that the CFRPs comprising MWCNTs could perform longer at the existence of damage, while the reference CFRPs could not stand the higher levels of damage and fail faster. The effect of this damage tolerance can be seen at the pictures of the fractured samples, in Figure 6-8.

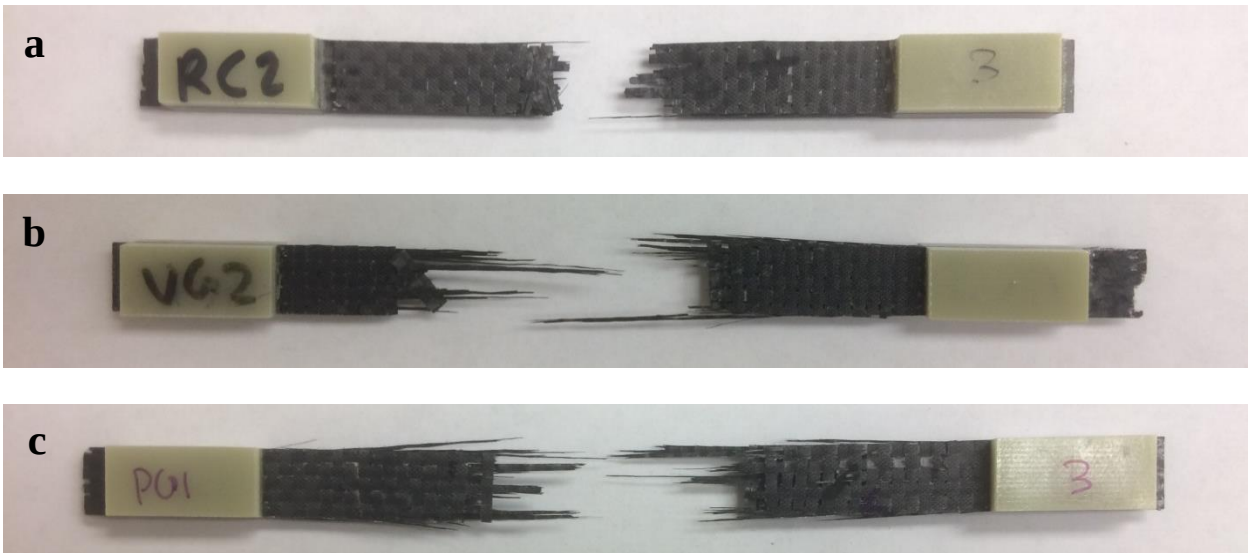

Figure 6-8. Fractured samples under cyclic loading for different CFRPs based on (a) reference, (b) uniform GSD grown MWCNT and (c) patterned GSD grown MWCNT fibers.

During a cyclic loading, damage can initiate at any point along a sample. This initiated damage can propagate through the sample and cause the final failure. In a material with low damage tolerance, the first initiated damages propagate rapidly leading to the final failure. In contrary, high damage-tolerant materials allow for other damages to form and propagate while a damage already pre-existed in the material. As a result, the final fractured material would show multiple damaged places. That could explain why the samples with the GSD grown MWCNTs

(Figure 6-8(b and c)) showed several strands' failures at different locations along the sample, while the reference CFRPs with no MWCNTs (Figure 6-8(a)) exhibited almost flat fracture surfaces.

The ability of the surface grown MWCNTs to stop the matrix cracks from entering the fibers can be the main reason for the improvement in the damage tolerance and fatigue life. The SEM micrographs of the fractured CFRPs are shown in Figure 6-9.

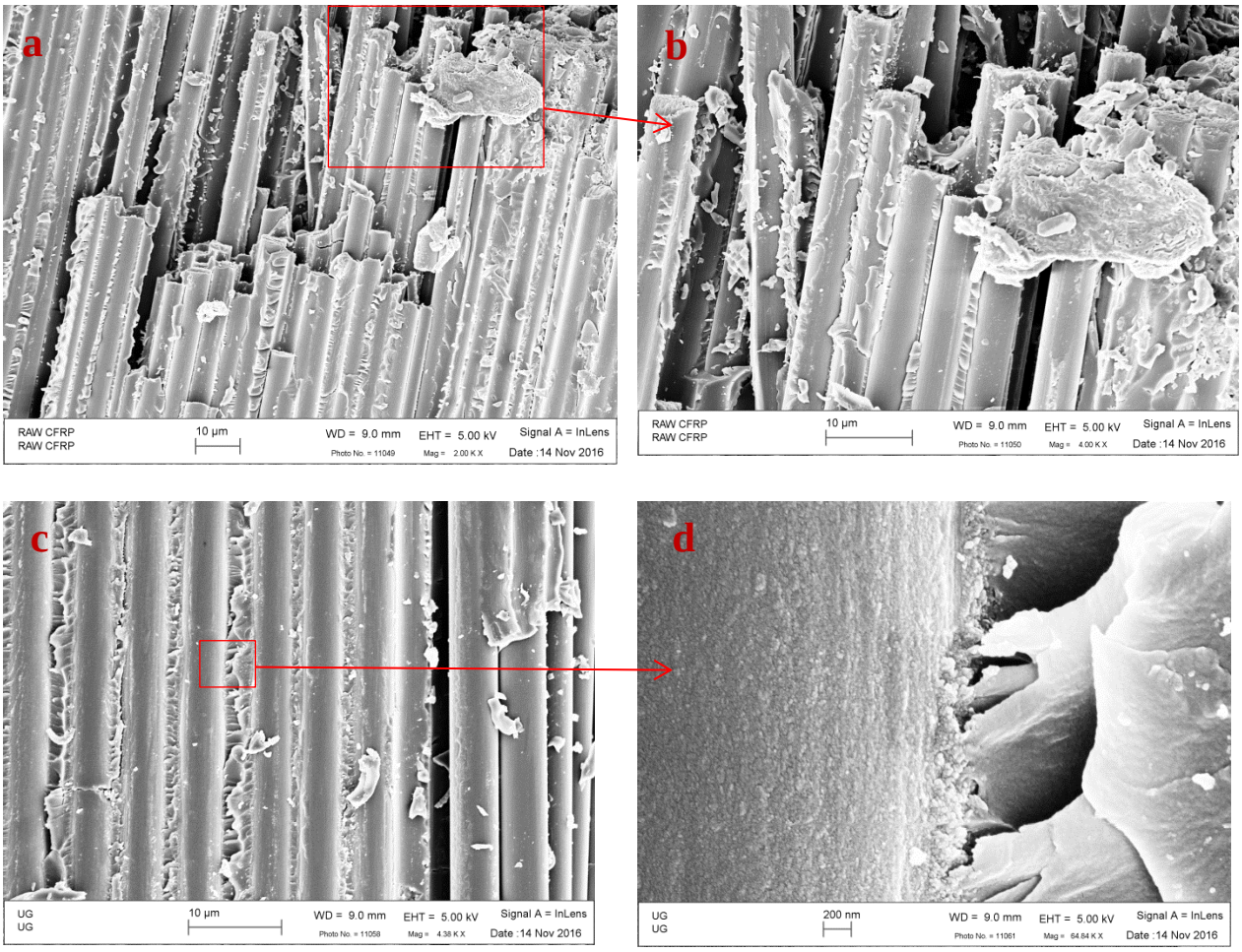

Figure 6-9. SEM micrographs of the fractured samples under cyclic loading for different CFRPs based on (a and b) reference, and (c and d) uniform GSD grown MWCNT fibers.

Different damage mechanisms, like matrix cracking, fiber/matrix debonding and fiber fracture can be identified in Figure 6-9. The fibers were fractured perpendicular to the loading direction. The matrix cracks perpendicular to the fibers can also be seen. However, from Figure 6-9(d) the role of the surface grown MWCNTs in matrix crack blocking can be seen.

6.4.4 Effect of ZnO nanorod growth on CFRPs' fatigue performance

The CFRPs based on ZnO nanorod grown fibers were also tested in fatigue, at three stress levels same as in the fatigue tests for reference samples. The results show that, at the stress levels of 90% and 85% of tensile strength, all the samples overran beyond a million cycles, therefore S-N curves could not be achieved for this CFRP configuration. However, Figure 6-10 shows the S-N results for the Z samples compared to the results captured from the reference CFRPs. The overrun data points are indicated with small arrows next to them.

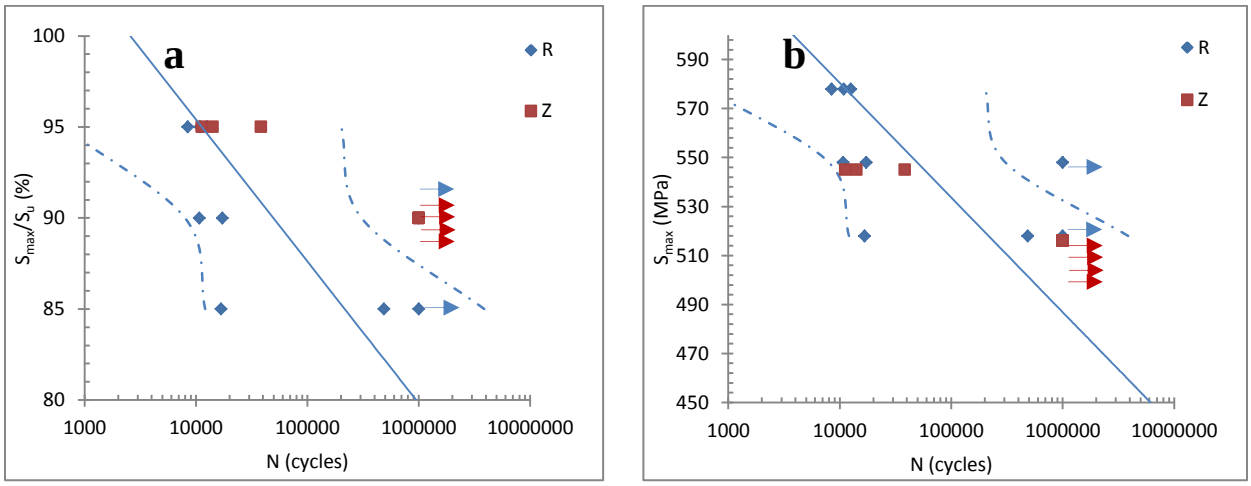

Figure 6-10. Stress-Life (S-N) results of the CFRPs based on the ZnO nanorod grown (z) fibers in comparison with the S-N curve of the reference (R) CFRPs. In (a) the vertical axis is maximum cyclic stress as a percent of the tensile strength and in (b) the vertical axis is the maximum cyclic stress.

Compared to the reference CFRPs, it can be seen that at high stress levels (~550 MPa) the CFRPs based on Z fibers underperformed. However, at lower stress levels (~520 MPa), they exceeded 1 million cycles. Damage factor history results were also captured for the hybrid CFRPs based on ZnO nanorod grown fibers and plotted in Figure 6-11.

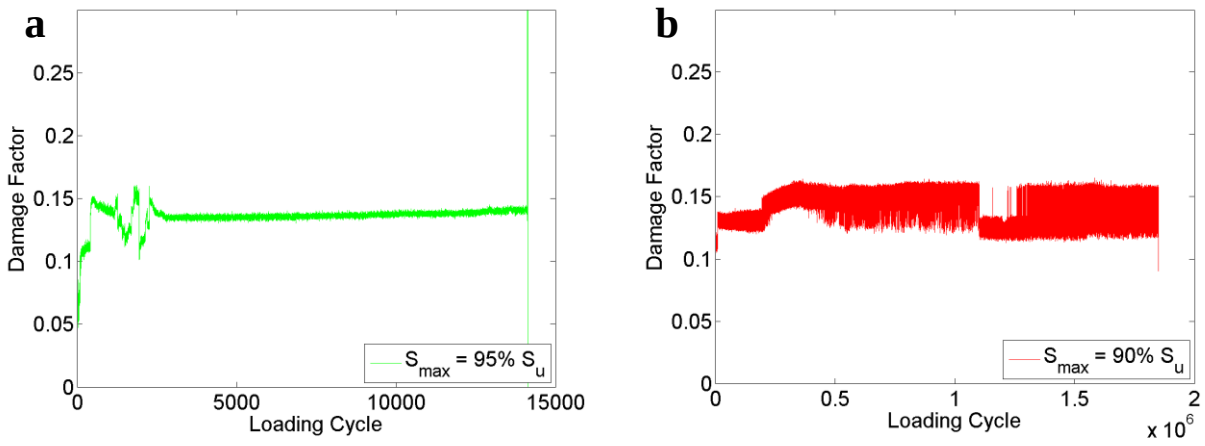

Figure 6-11. Representative damage factors vs. loading cycle curves for the CFRPs based on ZnO nanorod grown fibers. (a) at 95% of tensile strength stress level, and (b) at 90% of tensile strength stress level.

Comparing the damage factor history curves of Figure 6-11 with the curves of Figure 6-7 reveals that the CFRPs based on Z fibers illustrated a sudden jump in damage factor at the initial cycles. This sudden jump can signify a signature damage mode for these CFRPs; delamination. It was observed that almost all of these samples exhibited large delamination areas after they were visually examined after running the tests; for the samples reached their final fracture, as well as the samples exceeded 1 million cycles. Delamination damage is known to severely limit the fatigue life of the FRPs. However, for the current tests performed in and under 90% of S_u, the stresses were not high enough to initiate a damage level necessary to fail the individual plies. Figure 6-12 shows a fractured CFRP sample based on Z fibers.

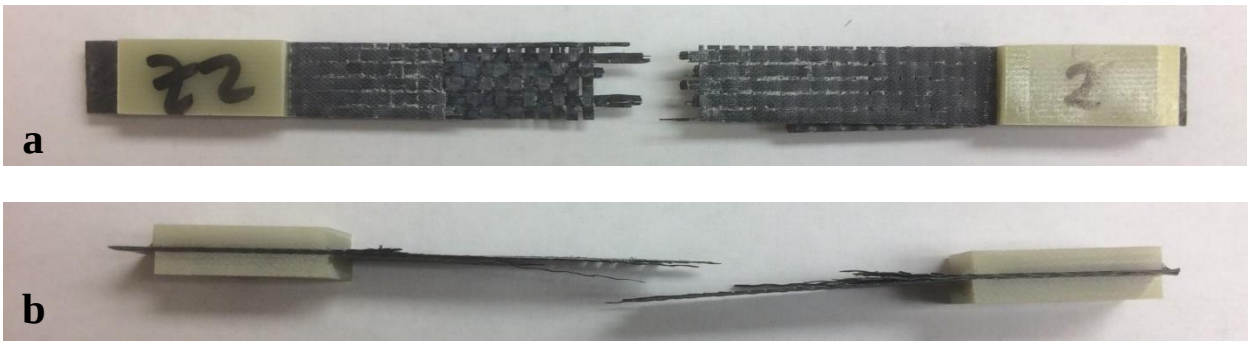

Figure 6-12. Fractured samples under cyclic loading for the CFRPs based on ZnO nanorod grown fibers from front (a) and side (b) views.

The large areas of delamination can be seen in Figure 6-12 causing the CFRPs to lose their integrity long before the final failure. Figure 6-13 shows the SEM micrographs of the fractured CFRP based on the Z fibers in a delaminated region.

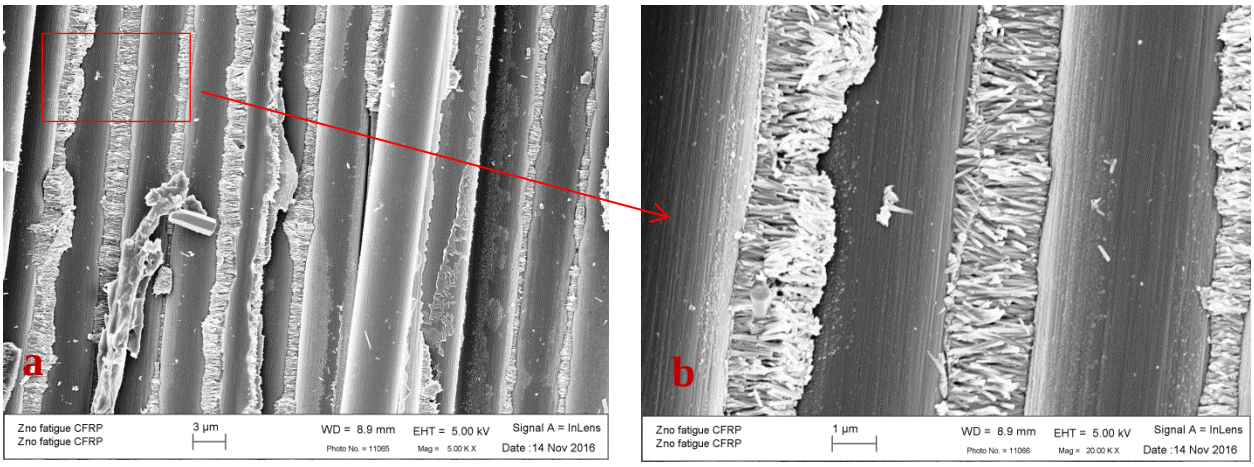

Figure 6-13. SEM micrographs of the fractured samples under cyclic loading for the CFRPs based on ZnO nanorod grown fibers. (a and b) have different magnifications.

Inferred from Figure 6-13, the ZnO nanorod forests are almost completely detached from the carbon fibers surface, resulting in large delamination areas.

6.5 Conclusions

Graphitic structure by design (GSD) technique was employed to grow MWCNTs over unsized woven carbon fibers. Two different topologies of MWCNTs frosts were considered: uniform growth of CNTs forest and checkerboard patterned CNTs forest. To unravel the effects of exposure to GSD method environment, some as-received carbon fibers were exposed to the GSD temperature and the gas mixture, except they lacked the catalyst layer and therefore lacked MWCNTs growth at the end. A hydrothermal ZnO nanorods synthesis technique was utilized to grow ZnO nanorods over the carbon fibers. Again, some of the as-received carbon fibers were immersed in DI water as hot as the solution in the hydrothermal process, to probe the effects of the process environment. Hybrid CFRPs based on different surface-treated fibers were fabricated. The different designed CFRPs were examined in tension to obtain their tensile strengths, as well as their elastic moduli and strain-to-failures. The surface grown CNTs promoted the tensile strength of the CFRPs by 12% and 19%, via uniform and checkerboard-patterned growth morphologies, respectively, over the carbon fiber fabrics. However, 6% reduction in the tensile strength of the CFRPs was observed via growing relatively long ZnO nanorods over the carbon fibers. The designed CFRPs then tested in tension-tension fatigue experiments to see the effect of nano-reinforcements growth on the fatigue behavior of the CFRPs. Stress-Life (S-N) curves were obtained at stress levels of 85%, 90% and 95% of the CFRPs' tensile strength at the cycling stress ratio of 0.10. Outstanding damage tolerance was observed in the CFRPs based on uniform and patterned grown CNT fibers. Almost two decades of fatigue life extension was achieved via surface grown CNTs. However, the samples possessing surface grown ZnO nanorods displayed large delamination areas under cyclic loading, resulting in poor fatigue performance.

Chapter 7. **Conclusions and Future Work**

In the experimental studies of this dissertation, carbon fibers underwent two different nano-reinforcements synthesis techniques to produce hierarchical reinforcements; (a) graphitic structure by design (GSD) method was used to grow multi-walled carbon nanotubes (MWCNTs), and (b) hydrothermal technique was employed to grow zinc oxide (ZnO) nanorods over the carbon fibers. The carbon fibers with surface grown ZnO nanorods or CNTs were utilized to fabricate hybrid carbon fiber reinforced polymer composites (CFRPs). In order to reveal the effects of the different parameters encountered in the nano-reinforcement growth techniques (e.g., exposure to the GSD temperature, uniform or patterned CNT growth topologies, exposure to hydrothermal environment, and ZnO nanorods growth), carbon fibers underwent various surface treatments. In one investigation, two methods were utilized to pre-deposit a thin seeding layer of ZnO on the surface of the woven carbon fiber fabrics. These two methods comprised (a) ZnO magnetron sputtering, and (b) airbrush spraying of dispersed ZnO nanoparticles/solvent mixture techniques. The pre-coated carbon fibers underwent a hydrothermal ZnO nanorods synthesis process. As a result of the different pre-coating techniques, different morphologies of ZnO nanorods forests were grown over the carbon fibers. Radially aligned ZnO nanorods were obtained utilizing the sputtering technique for pre-coating the fibers, while randomly aligned nanorods were grown using the airbrush spraying method.

Carbon fiber reinforced composite laminates were fabricated based on the different surface-treated fibers. The CFRPs were investigated via quasi-static tension, 3-poin bending dynamic mechanical analysis (DMA), double cantilever beam (DCB), high velocity impact (HVI) and tension-tension fatigue experiments, in order to reveal the effects of the nano-reinforcements with different growth morphologies on the static and dynamic in-plane and out-of-plane

mechanical performance of the hybrid CFRPs. Finite element method (FEM) was also employed to simulate the hybrid CFRPs interlaminar crack propagation. As a summary of the obtained results:

- The CFRPs possessing randomly aligned ZnO nanorods illustrated outstanding improvements in the CFRPs in-plane strength (18%) and strain to failure (47%), due to their strong fiber/matrix interface region. However, minor improvements in strength and strain-to-failure of the CFRPs were achieved via radially grown ZnO nanorods.
- The long, thin, and controlled ZnO nanorods morphology provided stronger adhesion between the ZnO nanorods and polymer matrix than the adhesion between the ZnO nanorods and carbon fibers. This characteristic caused the CFRPs with radially aligned carbon fibers to show local delamination failure right before the final fracture in the quasi-static tension tests.
- The radially aligned ZnO nanorods introduce larger surface area to the CFRPs structure than the randomly aligned ones. Therefore, vibration attenuation capabilities of the CFRPs with radially aligned ZnO nanorods were higher than the ones with randomly aligned ZnO nanorods. As a result of DMA tests, loss tangent of the CFRPs were improved by 26% and 18% via growing radially and randomly aligned ZnO nanorods, respectively.
- Outstanding improvements of 34% and 23% in mode I interlaminar fracture toughness (G_{Ic}) of the CFRPs were achieved via patterned and uniform growth of MWCNTs over carbon fibers. Fractographs taken by a scanning electron microscope (SEM) revealed that the mechanical interlocking of the polymers in-between the CNTs, CNTs pull-out and

rupture, matrix/CNT frictional slip, and matrix micro-cracks at the fiber/matrix interface were the energy dissipating mechanisms yielding the improvements in G_{Ic}.

- Dramatic drop in G_{Ic} (37%) was observed for the CFRP configuration with surface grown ZnO nanorods. The fractographs revealed that the interlaminar crack propagated between the ZnO nanorods forests and their substrate carbon fibers, rather than propagating between the ZnO nanorods forests of opposing interlaminar faces.
- The results of the FEM simulations -using the cohesive elements- revealed that the hybrid CFRP based on uniform MWCNs grown fiber possessed 55% higher interlaminar strength compared to the reference CFRP based on raw fibers and via patterned growth of MWCNTs, the ultimate crack opening of the CFRPs improved by 20%.
- The FEM simulations taking into consideration the fluctuations of the fracture toughness along the delamination region was successful in simulating the unstable crack growth behavior of the hybrid CFRPs.
- Via growing MWCNTs, ZnO nanorods, and MWCNT/ZnO nanorod nano-reinforcements over the carbon fiber fabrics, the dissipated impact energies of the CFRPs were improved 16%, 20%, and 21%, respectively, confirming the significant improvements in the delamination resistance of the hybrid CFRPs. These results were reinforced by measuring the delamination lengths of the impacted samples, where 30% less delamination zone was obtained in the CFRP hybridized by MWCNT/ZnO nanorod nano-reinforcing whiskers compared to the CFRP with no surface treatment.
- The surface grown CNTs promoted the tensile strength of the CFRPs by 12% and 19%, via uniform and checkerboard-patterned growth morphologies, respectively, over the carbon fiber fabrics.

- Noticeable damage tolerance was observed in the CFRPs based on uniform and patterned grown CNT fibers where almost 2.0 decades of fatigue life extension was accomplished. At high stress levels, this improvement was more pronounced.
- The CFRPs possessing long surface grown ZnO nanorods displayed large delamination zones under cyclic loading, resulting in poor fatigue performance.
- It is worth mentioning that among the different fiber hybridization techniques, the surface growth of ZnO, utilizing the airbrush technique to deposit the catalyst is by far the most affordable and will not change the cost of the CFRPs by no more than 3%.

Table 7-1. Summary of the performed investigations.

Chapter number	Mechanical property measured	CFRP configuration with highest improvement	Nano-reinforcement	Percent improvement.
Chapter 2	Tensile strength	AWZ	Randomly oriented long (~2μm) ZnO nanorods	18%
	Strain to failure	AWZ	Randomly oriented long (~2μm) ZnO nanorods	47%
	Vibration attenuation (tan δ)	SWZ	Radially aligned long (~2μm) ZnO nanorods	26%
Chapter 3	Interlaminar fracture toughness (GIc)	PG	Patterned grown MWCNTs	29% for crack initiation and 34% for crack growth
Chapter 4	Interlaminar strength	UG	Uniform grown MWCNTs	55%
	Ultimate interlaminar crack opening	PG	Patterned grown MWCNTs	20%
Chapter 5	Tensile strength	GH	Radially aligned short (~1μm) ZnO nanorods	3% compared to de-sized fiber
	Strain to failure	GG	MWCNTs grown over Radially aligned short (~1μm) ZnO nanorods	4.5%
	Impact energy dissipation	GG	MWCNTs grown over Radially aligned short (~1μm) ZnO nanorods	21%
Chapter 6	Fatigue life	PG	Patterned grown MWCNTs	~ 2.0 decades

Table 7-1 summarizes the major improvements in mechanical properties throughout the performed investigations by adopting different configurations of the hybrid CFRPs.

As a result of all the aforementioned investigations the following tasks are proposed for future work:

- The procedure of synthesizing the long randomly aligned ZnO nanorods has the capability to be scaled-up. Furthermore, promising mechanical behavior improvements were observed in the CFRPs based on randomly aligned ZnO nanorod grown fibers. Compared to CFRPs with long radially aligned ZnO nanorods, they exhibited less delamination damage. They have the potential capability to improve the interlaminar fracture toughness and fatigue performance of the hybrid CFRPs. As a future work, these investigations can be carried out.Because, different loading modes of interlaminar fracture exhibit different fracture mechanisms, the interlaminar fracture toughness experiments, modes II, III and mixed mode II/III can also be examined for the designed hybrid CFRPs. The role of nano-reinforcements in resisting these fracture mechanisms can be investigated.
- After experimentally examining the CFRPs' behavior in the interlaminar fracture resistance, FEM can be used to develop accurate models of the hybrid CFRPs.
- FEM simulations of the CFRPs under impact loading can be accurately carried out, when the different modes of interlaminar fracture toughness of the CFRPs achieved.
- FEM can also be employed in modeling the CFRPs behavior under cyclic loading.

List of Publications related to the dissertation

1. M. Al-Haik, **A. Y. Boroujeni** and M. Tehrani, Chapter 5: ballistic damage of hybrid composite materials, In Advanced Fibrous Composite Materials for Ballistic Protection, Xiaogang Chen and Gwen Jones(Ed), Woodhead Publishing, Cambridge, UK (2016).
2. **A. Y. Boroujeni**, A. A. Skandani, A. Emami, F. Yazdandoost, M. A;-Haik (2016). A hybrid ZnO nanorod/carbon nanotube/carbon fiber reinforced polymer composite; synthesis and mechanical characterization, under review in journal of Advanced Composite Materials.
3. **A. Y. Boroujeni**, M. Tehrani, A.J. Nelson, M.S. Al-Haik (2015). Effect of carbon nanotubes growth topology on the mechanical behavior and damage of hybrid carbon nanotube/carbon fiber polymer composites. Polymer Composites.
4. **A. Y. Boroujeni**, M. Tehrani, A.J. Nelson, M.S. Al-Haik (2014). Hybrid carbon nanotube-carbon fiber composites with improved in-plane mechanical properties. Composites Part B: Engineering, 66, pp.475-83.
5. **A.Y. Boroujeni**, M. Philen, M. Al-Haik, "Smart hybrid ZnO nanowire/carbon fiber reinforced polymer composites with in-situ structural health monitoring capability," American Society for Composites 30th Technical Conference Sep. 28-30, East Lansing, Michigan (2015).
6. **A.Y. Boroujeni**, A.A. Skandani, A. Emami, M. Al-Haik, "Impact performance of a hybrid ZnO nanorod/carbon nanotube/carbon fiber reinforced polymer composite," American Society for Composites 30th Technical Conference Sep. 28-30, East Lansing, Michigan (2015).

References

1. Hyer, M.W. *Stress analysis of fiber-reinforced composite materials*. DEStech Publications, Inc: 2009.
2. Gibson, R.F. A review of recent research on mechanics of multifunctional composite materials and structures. *Composite structures* **2010**, *92*, 2793-2810.
3. Knops, M. *Analysis of failure in fiber polymer laminates: The theory of alfred puck*. Springer Science & Business Media: 2008.
4. Khan, S.U.; Kim, J.-K. Impact and delamination failure of multiscale carbon nanotube-fiber reinforced polymer composites. *International Journal of Aeronautical and Space Sciences* **2011**, *12*, 115-133.
5. Kim, J.-K.; Mai, Y.-W. *Engineered interfaces in fiber reinforced composites*. Elsevier: 1998.
6. Trabelsi, W.; Michel, L.; Othomene, R. Effects of stitching on delamination of satin weave carbon-epoxy laminates under mode i, mode ii and mixed-mode i/ii loadings. *Applied Composite Materials* **2010**, *17*, 575-595.
7. Chung, D. Structural composite materials tailored for damping. *Journal of Alloys and Compounds* **2003**, *355*, 216-223.
8. Aksoy, A.; Carlsson, L. Interlaminar shear fracture of interleaved graphite/epoxy composites. *Composites science and technology* **1992**, *43*, 55-69.
9. Qian, H.; Greenhalgh, E.S.; Shaffer, M.S.; Bismarck, A. Carbon nanotube-based hierarchical composites: A review. *Journal of Materials Chemistry* **2010**, *20*, 4751-4762.
10. Li, D.; Zhang, X.; Sui, G.; Wu, D.; Liang, J.; Yi, X.-S. Toughness improvement of epoxy by incorporating carbon nanotubes into the resin. *Journal of materials science letters* **2003**, *22*, 791-793.
11. Xia, Z.; Curtin, W.; Sheldon, B. Fracture toughness of highly ordered carbon nanotube/alumina nanocomposites. *Journal of engineering materials and technology* **2004**, *126*, 238-244.
12. Tehrani, M.; Safdari, M.; Al-Haik, M. Nanocharacterization of creep behavior of multiwall carbon nanotubes/epoxy nanocomposite. *International Journal of Plasticity* **2011**, *27*, 887-901.
13. Soliman, E.; Al-Haik, M.; Taha, M.R. On and off-axis tension behavior of fiber reinforced polymer composites incorporating multi-walled carbon nanotubes. *Journal of Composite Materials* **2012**, *46*, 1661-1675.
14. Soliman, E.M.; Sheyka, M.P.; Taha, M.R. Low-velocity impact of thin woven carbon fabric composites incorporating multi-walled carbon nanotubes. *International Journal of Impact Engineering* **2012**, *47*, 39-47.
15. Suhr, J.; Koratkar, N.A. Energy dissipation in carbon nanotube composites: A review. *Journal of Materials Science* **2008**, *43*, 4370-4382.
16. Kundalwal, S.; Ray, M. Effect of carbon nanotube waviness on the effective thermoelastic properties of a novel continuous fuzzy fiber reinforced composite. *Composites Part B: Engineering* **2014**, *57*, 199-209.
17. Wang, B.-C.; Zhou, X.; Ma, K.-M. Fabrication and properties of cnts/carbon fabric hybrid multiscale composites processed via resin transfer molding technique. *Composites Part B: Engineering* **2013**, *46*, 123-129.

18. Zhu, S.; Su, C.-H.; Lehoczky, S.; Muntele, I.; Ila, D. Carbon nanotube growth on carbon fibers. *Diamond and Related Materials* **2003**, *12*, 1825-1828.
19. Zhang, Q.; Liu, J.; Sager, R.; Dai, L.; Baur, J. Hierarchical composites of carbon nanotubes on carbon fiber: Influence of growth condition on fiber tensile properties. *Composites Science and Technology* **2009**, *69*, 594-601.
20. Sinnott, S.B.; Andrews, R. Carbon nanotubes: Synthesis, properties, and applications. *Critical Reviews in Solid State and Materials Sciences* **2001**, *26*, 145-249.
21. Yamamoto, N.; Hart, A.J.; Garcia, E.J.; Wicks, S.S.; Duong, H.M.; Slocum, A.H.; Wardle, B.L. High-yield growth and morphology control of aligned carbon nanotubes on ceramic fibers for multifunctional enhancement of structural composites. *Carbon* **2009**, *47*, 551-560.
22. Tehrani, M.; Safdari, M.; Boroujeni, A.; Razavi, Z.; Case, S.; Dahmen, K.; Garmestani, H.; Al-Haik, M. Hybrid carbon fiber/carbon nanotube composites for structural damping applications. *Nanotechnology* **2013**, *24*, 155704.
23. Qian, H.; Bismarck, A.; Greenhalgh, E.S.; Shaffer, M.S. Carbon nanotube grafted carbon fibres: A study of wetting and fibre fragmentation. *Composites Part A: Applied science and manufacturing* **2010**, *41*, 1107-1114.
24. Thostenson, E.; Li, W.; Wang, D.; Ren, Z.; Chou, T. Carbon nanotube/carbon fiber hybrid multiscale composites. *Journal of Applied physics* **2002**, *91*, 6034-6037.
25. Chen, X.; Saito, T.; Kusunoki, M.; Motojima, S. Three-dimensional vapor growth mechanism of carbon microcoils. *Journal of materials research* **1999**, *14*, 4329-4336.
26. Veedu, V.P.; Cao, A.; Li, X.; Ma, K.; Soldano, C.; Kar, S.; Ajayan, P.M.; Ghasemi-Nejhad, M.N. Multifunctional composites using reinforced laminae with carbon-nanotube forests. *Nature materials* **2006**, *5*, 457-462.
27. Luhrs, C.C.; Garcia, D.; Tehrani, M.; Al-Haik, M.; Taha, M.R.; Phillips, J. Generation of carbon nanofilaments on carbon fibers at 550 c. *Carbon* **2009**, *47*, 3071-3078.
28. Tehrani, M.; Yari Boroujeni, A.; Luhrs, C.; Phillips, J.; Al-Haik, M.S. Hybrid composites based on carbon fiber/carbon nanofilament reinforcement. *Materials* **2014**, *7*, 4182-4195.
29. Boroujeni, A.; Tehrani, M.; Nelson, A.; Al-Haik, M. Hybrid carbon nanotube–carbon fiber composites with improved in-plane mechanical properties. *Composites Part B: Engineering* **2014**, *66*, 475-483.
30. Boroujeni, A.; Tehrani, M.; Nelson, A.; Al-Haik, M. Effect of carbon nanotubes growth topology on the mechanical behavior of hybrid carbon nanotube/carbon fiber polymer composites. *Polymer Composites* **2015**, *accepted for publication*.
31. Ehlert, G.J.; Lin, Y.; Galan, U.; Sodano, H.A. Interaction of zno nanowires with carbon fibers for hierarchical composites with high interfacial strength. *Journal of Solid Mechanics and Materials Engineering* **2010**, *4*, 1687-1698.
32. Lin, Y.; Ehlert, G.; Sodano, H.A. Increased interface strength in carbon fiber composites through a zno nanowire interphase. *Advanced functional materials* **2009**, *19*, 2654-2660.
33. Yu, D.; Trad, T.; McLeskey Jr, J.T.; Craciun, V.; Taylor, C.R. Zno nanowires synthesized by vapor phase transport deposition on transparent oxide substrates. *Nanoscale research letters* **2010**, *5*, 1333-1339.
34. Montenegro, D.; Souissi, A.; Martínez-Tomás, C.; Muñoz-Sanjosé, V.; Sallet, V. Morphology transitions in zno nanorods grown by mocvd. *Journal of Crystal Growth* **2012**, *359*, 122-128.

35. Jimenez-Cadena, G.; Comini, E.; Ferroni, M.; Vomiero, A.; Sberveglieri, G. Synthesis of different zno nanostructures by modified pvd process and potential use for dye-sensitized solar cells. *Materials Chemistry and Physics* **2010**, *124*, 694-698.
36. Su, S.; Lu, Y.; Zhang, Z.; Li, B.; Shen, D.; Yao, B.; Zhang, J.; Zhao, D.; Fan, X. Structural, optical, and hydrogenation properties of zno nanowall networks grown on a si (111) substrate by plasma-assisted molecular beam epitaxy. *Physica B: Condensed Matter* **2008**, *403*, 2590-2593.
37. Hassan, N.; Hashim, M.; Bououdina, M. One-dimensional zno nanostructure growth prepared by thermal evaporation on different substrates: Ultraviolet emission as a function of size and dimensionality. *Ceramics International* **2013**, *39*, 7439-7444.
38. Ramgir, N.S.; Subannajui, K.; Yang, Y.; Grimm, R.; Michiels, R.; Zacharias, M. Reactive vls and the reversible switching between vs and vls growth modes for zno nanowire growth. *The Journal of Physical Chemistry C* **2010**, *114*, 10323-10329.
39. Skandani, A.A.; Masghouni, N.; Case, S.; Leo, D.; Al-Haik, M. Enhanced vibration damping of carbon fibers-zno nanorods hybrid composites. *Applied Physics Letters* **2012**, *101*, 073111.
40. Alipour Skandani, A.; Yari Boroujeni, A.; Kalhor, R.; Case, S.W.; Al-Haik, M. Viscoelastic behavior of epoxy/carbon fiber/zno nano-rods hybrid composites. *Polymer Composites* **2014**.
41. Masghouni, N.; Al-Haik, M. Quasistatic and dynamic mechanical characterization of a woven carbon fiber–zinc oxide nanowires–epoxy composite. *Polymer Composites* **2014**.
42. Wang, Z.L. Energy harvesting for self-powered nanosystems. *Nano Research* **2008**, *1*, 1-8.
43. Wang, Z.L. Energy harvesting using piezoelectric nanowires–a correspondence on "energy harvesting using nanowires?" by alexe et al. *Advanced Materials* **2009**, *21*, 1311-1315.
44. Gullapalli, H.; Vemuru, V.S.; Kumar, A.; Botello-Mendez, A.; Vajtai, R.; Terrones, M.; Nagarajaiah, S.; Ajayan, P.M. Flexible piezoelectric zno–paper nanocomposite strain sensor. *Small* **2010**, *6*, 1641-1646.
45. Kumar, A.; Gullapalli, H.; Balakrishnan, K.; Botello-Mendez, A.; Vajtai, R.; Terrones, M.; Ajayan, P.M. Flexible zno–cellulose nanocomposite for multisource energy conversion. *Small* **2011**, *7*, 2173-2178.
46. Masghouni, N.; Burton, J.; Philen, M.; Al-Haik, M. Investigating the energy harvesting capabilities of a hybrid zno nanowires/carbon fiber polymer composite beam. *Nanotechnology* **2015**, *26*, 095401.
47. Du, J.; Bai, J.; Cheng, H. The present status and key problems of carbon nanotube based polymer composites. *Express Polymer Letters* **2007**, *1*, 253-273.
48. Spitalsky, Z.; Tasis, D.; Papagelis, K.; Galiotis, C. Carbon nanotube–polymer composites: Chemistry, processing, mechanical and electrical properties. *Progress in polymer science* **2010**, *35*, 357-401.
49. Thostenson, E.T.; Ren, Z.; Chou, T.-W. Advances in the science and technology of carbon nanotubes and their composites: A review. *Composites science and technology* **2001**, *61*, 1899-1912.
50. Fiedler, B.; Gojny, F.H.; Wichmann, M.H.; Nolte, M.C.; Schulte, K. Fundamental aspects of nano-reinforced composites. *Composites science and technology* **2006**, *66*, 3115-3125.

51. Gryshchuk, O.; Karger-Kocsis, J.; Thomann, R.; Kónya, Z.; Kiricsi, I. Multiwall carbon nanotube modified vinylester and vinylester–based hybrid resins. *Composites Part A: Applied Science and Manufacturing* **2006**, *37*, 1252-1259.
52. Ma, P.C.; Kim, J.-K.; Tang, B.Z. Effects of silane functionalization on the properties of carbon nanotube/epoxy nanocomposites. *Composites Science and Technology* **2007**, *67*, 2965-2972.
53. Gojny, F.H.; Wichmann, M.H.; Fiedler, B.; Schulte, K. Influence of different carbon nanotubes on the mechanical properties of epoxy matrix composites–a comparative study. *Composites Science and Technology* **2005**, *65*, 2300-2313.
54. Ganguli, S.; Bhuyan, M.; Allie, L.; Aglan, H. Effect of multi-walled carbon nanotube reinforcement on the fracture behavior of a tetrafunctional epoxy. *Journal of materials science* **2005**, *40*, 3593-3595.
55. Yokozeki, T.; Iwahori, Y.; Ishiwata, S.; Enomoto, K. Mechanical properties of cfrp laminates manufactured from unidirectional prepregs using cscnt-dispersed epoxy. *Composites Part A: Applied Science and Manufacturing* **2007**, *38*, 2121-2130.
56. Godara, A.; Mezzo, L.; Luizi, F.; Warrier, A.; Lomov, S.V.; Van Vuure, A.; Gorbatikh, L.; Moldenaers, P.; Verpoest, I. Influence of carbon nanotube reinforcement on the processing and the mechanical behaviour of carbon fiber/epoxy composites. *Carbon* **2009**, *47*, 2914-2923.
57. Warrier, A.; Godara, A.; Rochez, O.; Mezzo, L.; Luizi, F.; Gorbatikh, L.; Lomov, S.V.; VanVuure, A.W.; Verpoest, I. The effect of adding carbon nanotubes to glass/epoxy composites in the fibre sizing and/or the matrix. *Composites Part A: Applied Science and Manufacturing* **2010**, *41*, 532-538.
58. Inam, F.; Wong, D.W.; Kuwata, M.; Peijs, T. Multiscale hybrid micro-nanocomposites based on carbon nanotubes and carbon fibers. *Journal of Nanomaterials* **2010**, *2010*, 9.
59. Borowski, E.; Soliman, E.; Kandil, U.F.; Taha, M.R. Interlaminar fracture toughness of cfrp laminates incorporating multi-walled carbon nanotubes. *Polymers* **2015**, *7*, 1020-1045.
60. Wicks, S.S.; de Villoria, R.G.; Wardle, B.L. Interlaminar and intralaminar reinforcement of composite laminates with aligned carbon nanotubes. *Composites Science and Technology* **2010**, *70*, 20-28.
61. Camanho, P.P.; Dávila, C.G. Mixed-mode decohesion finite elements for the simulation of delamination in composite materials. **2002**.
62. Rybicki, E.F.; Kanninen, M. A finite element calculation of stress intensity factors by a modified crack closure integral. *Engineering Fracture Mechanics* **1977**, *9*, 931-938.
63. ABAQUS. In *Abaqus documentation*, Dassault Systèmes, Providence, RI, USA, 2012; Providence, RI, USA.
64. Barenblatt, G.I. The mathematical theory of equilibrium cracks in brittle fracture. *Advances in applied mechanics* **1962**, *7*, 55-129.
65. Dugdale, D.S. Yielding of steel sheets containing slits. *Journal of the Mechanics and Physics of Solids* **1960**, *8*, 100-104.
66. Cui, W.; Wisnom, M. A combined stress-based and fracture-mechanics-based model for predicting delamination in composites. *Composites* **1993**, *24*, 467-474.
67. Shahwan, K.W.; Waas, A.M. In *Non–self–similar decohesion along a finite interface of unilaterally constrained delaminations*, Proceedings of the Royal Society of London A: Mathematical, Physical and Engineering Sciences, 1997; The Royal Society: pp 515-550.

68. De Moura, M.; Gonçalves, J.; Marques, A.; De Castro, P.T. Modeling compression failure after low velocity impact on laminated composites using interface elements. *Journal of Composite Materials* **1997**, *31*, 1462-1479.
69. Reedy, E.; Mello, F.; Guess, T. Modeling the initiation and growth of delaminations in composite structures. *Journal of Composite Materials* **1997**, *31*, 812-831.
70. Grimmer, C.S.; Dharan, C. High-cycle fatigue of hybrid carbon nanotube/glass fiber/polymer composites. *Journal of Materials Science* **2008**, *43*, 4487-4492.
71. Dharan, C. Fatigue failure in graphite fibre and glass fibre-polymer composites. *Journal of Materials Science* **1975**, *10*, 1665-1670.
72. Degrieck, J.; Van Paepegem, W. Fatigue damage modeling of fibre-reinforced composite materials: Review. *Applied Mechanics Reviews* **2001**, *54*, 279-300.
73. Bortz, D.R.; Heras, E.G.; Martin-Gullon, I. Impressive fatigue life and fracture toughness improvements in graphene oxide/epoxy composites. *Macromolecules* **2011**, *45*, 238-245.
74. Davis, D.C.; Wilkerson, J.W.; Zhu, J.; Ayewah, D.O. Improvements in mechanical properties of a carbon fiber epoxy composite using nanotube science and technology. *Composite Structures* **2010**, *92*, 2653-2662.
75. Knoll, J.; Riecken, B.; Kosmann, N.; Chandrasekaran, S.; Schulte, K.; Fiedler, B. The effect of carbon nanoparticles on the fatigue performance of carbon fibre reinforced epoxy. *Composites Part A: Applied Science and Manufacturing* **2014**, *67*, 233-240.
76. Borrego, L.; Costa, J.; Ferreira, J.; Silva, H. Fatigue behaviour of glass fibre reinforced epoxy composites enhanced with nanoparticles. *Composites Part B: Engineering* **2014**, *62*, 65-72.
77. Grimmer, C.S.; Dharan, C. Enhancement of delamination fatigue resistance in carbon nanotube reinforced glass fiber/polymer composites. *Composites Science and Technology* **2010**, *70*, 901-908.
78. Fenner, J.S.; Daniel, I.M. Hybrid nanoreinforced carbon/epoxy composites for enhanced damage tolerance and fatigue life. *Composites Part A: Applied Science and Manufacturing* **2014**, *65*, 47-56.
79. Kostagiannakopoulou, C.; Loutas, T.; Sotiriadis, G.; Markou, A.; Kostopoulos, V. On the interlaminar fracture toughness of carbon fiber composites enhanced with graphene nano-species. *Composites Science and Technology* **2015**, *118*, 217-225.
80. Kamar, N.T.; Hossain, M.M.; Khomenko, A.; Haq, M.; Drzal, L.T.; Loos, A. Interlaminar reinforcement of glass fiber/epoxy composites with graphene nanoplatelets. *Composites Part A: Applied Science and Manufacturing* **2015**, *70*, 82-92.
81. Wang, F.; Drzal, L.T.; Qin, Y.; Huang, Z. Size effect of graphene nanoplatelets on the morphology and mechanical behavior of glass fiber/epoxy composites. *Journal of Materials Science* **2016**, *51*, 3337-3348.
82. Tang, Y.; Ye, L.; Zhang, D.; Deng, S. Characterization of transverse tensile, interlaminar shear and interlaminate fracture in cf/ep laminates with 10wt% and 20wt% silica nanoparticles in matrix resins. *Composites Part A: Applied Science and Manufacturing* **2011**, *42*, 1943-1950.
83. Zeng, Y.; Liu, H.-Y.; Mai, Y.-W.; Du, X.-S. Improving interlaminar fracture toughness of carbon fibre/epoxy laminates by incorporation of nano-particles. *Composites Part B: Engineering* **2012**, *43*, 90-94.

84. Kinloch, A.; Mohammed, R.; Taylor, A.; Sprenger, S.; Egan, D. The interlaminar toughness of carbon-fibre reinforced plastic composites using 'hybrid-toughened'matrices. *Journal of materials Science* **2006**, *41*, 5043-5046.
85. Tang, Y.; Ye, L.; Zhang, Z.; Friedrich, K. Interlaminar fracture toughness and cai strength of fibre-reinforced composites with nanoparticles–a review. *Composites Science and Technology* **2013**, *86*, 26-37.
86. Tehrani, M.; Boroujeni, A.; Hartman, T.; Haugh, T.; Case, S.; Al-Haik, M. Mechanical characterization and impact damage assessment of a woven carbon fiber reinforced carbon nanotube–epoxy composite. *Composites Science and Technology* **2013**, *75*, 42-48.
87. Garcia, E.J.; Wardle, B.L.; Guzman deVilloria, R.; Wicks, S.; Ishiguro, K.; Yamamoto, N.; Hart, A.J. In *Aligned carbon nanotube reinforcement of advanced composite ply interfaces*, Proceedings of the 49th AIAA/ASME/ASCE/AHS/ASC structures, structural dynamics, and materials conference. Schaumburg, IL, 2008; pp 7-10.
88. Boroujeni, A.Y.; Tehrani, M.; Manteghi, M.; Zhou, Z.; Al-Haik, M. Electromagnetic shielding effectiveness of a hybrid carbon nanotube/glass fiber reinforced polymer composite. *Journal of Engineering Materials and Technology* **2016**.
89. BOROUJENI, A.Y.; PHILEN, M.; AL-HAIK, M. In *Smart hybrid zno nanowire/carbon fiber reinforced polymer composites with in-situ structural health monitoring capability*, American Society of Composites-30th Technical Conference, 2015.
90. Groo, L.; Chung, H.; Boroujeni, A.Y.; Emami, A.; Al-Haik, M.; Philen, M. In *Characterization of zno piezoelectric nanowires in energy harvesting for fiber-reinforced composites*, ASME 2015 Conference on Smart Materials, Adaptive Structures and Intelligent Systems, 2015; American Society of Mechanical Engineers: pp V002T007A014-V002T007A014.
91. Wagner, R.; Ellis, W. Vapor-liquid-solid mechanism of single crystal growth. *Applied Physics Letters* **1964**, 89-90.
92. BOROUJENI, A.Y.; SKANDANI, A.A.; EMAMI, A.; AL-HAIK, M. In *Impact performance of a hybrid zno nanorod/carbon nanotube/carbon fiber reinforced polymer composite*, American Society of Composites-30th Technical Conference, 2015.
93. Malakooti, M.H.; Hwang, H.-S.; Sodano, H.A. Morphology-controlled zno nanowire arrays for tailored hybrid composites with high damping. *ACS applied materials & interfaces* **2014**, *7*, 332-339.
94. ASTM. Standard test method for tensile properties of polymer matrix composite materials. In *ASTM D3039/D 3039M*, 1995.
95. Sumita, M.; Gohda, H.; Asai, S.; Miyasaka, K.; Furuta, A.; Suzuki, Y.; Uchino, K. New damping materials composed of piezoelectric and electro-conductive, particle-filled polymer composites: Effect of the electromechanical coupling factor. *Die makromolekulare chemie, rapid communications* **1991**, *12*, 657-661.
96. Wicks, S.S.; Wang, W.; Williams, M.R.; Wardle, B.L. Multi-scale interlaminar fracture mechanisms in woven composite laminates reinforced with aligned carbon nanotubes. *Composites Science and Technology* **2014**, *100*, 128-135.
97. ASTM, A. D5528-13, standar test method for mode i interlaminar fracture toughness of unidirectional fiber reinforced polymer matrix composites. *West Conshohocken, PA: ASTM international* **2013**.
98. Wang, Y.; Zhao, D. Characterization of interlaminar fracture behaviour of woven fabric reinforced polymeric composites. *Composites* **1995**, *26*, 115-124.

99. Kepple, K.; Sanborn, G.; Lacasse, P.; Gruenberg, K.; Ready, W. Improved fracture toughness of carbon fiber composite functionalized with multi walled carbon nanotubes. *Carbon* **2008**, *46*, 2026-2033.
100. Thakre, P.R.; Lagoudas, D.C.; Riddick, J.C.; Gates, T.S.; Frankland, S.-J.V.; Ratcliffe, J.G.; Zhu, J.J.; Barrera, E.V. Investigation of the effect of single wall carbon nanotubes on interlaminar fracture toughness of woven carbon fiber-epoxy composites. *Journal of Composite Materials* **2011**, 0021998310389088.
101. Krueger, R. Virtual crack closure technique: History, approach, and applications. *Applied Mechanics Reviews* **2004**, *57*, 109-143.
102. Irwin, G. Handbuch der physik. *Vol. VI (Springer, Berlin, 1958) p* **1958**, *49*, I4.
103. Broek, D. *Elementary engineering fracture mechanics*. Springer Science & Business Media: 2012.
104. Sadeghian, R.; Gangireddy, S.; Minaie, B.; Hsiao, K.-T. Manufacturing carbon nanofibers toughened polyester/glass fiber composites using vacuum assisted resin transfer molding for enhancing the mode-i delamination resistance. *Composites Part A: applied science and manufacturing* **2006**, *37*, 1787-1795.
105. Tsantzalis, S.; Karapappas, P.; Vavouliotis, A.; Tsotra, P.; Kostopoulos, V.; Tanimoto, T.; Friedrich, K. On the improvement of toughness of cfrps with resin doped with cnf and pzt particles. *Composites Part A: Applied Science and Manufacturing* **2007**, *38*, 1159-1162.
106. Li, Y.; Hori, N.; Arai, M.; Hu, N.; Liu, Y.; Fukunaga, H. Improvement of interlaminar mechanical properties of cfrp laminates using vgcf. *Composites Part A: applied science and manufacturing* **2009**, *40*, 2004-2012.
107. Tehrani, M. Next generation multifunctional composites for impact, vibration and electromagnetic radiation hazard mitigation. **2012**.
108. Hartman, T.; Allen, D.; Case, S. In *Failure of spectra shield uhmwpe composite due to low velocity hard body impact*, SAMPE fall technical conference, Salt Lake City, UT, 2010.
109. Sun, C.; Potti, S. A simple model to predict residual velocities of thick composite laminates subjected to high velocity impact. *International Journal of Impact Engineering* **1996**, *18*, 339-353.
110. Standard, A. D3479/d3479m 1996 (2007)," standard test method for tension-tension fatigue of polymer matrix composite materials", astm international, west conshohocken, pa, 2007, doi: 10.1520/d3479_d3479m-96r07.
111. Standard, A. Standard practice for statistical analysis of linear or linearized stress-life (sn) and strain-life (en) fatigue data. *West Conshohocken. PA* **1998**.